Targeting heat shock protein 70 to increase chemosensitivity in ovarian cancer

Dissertation

zur Erlangung des akademischen Grades eines
Doktors der Medizin (Dr. med.)

an der

Medizinischen Fakultät der Universität Hamburg

vorgelegt von

Zhuoqun Ma

aus

Xuzhou, Volksrepublik China

2025

Betreuer:in / Gutachter:in der Dissertation: Prof. Dr. Leticia Oliveira-Ferrer

Gutachter:in der Dissertation: Prof. Dr. Sabine Windhorst

Vorsitz der Prüfungskommission: Prof. Dr. Sabine Windhorst

Mitglied der Prüfungskommission: PD Dr. Simon Joosse

Mitglied der Prüfungskommission: PD Dr. Katharina Harms-Effenberger

Datum der mündlichen Prüfung: 17.06.2026

CONTENTS

1. Hypothesis and Objectives

Epithelial ovarian cancer (EOC) is often diagnosed at an advanced stage with peritoneal dissemination and malignant ascites. Platinum-based chemotherapy is standard systemic treatment, but many patients relapse with cisplatin-resistant disease. Our previous work has demonstrated that tumor cell aggregates in ascites, so-called spheroids, exhibit high tumorigenicity and are likely the main contributors to the development of peritoneal metastasis. These spheroids express high mRNA levels of the stress-inducible HSP70 isoforms HSPA1A, HSPA1B and HSPA6 compared with matched solid tumor tissues, suggesting that they may play a role in stress adaptation and chemotherapy tolerance. However, the functional contribution of these stress-inducible HSP70 isoforms to the platinum response in EOC has not been fully defined. The working hypothesis of this thesis is that stress-inducible HSP70 isoforms contribute to the survival of ascites-derived spheroids under platinum-based chemotherapy.

Accordingly, the objectives of this project are:

1) To characterise the expression of HSPA1A, HSPA1B and HSPA6 at mRNA and protein levels in EOC cell lines, tumor tissues and patient-derived spheroids.

2) To determine whether HSP70 inhibition influences cell viability and cisplatin sensitivity *in vitro* and *in vivo*.

3) To analyse the effect of HSPA6 silencing on cisplatin response *in vitro* and *in vivo*.

Together, these objectives aim to provide preclinical evidence whether HSP70 is a viable target to enhance platinum efficacy in advanced EOC.

2. Introduction

2.1. Epithelial Ovarian Cancer

2.1.1. Epidemiology and Global Disease Burden

Epithelial ovarian cancer (EOC) is one of the most common malignant tumors of the female reproductive system and a leading cause of cancer-related mortality among women worldwide (Lavoué et al., 2013, Krzystyniak et al., 2016). In 2020, EOC ranked eighth in incidence and seventh in mortality among female malignancies. Approximately 310,000 new cases and 210,000 deaths were recorded globally in 2020, both higher than in 2019 (Caruso et al., 2025). Forecasts suggest that by 2040, the global incidence of ovarian cancer will increase by about 42%, and mortality will rise by more than 50% (Webb and Jordan, 2024). Together, these trends indicate that improvements in overall survival remain limited despite advances in screening and treatment.

Marked geographic heterogeneity exists in the global distribution of EOC. Incidence is highest in Northern and Central/Eastern Europe, intermediate in North America, Western Europe, and Australia, and lowest in Asia and Africa (Zhuang et al., 2025). These differences are likely attributable to socioeconomic status, lifestyle, obesity prevalence, delayed childbearing, and the use of oral contraceptives. Although incidence has declined modestly in some high-incidence regions, many historically low-incidence regions are now experiencing increases associated with urbanization and lifestyle westernization, narrowing previous regional differences.

2.1.2. Pathogenesis and Risk Factors

Ovarian carcinogenesis is a multifactorial, multistep process driven by genetic susceptibility, hormonal exposure, chronic inflammation, and environmental influences. Epidemiologic studies have linked advanced age, obesity, nulliparity or first pregnancy after the age of 35, long-term hormone

replacement therapy, and a positive family history of cancer to an increased risk of EOC. Prolonged exposure to specific environmental agents such as talc and asbestos has also been proposed as a potential risk factor (Langseth et al., 2008).

At the molecular level, germline mutations in BRCA1 and BRCA2 represent the most important hereditary risk factors for EOC (Gráf et al., 2021). These mutations impair DNA repair, increase cellular vulnerability to DNA damage, promote genomic instability, and facilitate tumorigenesis (Kim et al., 2023, Zhao et al., 2022). Women carrying BRCA1 mutations have an estimated lifetime ovarian cancer risk of roughly 40%, whereas those with BRCA2 mutations have a risk of about 18% (Suthers, 2007). Mismatch repair defects associated with Lynch syndrome and TP53-related Li–Fraumeni syndrome also confer substantially elevated risk. Beyond BRCA, pathogenic variants in homologous recombination repair genes, including RAD51C, RAD51D, PALB2, and CHEK2, are implicated in disease susceptibility and may influence sensitivity to platinum-based chemotherapy (Pietragalla et al., 2020, Toss et al., 2015).

According to the 2020 World Health Organization classification, ovarian tumors are categorized into epithelial, sex cord–stromal, germ cell, and mixed types, with epithelial ovarian cancer accounting for approximately 90% of cases (Mezzapesa et al., 2025). EOC comprises five major histological subtypes: high-grade serous ovarian cancer (HGSOC), low-grade serous ovarian cancer (LGSOC), endometrioid ovarian cancer (EnOC), ovarian clear cell carcinoma (OCCC), and mucinous ovarian carcinoma (Zhu et al., 2022, Romero et al., 2020). HGSOC constitutes about 70% of EOC cases and is responsible for 70–80% of deaths. The median overall survival is approximately 40 months, and the 5-year survival rate is below 50% (Bowtell et al., 2015). Current evidence suggests that most HGSOC originates from the fimbrial epithelium of

the fallopian tube rather than the ovarian surface epithelium, with important implications for strategies aimed at early detection and prevention. In addition to histopathological classification, epithelial ovarian carcinomas can also be grouped according to a dualistic model that distinguishes type I and type II tumors. Type I tumors encompass most low-grade, genetically more stable entities, including low-grade serous, endometrioid, clear cell, mucinous and Brenner tumors, whereas type II tumors are high-grade, genomically unstable carcinomas, predominantly HGSOC (Shih Ie and Kurman, 2004). Based on gene expression profiling of HGSOC, four reproducible molecular subtypes—immunoreactive, proliferative, mesenchymal and differentiated—have been proposed, which differ in immune and stromal signatures and are associated with distinct clinical outcomes and potential therapeutic vulnerabilities (Konecny et al., 2014) .

2.1.3. Diagnosis and Early Detection

EOC often presents insidiously and lacks specific early symptoms, which contributes to its high mortality. More than 70% of patients are diagnosed at FIGO stage III or IV, frequently with ascites and extensive peritoneal dissemination (Saji et al., 2007, Marchetti et al., 2010). Early-stage disease may manifest only as mild abdominal pain, distension, or dyspepsia and is easily mistaken for gastrointestinal disorders. Commonly used serum biomarkers—cancer antigen 125 (CA125), human epididymis protein 4 (HE4), and multianalyte panels such as OVA1—have limited sensitivity and specificity, particularly for early disease (Gaillard et al., 2025). Imaging modalities including ultrasonography, computed tomography (CT), and magnetic resonance imaging (MRI) assist in disease assessment but are insufficient for effective population-level screening (Liu et al., 2017).

With advances in molecular diagnostics, approaches based on liquid biopsy, including circulating tumor DNA (ctDNA), exosomal RNA, and methylation

profiling, are being investigated as early detection tools. Integrative multi-omics strategies that combine genomics, proteomics, and metabolomics may further improve the identification of high-risk populations and the early diagnosis of EOC (Soda et al., 2019). However, to date, no screening strategy has yet been shown to reduce mortality at the population level, and definitive diagnosis still relies primarily on imaging findings followed by postoperative histopathology.

2.1.4. Treatment Paradigms and Prognosis

Standard management of EOC consists of cytoreductive surgery combined with platinum-based chemotherapy, typically cisplatin or carboplatin in combination with a taxane (Lheureux et al., 2019). Although most patients initially respond to chemotherapy, EOC is characterized by high rates of relapse, rapid progression, and poor long-term outcomes. Recurrent disease is frequently chemoresistant, with response rates of only 10–20% and a 5-year survival rate after recurrence below 15% (Xi et al., 2023). Prognosis is influenced by clinical stage, histologic subtype, residual disease after surgery, molecular subtype, driver mutations, and features of the tumor microenvironment. Mechanisms underlying resistance include increased drug efflux, enhanced DNA repair capacity, epigenetic alterations, and remodeling of the tumor microenvironment.

Since the beginning of the 21st century, the therapeutic landscape of ovarian cancer has gradually shifted toward molecularly targeted therapy and immunotherapy. Inhibitors of poly (ADP-ribose) polymerase (PARP) (Ray-Coquard et al., 2023), such as olaparib, niraparib, and veliparib, have been shown to significantly prolong progression-free survival in patients with BRCA-mutated tumors or homologous recombination deficiency (HRD)-positive disease (Leary et al., 2016). In parallel, inhibition of the vascular endothelial growth factor (VEGF) signaling pathway, exemplified by

bevacizumab, suppresses tumor angiogenesis and can improve clinical outcomes in selected patients, including those with chemoresistant disease (Khosravi-Shahi and Cabezon-Gutierrez, 2012). Multiple targeted agents directed against epidermal growth factor receptor (EGFR), mammalian target of rapamycin (mTOR), and the phosphoinositide 3-kinase/protein kinase B (PI3K/AKT) pathway are under active investigation, although their overall efficacy remains limited at present (Carnero et al., 2008, Osaki et al., 2004).

In recent years, immune checkpoint inhibitors targeting programmed cell death protein 1 (PD-1) and programmed death-ligand 1 (PD-L1) have demonstrated potential activity in subsets of patients with recurrent ovarian cancer, providing a therapeutic option for otherwise refractory disease (Li et al., 2018, Zsiros et al., 2021). Consequently, treatment strategies are evolving from conventional cytotoxic chemotherapy alone toward multimodal regimens that integrate targeted therapy, anti-angiogenic therapy, and immunotherapy (González-Martín et al., 2014, Kim et al., 2017). Future work will need to address how mechanisms of drug resistance intersect with metastatic progression and to define the key signaling networks that sustain these phenotypes. A better understanding of these pathways may help identify novel diagnostic biomarkers and therapeutic targets and could ultimately improve the long-term prognosis of patients with recurrent ovarian cancer.

2.1.5. Patterns and Mechanisms of Metastasis and Recurrence

Metastasis is the leading cause of death in patients with advanced EOC. EOC disseminates primarily through three main routes: intraperitoneal seeding, lymphatic spread, and hematogenous metastasis (Yousefi et al., 2020). Intraperitoneal implantation is most common. Exfoliated tumor cells circulate in peritoneal fluid and colonize the pelvis, subdiaphragmatic surfaces, hepatic capsule, mesentery, and omentum. In advanced HGSOC, more than 80% of patients have peritoneal dissemination at diagnosis. Distant metastases

frequently involve the lungs (15–28%), liver (26–37%), and lymph nodes (30–60%), whereas bone (~4%) and the central nervous system (1–12%) are less commonly affected (Konishi et al., 2022, Bayraktar et al., 2024). Involvement of the liver, lungs, or brain is associated with a particularly poor prognosis (Bayraktar et al., 2024).

Metastasis in EOC is a complex, multistep process encompassing alterations in cell adhesion and detachment, extracellular matrix (ECM) degradation, angiogenesis, epithelial–mesenchymal transition (EMT), immune evasion, and dynamic remodeling of the tumor microenvironment (TME) (Klymenko et al., 2017, Dhaliwal and Shepherd, 2022). During dissemination, EOC cells rely on cytoskeletal reorganization and ECM degradation, coupled with metabolic reprogramming and aberrant activation of signaling pathways such as PI3K/AKT, transforming growth factor-β (TGF-β), Wnt/β-catenin, and nuclear factor-κB (NF-κB) (Cai et al., 2018, Bou Antoun and Chioni, 2023). Cancer-associated fibroblasts (CAFs) and tumor-associated macrophages (TAMs) secrete cytokines, promote angiogenesis, and induce immunosuppression, thereby enhancing invasion and distant spread (Monteran and Erez, 2019, Liu et al., 2024).

Recurrence and metastasis are tightly linked. Under the selective pressure of chemotherapy, tumor cells progressively acquire resistance through adaptive mutations and changes in signaling pathways that enhance migratory capacity and survival (Nachtigal et al., 2022). Key features include upregulation of DNA repair, activation of anti-apoptotic programs, and shifts in cellular metabolism, which together help tumor cells to evade cytotoxic injury. These changes are accompanied by remodeling of the TME and the emergence of resistant clonal populations, further driving relapse and systemic dissemination. Recurrence and metastasis in ovarian cancer involve interactions between genetic mutations, epigenetic regulation, and intercellular signaling networks. Therapy

resistance in metastatic and recurrent disease is a major cause of treatment failure and a central challenge in postoperative management (Alemzadeh et al., 2024, Song et al., 2022b)

2.1.6. Tumor Microenvironment in Epithelial Ovarian Cancer

The tumor microenvironment (TME) of epithelial ovarian cancer (EOC), similar to that of other solid tumors, comprises immune cells, fibroblasts, vascular endothelial cells, extracellular matrix (ECM) components, and a variety of soluble factors. In general, the TME is a critical determinant of tumor initiation, progression, and therapeutic response (Maman and Witz, 2018, Anderson and Simon, 2020). In EOC, escape from immune surveillance is a key feature of disease pathobiology and treatment resistance. As described for many malignancies, ovarian tumour cells can downregulate major histocompatibility complex class I (MHC-I) molecules, thereby reducing antigen presentation and evading cytotoxic T-cell recognition (Whiteside, 2008). Like tumor cells in other cancers, they also secrete immunosuppressive cytokines such as TGF-β and interleukin-10 (IL-10) and recruit regulatory T cells (Tregs) and myeloid-derived suppressor cells (MDSCs) to establish a sustained immunosuppressive niche (Raimondi et al., 2007). MDSCs can further promote Treg induction through secretion of IL-10 and TGF-β and expression of arginase-1 (ARG1), indoleamine 2,3-dioxygenase (IDO), and CD40, mechanisms that have been described in cancer and other chronic inflammatory settings (Pawelec et al., 2021). Pro-inflammatory mediators including tumor necrosis factor-α (TNF-α) and interleukin-6 (IL-6) facilitate angiogenesis and ECM remodeling, providing nutrients and space for tumor growth while contributing to therapy resistance. Chronic inflammation reinforces the accumulation of Tregs and MDSCs and amplifies local immunosuppression (Manickasamy et al., 2025).

Cancer-associated fibroblasts (CAFs) and ECM remodeling are also important components of the ovarian cancer TME. In line with observations in other solid tumors, CAFs in EOC secrete TGF-β, VEGF, and matrix metalloproteinases (MMPs), directly promoting tumor cell proliferation, migration, and invasion (Wu et al., 2021). By altering ECM composition and structure, they create permissive physical tracks for dissemination and foster neovascularization that sustains tumor growth and spread. To adapt to hypoxia and nutrient deprivation within the TME, EOC cells undergo metabolic reprogramming characterized by enhanced glycolysis (the Warburg effect), even under aerobic conditions(Vaupel and Multhoff, 2021). This metabolic shift supports survival and proliferation in hostile environments and is associated with increased invasiveness and therapeutic resistance, both in EOC and in other solid malignancies. Improved mechanistic insight into the ovarian cancer TME may help to optimize immunotherapy and to develop microenvironment-targeted treatment strategies.

2.2. Platinum-Based Chemotherapy in Ovarian Cancer

2.2.1. Historical Development and Drug Classes

Chemotherapy remains a cornerstone of systemic therapy for ovarian cancer (Armstrong, 2013, Ozols, 2006). Before the 1970s, advanced-stage disease was typically treated with single-agent alkylators such as melphalan, cyclophosphamide, thiotepa, or chlorambucil, achieving clinical complete responses in only about 20% of patients, with median survival of 10–14 months and substantial hematologic toxicity (Thigpen et al., 1994, du Bois et al., 2009, Greene et al., 1982). The serendipitous observation in 1965 that platinum compounds inhibit Escherichia coli division led to the identification of cisplatin and, by the early 1980s, to its recognition as a potent antineoplastic agent that acts primarily through DNA interactions (Taniguchi et al., 2003). Clinical trials demonstrated superior outcomes with platinum agents, either alone or in combination, compared with non-platinum regimens, spurring widespread clinical adoption (Aabo et al., 1998). Since then, thousands of platinum analogs have been synthesized. These compounds are broadly categorized as Pt(II) or Pt(IV) agents based on oxidation state, and several have gained regulatory approval(Galanski and Keppler, 2007, Yan et al., 2016).

2.2.2. Mechanisms of Action of Cisplatin

Clinically used platinum agents include cisplatin, carboplatin, oxaliplatin, nedaplatin, and lobaplatin, with cisplatin and carboplatin being most widely used in ovarian cancer (Monneret, 2011, Dasari and Tchounwou, 2014). Cisplatin exerts antitumor activity primarily by forming DNA adducts and inducing intra- and interstrand crosslinks at the N7 position of guanine (Minerva et al., 2023). These lesions distort the DNA double helix, impede replication and transcription, and, when irreparable, trigger cell-cycle arrest and apoptosis (Woźniak and Błasiak, 2002, Ma et al., 2021). Within cells,

cisplatin perturbs antioxidant defenses, increases reactive oxygen species (ROS), and activates pro-inflammatory and pro-apoptotic signaling pathways (Lin et al., 2023). Mitochondrial release of cytochrome c further amplifies the apoptotic cascade (Zhu et al., 2015). Additional effects include interference with RNA transcription, cytoplasmic acidification, reduced metabolic plasticity, and activation of estrogen receptor-related stress responses (Dejonghe et al., 2016). Together, these effects contribute to the antitumor activity of cisplatin and have guided the development of next-generation platinum compounds.

2.2.3. Clinical Use of Cisplatin and Mechanisms of Resistance

Cisplatin entered clinical trials in 1972 and received regulatory approval in 1978 for testicular, bladder, and ovarian cancers, becoming one of the earliest widely used cytotoxic agents (Boulikas and Vougiouka, 2004, Zoń and Bednarek, 2023). As a first-line therapy for ovarian cancer, cisplatin achieves high initial response rates, reducing tumor burden and delaying progression (Ghosh, 2019). Nevertheless, more than half of patients with advanced disease relapse within two years, and many ultimately succumb to chemoresistant disease; the 5-year overall survival remains below 30% (Torre et al., 2018). Cisplatin resistance is a major cause of treatment failure and a biological driver of recurrence and metastasis. Resistance involves multiple layers: decreased drug uptake or increased efflux; upregulation of detoxification systems (e.g., glutathione); enhancement of DNA damage recognition and repair, particularly homologous recombination and nucleotide excision repair; attenuation of apoptotic signaling; alterations of the cytoskeleton and cellular membranes affecting drug distribution; and microenvironment-mediated protective effects (Li et al., 2024, Li et al., 2022, Zhu et al., 2023). Targeting these mechanisms may help to restore chemosensitivity, delay relapse, and prolong survival.

Multiple lines of evidence also suggest that stress-response pathways, including heat shock proteins, modulate these resistance mechanisms by stabilizing damaged proteins and coordinating DNA damage responses (Li et al., 2021, Sottile and Nadin, 2018, Gaponova et al., 2017).

2.3. Heat Shock Proteins and HSP70

2.3.1. Discovery and Classification of Heat Shock Proteins

Heat shock proteins (HSPs) were first described in 1962 in Drosophila salivary glands as chromosomal ‘puffs’ that appeared after a temperature shift from 25 °C to 32 °C for 30 minutes, indicating enhanced transcription and protein synthesis (Jee et al., 2021). Subsequent studies in 1974 confirmed that heat stress augments transcription in specific chromosomal regions, producing proteins of approximately 70 kDa and 26 kDa that were collectively termed HSPs (Pauli et al., 1986). The molecular chaperone concept, proposed in 1992, established HSPs as central components of cellular proteostasis (Blander and Horwitz, 1993). HSPs are ubiquitous across bacteria, plants, and animals. Under basal conditions, they support protein folding, trafficking, and maintenance of native conformations; under exogenous (heat, cold, hypoxia, heavy metals) or endogenous (DNA damage, tissue injury, infection) stress, HSP expression increases to counteract protein denaturation and aggregation. Numerous studies have since reported overexpression of HSPs in cancer and linked this to apoptosis resistance and modulation of antitumor immunity, with HSP70 being the most extensively investigated member of the family (Liu et al., 2012, van Noort et al., 2012).

By molecular mass, HSPs are grouped into five major families: HSP110 (100–110 kDa), HSP90 (90 kDa), HSP70 (70 kDa), HSP60 (60 kDa), and the small HSPs (12–43 kDa) (Kaigorodova and Bogatyuk, 2014). HSP70 proteins are among the most conserved and abundant, comprising an ~44 kDa N-terminal ATPase domain, an ~18 kDa substrate-binding domain, and an ~10 kDa C-terminal domain (Liu et al., 2012).

2.3.2. Cellular Functions of HSP70

HSP70 performs three core proteostasis functions: (1) folding of nascent and denatured polypeptides into their native conformations; (2) refolding of aggregated proteins; and (3) targeting of insoluble aggregates for degradation via the ubiquitin–proteasome system or chaperone-mediated lysosomal autophagy (Kampinga and Craig, 2010). HSP70 also facilitates macromolecular trafficking (proteins and RNA), secretion, activation of signaling pathways, regulation of transcription factors, and cellular processes including division, migration, and differentiation (Zhang and Qi, 2025, Kampinga and Craig, 2010). Its expression is low in non-stressed cells but is markedly upregulated under heat shock, oxidative stress, hypoxia, pH perturbation, and heavy-metal exposure—conditions that are also implicated in oncogenesis and tumor progression (Du et al., 2009).

2.3.3. Oncologic Roles of HSP70

Cancer cells inhabit hostile microenvironments characterized by elevated oxidative stress, nutrient deprivation, hypoxia, accumulation of mutant proteins, and the selective pressure of cytotoxic therapies (Martínez-Reyes and Chandel, 2021, Hinshaw and Shevde, 2019). To survive, they rely heavily on chaperone networks—particularly HSP70—and adapt organelle crosstalk as well as metabolic and signaling pathways (Zhao et al., 2023). HSP70 is frequently overexpressed across malignancies, and has been implicated in tumorigenesis and mediates chemoresistance. For example, pharmacologic inhibition of HSP70 with pifithrin-μ reduces cisplatin resistance in prostate cancer models. HSP70 overexpression confers resistance to imatinib in chronic myeloid leukemia K562 cells; it is associated with resistance to topotecan and gemcitabine in fibrosarcoma; and HSP70-containing exosomes can propagate resistance to oxaliplatin and 5-fluorouracil in colorectal cancer (Balaburski et al., 2013, Noessner et al., 2002, Pocaly et al., 2007). Consistent

with these findings, targeting HSP70 is being explored as a strategy to overcome therapy resistance.

HSP70 also modulates antitumor immunity. It can chaperone tumor-specific peptides for uptake by dendritic cells and presentation via major histocompatibility complex (MHC) class I and II pathways to T and B lymphocytes, eliciting antigen-specific immune responses (Noessner et al., 2002, Ueda et al., 2004, Gong et al., 2009). Natural killer (NK) cells may be recruited through HSP70-related cues and release granzyme B, which, upon interacting with HSP70, induces tumor cell apoptosis (Gastpar et al., 2005, Gross et al., 2003). Conversely, HSP70 may protect malignant cells from tumor necrosis factor (TNF)-induced cytotoxicity, thereby promoting immune evasion and tumor progression (Jäättelä et al., 1992). Overall, HSP70 links proteostasis, chemotherapy resistance, and antitumor immunity. Taken together, these roles support the development and clinical evaluation of HSP70 inhibitors as adjuncts to established treatment regimens.

2.4. Previous findings of this Thesis

2.4.1. mRNA Levels of Stress-Induced HSP70 Isoforms in Ovarian Cancer

Previous work from the gynecology laboratory on ascites-derived spheroids revealed a significantly higher mRNA levels of the stress-induced HSP70 members HSPA1A, HSPA1B, and HSPA6 compared with matched primary and metastatic solid tumor samples (n = 30) (Ding et al., 2021). On this basis, an expanded bulk RNA-seq cohort from our centre, comprising 244 tissue samples from 211 patients, was analysed. Across the cohort, HSPA1A/1B/6 mRNA levels were lower than those of constitutive family members such as HSPA5, HSPA8, and HSPA9 (Figure 1A), yet the three stress-induced genes showed strong pairwise correlations with each other and with HSPA7 (Figure 1B).

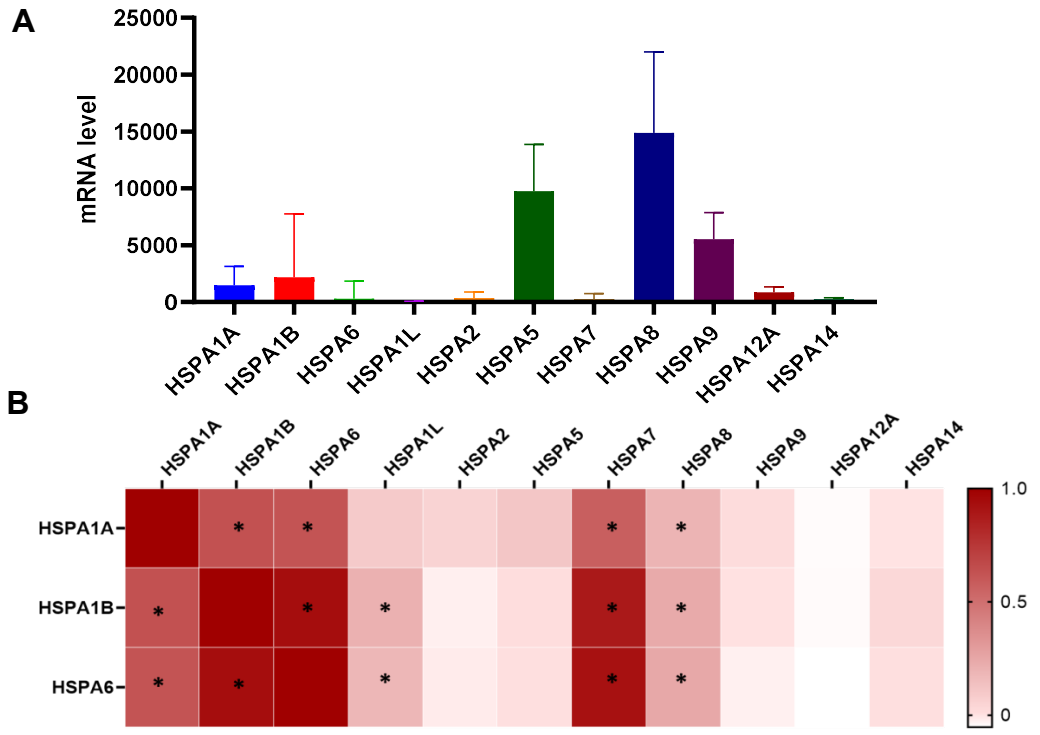

Figure 1 *HSP70 isoform mRNA expression and co-expression in 244 ovarian cancer samples.*

A. Mean mRNA levels of all HSP70 isoforms (RNA-seq, n = 244);

B. Correlation matrix of HSP70 isoforms (Pearson r, n = 244).

* p < 0.05; ** p < 0.01; *** p < 0.001; **** p < 0.0001.

In this cohort, no association was detected between HSPA1A/1B/6 expression and overall survival (Figure 2). A weak but statistically significant association was observed between higher HSPA1A expression and longer disease-free survival (DFS; p = 0.014), whereas HSPA1B and HSPA6 showed no impact on DFS (Figure 2).

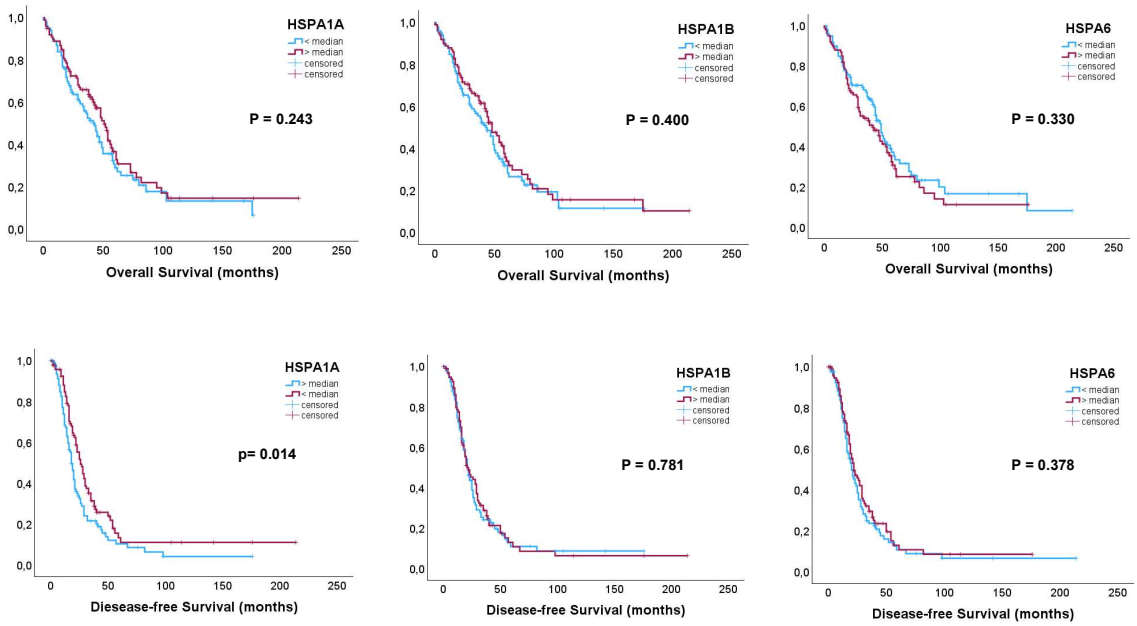

Figure 2 *Kaplan-Meier curves and log-rank test showing the association between HSPA1A/1B and HSPA6 mRNA levels and overall survival (upper panel) and disease-free survival (lower panel)*

2.4.2. Protein-Level Validation in Ascites-Derived Spheroids

Given the RNA-level findings and the lack of strong clinicopathological associations, protein-level validation was performed in matched sets of ascites-derived spheroids and the corresponding solid tumor tissues. Western blot analysis (Figure 3) demonstrated higher HSPA1A/B and HSPA6 protein expression in ascites-derived spheroids (S) than in solid tumor tissues (T), with a particularly pronounced difference for HSPA6.

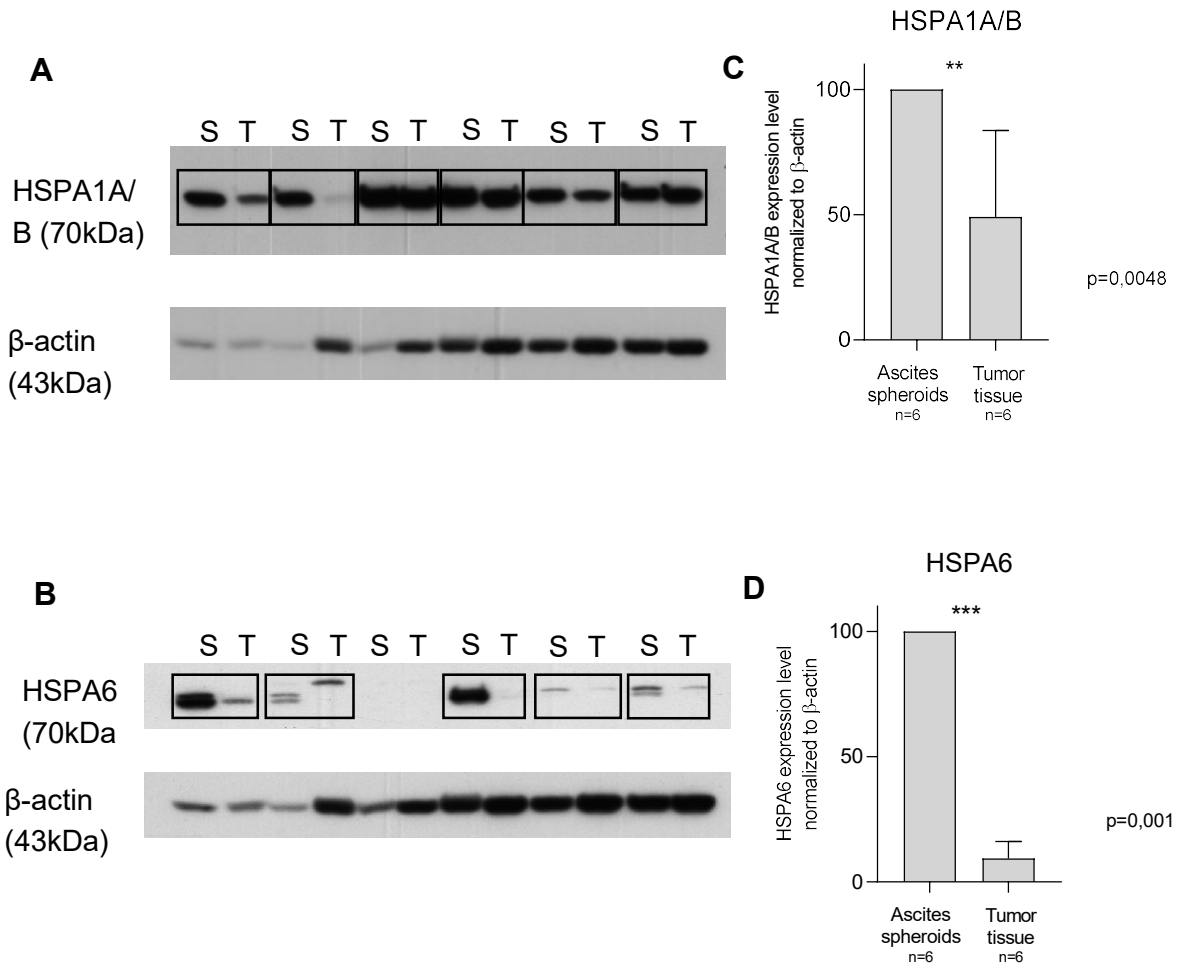

Figure 3 *Enrichment of HSPA1A/B and HSPA6 in ascites-derived spheroids compared with corresponding tumor tissues*

A,B. Representative western blots of HSPA1A/B and HSPA6 in paired ascites-derived spheroids (S) and solid tumor tissues (T); β-actin (43 kDa) serves as loading control;

C,D. Densitometric quantification (normalised to β-actin) of HSPA1A/B and HSPA6 in ascites-derived spheroids versus tumor tissues.

* $p < 0.05$; ** $p < 0.01$; *** $p < 0.001$; **** $p < 0.0001$.

2.4.3. HSP70 Inhibition Reduces Viability in Ovarian Cancer Models and Sensitizes to Cisplatin

Motivated by the high HSP70 expression in patient spheroids and its reported chemoprotective roles, two Hsp70 inhibitors—Quercetin and VER-155008—were tested as single agents and in combination with cisplatin in OVCAR8 and SKOV3 cells under 2D monolayer and 3D spheroid conditions. Cisplatin alone or in combination with Quercetin reduced viability in both formats (Figure 4A & B, top). In 2D OVCAR8, Quercetin + cisplatin decreased viability significantly vs. cisplatin alone (Figure 4A, top). With VER-155008, a similar patternwas observed; in adherent OVCAR8, VER-155008 plus cisplatin further reduced viability relative to cisplatin monotherapy (Figure 4A, bottom). Patient-derived ascites spheroids were then examined: low-dose Quercetin (10 µM) already reduced viability compared with untreated controls and enhanced the effect of cisplatin, while higher-dose Quercetin (50 µM) produced an even greater reduction (Figure 4C, top). VER-155008 (20 µM), as a single agent and in combination with cisplatin, likewise lowered viability in patient spheroids (Figure 4C, bottom). Taken together, these data indicate that HSP70 activity supports survival in the ascites-derived spheroid niche and that pharmacological HSP70 inhibition can enhance cisplatin sensitivity, particularly in 3D models.

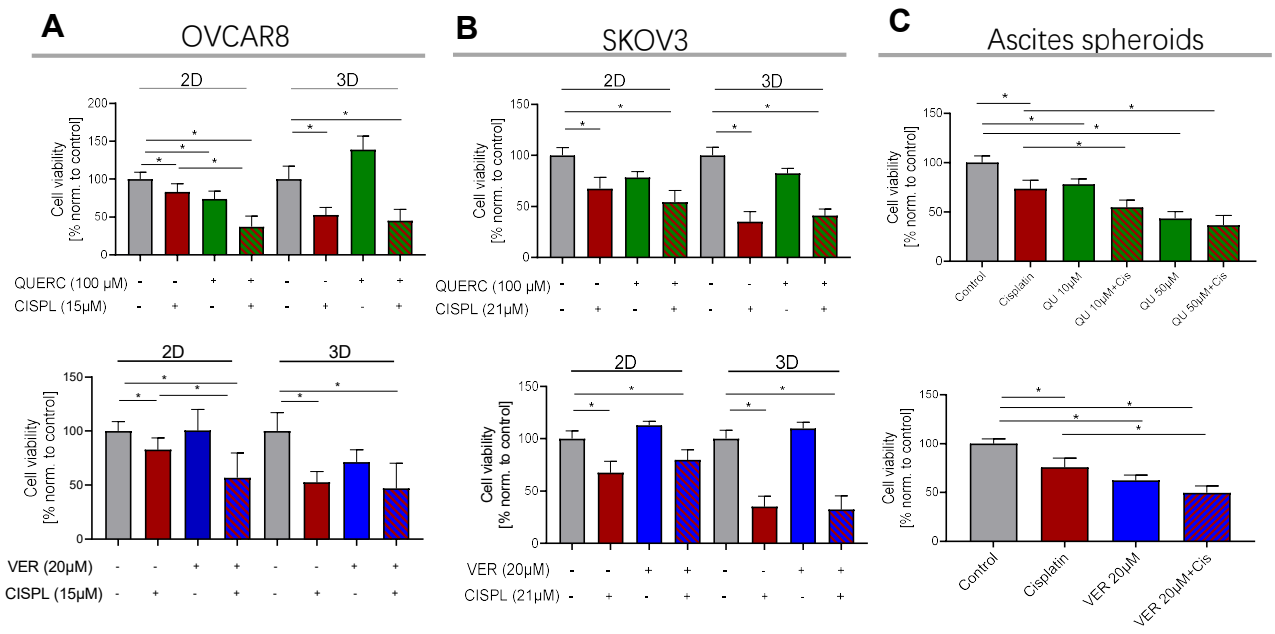

Figure 4 *HSP70 inhibition sensitises ovarian cancer cells and ascites-derived spheroids to cisplatin*

A. OVCAR8 cells treated with Quercetin (100 µM) or VER-155008 (20 µM), alone or in combination with cisplatin (15 µM), under 2D monolayer and 3D spheroid conditions.

B. SKOV3 cells exposed to quercetin (100 µM) or VER-155008 (20 µM), with or without cisplatin (21 µM), in 2D and 3D cultures.

C. Patient-derived spheroids treated with Quercetin (10 or 50 µM) or VER-155008 (20 µM), alone or with cisplatin. Cell viability is expressed as percentage of untreated control (mean ± SD).

* $p < 0.05$; ** $p < 0.01$; *** $p < 0.001$; **** $p < 0.0001$.

2.5 Scope of the present thesis within the overall project

Within the broader research programme on stress-inducible HSP70 isoforms in advanced epithelial ovarian cancer, the present MD thesis focuses on the role of HSPA1A, HSPA1B and HSPA6 in the platinum response of ascites-derived tumour cell spheroids. Building on the RNA-seq analyses and preclinical observations described above, this work is designed to characterise the expression of these isoforms at the mRNA and protein levels in tumour tissues, cell lines and patient-derived spheroids, and to evaluate whether pharmacological inhibition or genetic silencing of HSP70 can enhance cisplatin sensitivity *in vitro* and *in vivo*. In doing so, the thesis aims to provide translational evidence that stress-inducible HSP70 represents a promising target to improve the efficacy of platinum-based chemotherapy in advanced epithelial ovarian cancer.

3. Materials and Methods

3.1. Materials

3.1.1. Devices

Table 1 *Devices*

Device	Device designation	Manufacturer
Absorption reader	SunriseTM	Tecan Trading AG, Schweiz
Bioluminescence imaging system	IVIS 200	PerkinElmer
Blotting chamber	HoeferTMTE42 Tank Blotting Unit	Hoefer, Inc., Holliston, USA
Centrifuge 5810R	F-34-6-38 rotor and A-4-81 rotor	Eppendorf SE, Hamburg, Germany
Densitometer	GS-800 Calibrated Densitometer	Bio-Rad, Munich
Developer	CP1000 Automatic Film Processor	Agfa, Mortsel, Belgien
Electrophoresis	HoeferTM SE600 Series Vertical Electrophoresis System	Hoefer, Inc., Holliston, USA
Incubator	Heraeus/Kendro Lab HERAcell Incubator	Heraeus/Kendro Lab, Hanau
Luminescence microplate reader	CLARIOstar	BMG LABTECH, Ortenberg, Germany
Microcentrifuge	Biofuge FrescoTM	Heraeus, Hanau
Microplate reader	Infinite® M200	Tecan, Austria
Microscope	AxioVision 40	Carl Zeiss Imaging Solutions, Oberkochen, Germany
Precellys Evolution	Precellys Evolution	Bertin Technologies, France
Real-time PCR system	QuantStudio Real-Time PCR System	Applied Biosystems
Sliding microtome	Leica SM2000R	Leica Mikrosysteme Vertrieb GmbH, Wetzlar, Germany
Spectrophotometer	NanoDrop	Thermo Fisher Scientific, USA
PCR System	StepOne™ Real-Time PCR System	Applied Biosystems, Foster City, CA, USA
ThermoMixer® Compact	ThermoMixer® C 7096 5	Eppendorf SE, Hamburg, Germany

3.1.2. Materials

Table 2 *Materials*

Name	Manufacturer
Blottingpaper	Macherey- Nagel, Düren
Cell culture dishes, 100x20 mm	Greiner Bio-One, Frickenhausen, DE
Cell scraper	Sarstedt AG & Co., Nümbrecht, Germany
Cryo tubes	Greiner Bio-One International GmbH, Kremsmünster, Österreich.
Falcon® 15mL High Clarity PP Centrifuge Tube	Corning Incorporated, New York, US
Falcon® 50mL High Clarity PP Centrifuge Tube	Corning Incorporated, New York, US
Filter pipettes tips	Sarstedt AG & Co., Nümbrecht, Germany
MACS® Smartstrainer (30 µm + 100 µm)	Miltenyi Biotec B.V. & Co. KG, Sitz Bergisch Gladbach, Germany
Parafilm M	Bemis Company, Inc., Neenah, Wisconsin, USA
TC flask T75. Stand. Vent. Cap.	Thermo Fisher Scientific Inc., Waltham, USA
TC plate 48-, 24-, 6-well, standard	Thermo Fisher Scientific Inc., Waltham, USA
TC plate 96 well, standard	Sarstedt, Nuembrecht, DE

3.1.3. Medium, Kit, Reagent, Powders

Table 3 *Medium, Kit, Reagent, Powders*

Name	Manufacturer
10% normal goat serum	Vector Laboratories, USA; Cat# S-1000
10% normal horse serum	Vector Laboratories, USA; Cat# S-2000
40 % Acrylamid/bis-Acrylamid	Sigma-Aldrich, St. Louis, Missouri, USA
85 % Glycerin	Carl Roth, Karlsruhe
Accutase SCR005	Merck KGaA, Darmstadt, Germany
Ammoniumpersulfat (APS)	Bio-Rad, Hercules, Kalifornien, USA
Aquatex	Merck Cat# 1.08562.0050
CozyHi prestained Protein Ladder	highQu GmbH, Kraichtal
DAB Peroxidase Substrate Kit	Vector Laboratories Cat# SK-4100
DAKO Antibody Diluent	Agilent Technologies Cat# S0809
DAKO Target Retrieval Solution (pH 6.0)	Agilent Technologies Cat# S1699
Dimethyl sulfoxide (DMSO)	Sigma-Aldrich, St. Louis, USA; Cat# 472301
Dulbecco´s Phosphate Buffered Saline (PBS +/+); With $MgCl_2$ and $CaCl_2$, liquid, sterile-filtered, suitable for cell culture	Sigma-Aldrich, St. Louis, Missouri, USA
Dulbecco´s Phosphate Buffered Saline (PBS -/-); Modified, without calcium chloride and magnesium chloride, liquid, sterile-filtered, suitable for cell culture	Sigma-Aldrich, St. Louis, Missouri, USA
Ethanol	Carl Roth, Karlsruhe, DE
Eukitt mounting medium	Sigma-Aldrich Cat# 03989
Fetal Bovine Serum (FCS)	Biochrom AG, Merck Millipore, Darmstadt, Germany
Hematoxylin	Carl Roth, Karlsruhe
HighQu cDNA-Synthese Kit	HighQu; Cat# RTK0104
Immobilon®-P Transfer Membrane	Merck Millipore, Darmstadt
M199 medium	Sigma-Aldrich
McCoy's 5A medium	Gibco®, Thermo Fisher Scientific, Schwerte, Germany
MCDB 105 Medium	Sigma-Aldrich, St. Louis, Missouri, USA
Modified Eagle's Medium	Gibco®, Grand Island, NY, USA
Methanol	ThermoFisher Scientific, Waltham, MA USA

N,N,N',N'-Tetramethylethylendiamin (TEMED)	Sigma-Aldrich, St. Louis, Missouri, USA
Nuclease-free water, 50 mL	QIAGEN, Hilden, DE
Penicillin–streptomycin solution (2 mM)	Thermo Fisher Scientific, Waltham, MA, USA
Permanent AP-Red Kit	Zytomed Systems Cat# 001-125
Pierce ® BCA Protein Assay, Reagent A & B	ThermoFisher Scientific, Waltham, MA USA
Plasmid Midi Kit	Qiagen Cat# 163051488
Protease-Inhibitor (100x)	Sigma-Aldrich, St. Louis, Missouri, USA
qPCR Green ROX High Mix (2×)	HighQu; Cat# QPD0205
QIAquick PCR Purification Kit	Qiagen Cat#28104
Quercetin	Sigma-Aldrich, USA; Cat# Q4951-10G
RBC lysis buffer (10x), Invitrogen™	Thermo Fisher Scientific Inc., Waltham, USA
Rinder serum albumin (BSA)	Carl Roth, Karlsruhe
RPMI-1640 medium	Gibco®, Thermo Fisher Scientific, Schwerte, Germany
Sodiumdodecylsulfat (SDS)	Sigma-Aldrich, St. Louis, Missouri, USA
Trypan Blue Dye, 0.4% solution	Bio-Rad Laboratories, UK
Trypsin-EDTA	Thermo Fisher Scientific Inc.,, USA
Tween 20	Merck, Darmstadt
VECTASTAIN® ABC-AP Kit	Vector Laboratories Cat# AK-5000
VECTASTAIN® Elite® ABC Kit	Vector Laboratories Cat# PK-6100
VER-155008	Sigma-Aldrich, USA; Cat# SML0271-25MG
X-ray film developer solution	Calbe Chemie, Germany
X-ray film fixer solution	Calbe Chemie, Germany
β-Mercaptoethanol	Sigma-Aldrich, St. Louis, Missouri, USA

3.1.4. Antibody

Table 4 *Antibody list*

Antibody	Function	Manufacturer and catalog number
HSP70	Western Blot / IHC	Cell Signaling Technology Cat#46447S
HSPA6	Western Blot	OriGene Cat#CF501950
β-actin	Western Blot	Santa Cruz Biotechnology Cat#sc-47778
Anti-mouse IgG-HRP	Western Blot	Southern Biotech Cat#1030-05
Biotinylated horse anti-mouse IgG	IHC	Vector Laboratories Cat# BA-2000
Mouse IgG1 control antibody	IHC	DAKO Cat# X0931
Rabbit anti-HSPA6	IHC	Invitrogen Cat# PA5-21726
Biotinylated goat anti-rabbit IgG	IHC	Vector Laboratories Cat# BA-1000
Rabbit IgG control	IHC	DAKO Cat# X0903

3.2. Method

3.2.1. Cell lines

The human epithelial ovarian cancer (EOC) cell line SKOV3 was obtained from the American Type Culture Collection (ATCC, Manassas, VA, USA). OAW42 and A2780 cells were kindly provided by the Institute of Anatomy, University Medical Center Hamburg-Eppendorf (UKE). OVCAR-8 cells were kindly provided by Dr. Volker Assmann (Institute of Tumor Biology, UKE)

OAW42 cells were cultured in Modified Eagle's Medium (MEM; Gibco, Grand Island, NY, USA), and SKOV3 cells were maintained in McCoy's 5A medium (Gibco), both supplemented with 10% (v/v) fetal calf serum (FCS; Biochrom AG, Merck Millipore, Darmstadt, Germany). OVCAR-8 and A2780 cells were maintained in RPMI-1640 medium (Gibco®, Thermo Fisher Scientific, Schwerte, Germany) with 10% (v/v) FCS. All cell lines were incubated at 37 °C in a humidified atmosphere containing 5% CO_2.

3.2.2. Workflow for isolation and culture of ascites-derived spheroids

Ascitic fluid was collected from patients at the time of debulking surgery. Samples were first centrifuged at 1200 rpm for 5 minutes at room temperature, and the cell pellet was resuspended in RBC (red blood cell) lysis buffer (eBioscience™, Invitrogen, USA) and incubated for 15 minutes at room temperature. After a second centrifugation at 1200 rpm for 5 minutes, all subsequent steps were performed on ice. The pellet was washed with PBS containing calcium and magnesium (PBS+/+), and the cell suspension was gently filtered through a 30 µm cell strainer (Falcon®, USA). The cell strainer was then inverted over a new 50 mL tube, and the retained material was flushed back from the strainer using PBS+/+. Spheroids >30 µm in diameter were collected in the new 50 mL tube and used for further experiments (Figure 5). Isolated spheroids were cultured in MCDB medium (MCDB 105 and Medium 199 mixed at a 1:1 ratio, supplemented with 10% FCS) and incubated at 37 °C in a humidified atmosphere containing 5% CO_2.

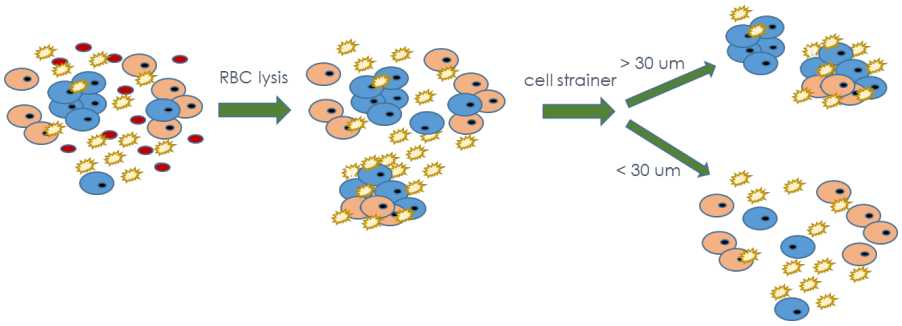

Figure 5 *Workflow for isolation of ascites-derived spheroids*

3.2.3. Workflow of tumoroids isolation and culture

Tumor tissue was obtained from surgical specimens. All subsequent steps were performed on ice to maintain cell viability. The tissue was mechanically minced into small pieces using sterile scissors in cold PBS(+/+). The resulting suspension was sequentially filtered through 100 µm and 30 µm cell strainers (Falcon®, USA). The 30 µm strainer was then inverted onto a new 50 mL tube, and the retained material was gently flushed back using PBS+/+. Tumoroids with diameters between 30 and 100 µm were collected and retained for further experiments (Figure 6). Tumoroids were cultured in MCDB medium (MCDB 105 and Medium 199 mixed at a 1:1 ratio, supplemented with 10% FCS) and incubated at 37 °C in a humidified atmosphere containing 5% CO_2.

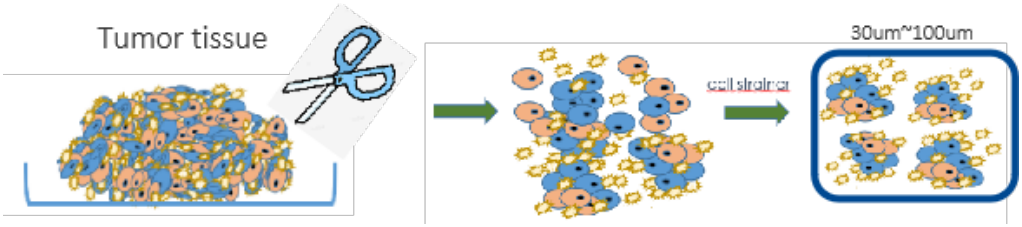

Figure 6 *Workflow for isolation of tumoroids*

3.2.4. Cell counts

A total of 10 µL of cell suspension was mixed with 10 µL of 0.04% trypan blue solution (1:1 dilution). The mixture was loaded into a Neubauer counting chamber, and viable (trypan blue-negative) and non-viable (trypan blue-positive) cells were counted using a Zeiss Axiovert 40C inverted phase-contrast microscope (Carl Zeiss, Oberkochen, Germany). Cells in four large squares of the counting grid were counted. The final cell concentration (cells/mL) was calculated using the following formula:

Cells/mL = (average number of cells per square) × (dilution factor) × 10^4

3.2.5. DNA isolation

Genomic DNA was extracted from cultured eukaryotic cells, mouse blood, and mouse tissue samples using the peqGOLD Tissue DNA Mini Kit (VWR, Germany). For all preparations, DNA was eluted in elution buffer pre-warmed to 70°C and stored at 4°C for short-term or –20°C for long-term storage.

For all sample types, DNA binding was performed by mixing lysates with absolute ethanol and applying them to silica spin columns. Columns were washed once with 500 µL HBC buffer (prepared with isopropanol) and twice with 700 µL DNA wash buffer (prepared with ethanol). After a drying centrifugation step, DNA was eluted in 200 µL (for cells and tissue) or 100 µL (for blood) of elution buffer pre-warmed to 70°C. A double elution step was performed by reloading the first eluate onto the column to maximize yield.

DNA extraction from cultured cells

Cell pellets were resuspended in 200 µL PBS, followed by addition of 25 µL proteinase K and 220 µL binding buffer. After vortexing, samples were incubated at 70°C for 10 minutes. Then, 220 µL ethanol was added before loading the lysate onto the spin column.

DNA extraction from mouse blood

A volume of 250 µL whole blood was mixed with 25 µL proteinase K and 250 µL BL buffer. After vortexing and incubation at 70°C for 10 minutes, 250 µL ethanol was added. The mixture was then applied to the spin column.

DNA extraction from tissue samples

Approximately 30 mg of tissue (lung or liver) was homogenized in 400 µL TL buffer with a 5 mm steel bead using a Precellys Evolution. 200 µL of the lysate was mixed with 200 µL TL buffer and 25 µL proteinase K, followed by incubation at 55°C for at least 1 hour. After digestion, 220 µL BL buffer and 220 µL ethanol were added before transferring the lysate to the spin column.

3.2.6. Human-specific Alu-qPCR

Alu-qPCR was performed following a protocol established at the Institute of Anatomy (UKE) (Haider et al., 2024). Genomic DNA was extracted from mouse blood, lung and liver, as well as from the human tumor cell suspension used for intraperitoneal (i.p.) injection. All DNA samples were diluted to 30 ng/µL prior to analysis. Human DNA in mouse matrices was quantified by SYBR Green–based Alu-qPCR on a QuantStudio™ 7 Real-Time PCR System (Applied Biosystems).

Standard curve and controls: A cell-equivalent standard curve ranging from 2,000 to 0 human cells per reaction was prepared in a constant background of mouse DNA; its composition and absolute cell numbers are shown in Table 5. A background control containing mouse DNA only was included on every plate.

qPCR reactions were run with PowerUp™ SYBR™ Green Master Mix (Applied Biosystems™ Lot: A25780). Primer sequences are listed in Tables 6. Reaction components, volumes, and the fast-cycling program used on QuantStudio are summarized in Table 7 and Table 8, respectively. Each well contained 2 µL of sample DNA; all standards and unknowns were run in technical triplicate.

Ct values were converted to human cell equivalents per reaction using the standard-curve regression and reported as cell equivalents per 2 µL (60 ng) input DNA.

Table 5 *Preparation of standard curve and control*

Standard curve	DNA from cells (µl)		Background control DNA (µl)	Absolute cell count
A	12.5 µl	+	50 µl	2000
B	2 µl from A	+	18 µl	200
C	2 µl from B	+	18 µl	20
D	2 µl from C	+	18 µl	2
E	2 µl from D	+	18 µl	0.2
F	2 µl from E	+	18 µl	0.02
G	2 µl from F	+	18 µl	0.002
H	--------	+	20 µl	0

Table 6 *Primers used for Alu-PCR*

Primer name	Sequence (5′–3′)
Alu - Forward	TGGCTCACGCCTGTAATCCA
Alu - Reverse	GCCACTACGCCCGGCTAATTT

Table 7 *Alu-pcr reaction components and volumes*

Component	Volume (µl)
PowerUp™ SYBR™ Green Master Mix(A25780)	10 µl
Alu Forward primer (10 pmol/µl)	4 µl
Alu Reverse primer (10 pmol/µl)	4 µl
DNA	2 µl

Table 8 *Reaction setup and cycling program (fast-cycling mode)*

Step	Temperature	Time	Cycles
UDG activation	50°C	2 minutes	1
Activation	95°C	2 minutes	1
Denature	95°C	1 second	40
Extend	60°C	30 seconds	

3.2.7. RNA isolation

Total RNA was extracted using the Qiagen RNeasy Mini Kit (Qiagen, Germany). All reagents were prepared as recommended, with RDD buffer and RNase-free water stored at 4 °C and DNase I at −20 °C. All procedures were performed under RNase-free conditions, and samples were kept on ice unless otherwise stated.

For cells, spheroids and tumoroids in suspension, samples were collected by centrifugation at 1200 rpm for 5 minutes and the supernatant was removed. For adherent cells, the medium was aspirated and cells were washed with PBS before lysis. In both cases, cells were lysed with 350 µL Buffer RLT, and the lysate was homogenised and transferred to microcentrifuge tubes.

An equal volume of 70% ethanol was added, mixed by gentle inversion, and up to 700 µL of the solution was loaded onto an RNeasy spin column. After centrifugation at ≥10,000 rpm for 30 seconds at room temperature, the flow-through was discarded. The column was washed with 350 µL RW1 buffer, incubated for 2 minutes at room temperature and centrifuged again.

For on-column DNase digestion, 70 µL of RDD buffer was mixed with 10 µL DNase I, and 80 µL of the mixture was applied to the column and incubated for 15 minutes. The column was then washed again with 350 µL RW1, followed by two washes with 500 µL RPE buffer, each including a 2-minute incubation. A final drying spin was performed at 13,000 rpm for 1 minute.

RNA was eluted in two steps. First, 25 µL of RNase-free water was added to the spin column, incubated for 3 minutes at room temperature and centrifuged at 13,000 rpm for 1 minute. The eluate was collected into a labelled RNase-free tube. A second elution was performed with the same volume of RNase-free water. RNA quantity and purity were measured using a NanoDrop spectrophotometer (Thermo Fisher Scientific, USA) by assessing the A260/A280 ratio (target range: 1.8–2.0), and samples were stored at −80 °C.

3.2.8. cDNA synthesis and RT-qPCR

Total RNA was reverse transcribed using the HighQu cDNA-Synthese Kit (HighQu; Cat# RTK0104). The reaction composition and program are provided in Tables 9 and 10. RT-qPCR was performed with qPCR Green ROX High Mix (2×) (HighQu; Cat# QPD0205). Each 20 µL reaction was set up in technical triplicate; the full composition and primer sequences are listed in Tables 11 and 12. Amplifications were run on a StepOne™ Real-Time PCR System (Applied Biosystems, Foster City, CA, USA) using the program shown in Table 13. All steps were performed under RNase-free conditions. Relative expression was calculated by the 2^−ΔΔCt method with GAPDH as the reference gene.

Table 9 *cDNA reaction components and volumes (total 20 µL)*

Component	Volume per reaction (µL)
5× Reaction Mix	4 µl
Reverse Blend (20×; DNase-free)	1 µl
RNA + RNase-free water (to 20 µL total)	up to 15 µl

Table 10 *cDNA thermal program*

Step	Temperature	Time
Reverse transcription	42°C	30 minutes
Inactivation	85°C	10 minutes
Hold	4°C	-

Table 11 *RT-qPCR reaction components and volumes (total 20 µL)*

Component	Volume (µl)
qPCR Green ROX High Mix (2×)	10 µl
Forward primer (10 pmol/µl)	0.4 µl
Reverse primer (10 pmol/µl)	0.4 µl
cDNA template	1 µl
Nuclease-free water	8.2 µl

Table 12 *Primers used for RT-qPCR*

Primer name	Sequence (5′–3′)
GAPDH - Forward	GTCAGTGGTGGACCTGACCT
GAPDH - Reverse	TGCTGTAGCCAAATTCGTTG
HSPA1A - Forward	AGCTGGAGCAGGTGTGTAAC
HSPA1A - Reverse	CAGCAATCTTGGAAAGGCCC
HSPA1B - Forward	TCAGGCCCTACCATTGAGGA
HSPA1B - Reverse	CCTTGAGTCCCAACAGTCCA
HSPA6 - Forward	GAGATCTCGTCCATGGTGCT
HSPA6 - Reverse	CGCTGCGAGTCATTGAAATA

Table 13 *Reaction setup and cycling program*

Step	Temperature	Time	Cycles
Holding	95°C	30 seconds	1
Denaturation	95°C	5 seconds	40
Extend	60°C	30 seconds	
Melt curve	95°C	10 seconds	1
	65°C	1 minute	1
	97°C	1 second	1

3.2.9. Protein extraction from cells, spheroids and tumoroids

Total protein was extracted from suspended spheroids, tumoroids and adherent cells using RIPA lysis buffer supplemented with protease and phosphatase inhibitors. All steps were carried out on ice unless otherwise specified.

For suspended spheroids and tumoroids, culture supernatants were collected and centrifuged at 1200 rpm for 5 minutes at room temperature. The resulting cell pellets were washed once with PBS and centrifuged again at 1200 rpm for 5 minutes.

For adherent cells, the monolayers were washed with PBS, then detached by trypsinisation at room temperature for 5 minutes. Detached cells were collected into 15 mL tubes containing an equal volume of culture medium (2:1 medium:trypsin) to neutralise trypsin. After centrifugation at 1200 rpm for 5 minutes, the cell pellets were washed once with PBS and centrifuged again at 1200 rpm for 5 minutes.

The final pellets were resuspended in RIPA buffer (65 mM Tris-HCl, pH 7.4; 154 mM NaCl; 1% Nonidet P-40 substitute; 1% sodium deoxycholate; 1 mM EDTA) supplemented with 1× protease inhibitor cocktail and 1× phosphatase inhibitor. The lysates were incubated on ice for 30 minutes, with brief vortexing every 5–10 minutes to enhance lysis. After centrifugation at 13,000 rpm for 5 minutes at 4 °C, the supernatants containing total soluble proteins were transferred to clean microcentrifuge tubes and stored at −80 °C for further analysis.

3.2.10. Protein quantification by BCA assay

Total protein concentrations were measured using the Pierce® BCA Protein Assay Kit (Thermo Scientific, USA), which relies on the reduction of Cu^{2+} ions by proteins and subsequent colourimetric detection via bicinchoninic acid. Bovine serum albumin (BSA) was used as the protein standard.

Protein lysates were diluted 1:5 in 50 mM Tris-HCl buffer. For each sample, 25 µL was loaded in triplicate onto a 96-well plate. A standard curve was generated from a 2000 µg/mL BSA stock solution by serial dilution in a mixture of RIPA buffer and 50 mM Tris-HCl (Table 14).

The working reagent was prepared by mixing Reagents A and B at a 50:1 ratio. Each well received 200 µL of this solution. After incubation at 37 °C for 45–60 minutes, absorbance was measured at 540 nm using a Sunrise™ plate reader with Magellan software (v6.6, Tecan Trading AG). Protein concentrations were calculated by interpolation from the BSA standard curve.

Table 14 *BSA standard concentrations for the BCA assay*

Standard curve	BSA concentration (µg/mL)	BSA stock (µL)	RIPA buffer (µL) + 50 mM Tris-HCl (µL)
A	1600	400 from stock	100 + 0
B	1000	500 from stock	200 + 300
C	800	200 from A	40 + 160
D	500	500 from B	100 + 400
E	250	500 from D	100 + 400
F	125	500 from E	100 + 400
G	62.5	500 from F	100 + 400
H	31.25	500 from G	100 + 400
Blank	-	-	20 + 80

3.2.11. Western blot

3.2.11.1. Gel electrophoresis

SDS–PAGE was performed in a discontinuous buffer system with a 10% separating gel and a 5% stacking gel (composition shown in Table 15). Glass plates were cleaned with ethanol, assembled with spacers and aligned using a spirit level. The separating gel was cast, overlaid with distilled water and allowed to polymerise for at least 45 minutes at room temperature. After removal of the water, the stacking gel was poured, a comb was inserted and the gel was left to polymerise for 30 minutes.

Protein samples (20 µg) were mixed 1:1 with 2× Laemmli sample buffer containing β-mercaptoethanol, heated at 95 °C for 5 minutes and briefly centrifuged. Samples were then loaded into the gel wells using low-retention pipette tips. A pre-stained protein ladder (CozyHi, HighQu) was used as the molecular weight marker.

Electrophoresis was performed at 58 V for approximately 18 hours in a vertical electrophoresis unit (SE600, Hoefer™) using 1× cathode and anode buffers prepared from the 10× stock solutions described in Table 16.

Table 15 *Composition of polyacrylamide gels*

Component	Separating gel (10%)	Stacking gel (5%)
87% Glycerol	8 g	–
Distilled water (Aqua dest)	17 mL	11.9 mL
3× Gel buffer with SDS	20 mL	4.7 mL
40% Acrylamide/Bis (AA/BAA)	15 mL	2.3 mL
10% APS	300 µL	225 µL
TEMED	30 µL	25 µL

Table 16 *Composition of electrophoresis buffers*

Buffer type	10× stock composition	pH	Preparation note
Cathode buffer	121.14 g Tris, 179.2 g Tricine; made up to 1 L with distilled water	8.25	Dilute 1:10 with distilled water for 1× working solution
Anode buffer	242.28 g Tris; made up to 1 L with distilled water	8.9	Dilute 1:10 with distilled water for 1× working solution
3× Gel buffer with SDS	181.7 g Tris; made up to 1 L with distilled water	8.45	Add 15 mL 10% SDS before use
0.5 M Tris buffer	6.05 g Tris; made up to 1 L with distilled water	6.8	Used for sample buffer preparation

3.2.11.2. Protein transfer, blocking and antibody incubation

After separation, proteins were transferred onto PVDF membranes. Membranes were activated in methanol for 1 minute, rinsed with distilled water and transferred by electroblotting at 1 A for 1 hour 45 minutes in 1× transfer buffer (10× stock; 121.41 g Tris, 144.89 g glycine, made up to 1 L with distilled water) using a blotting chamber.

Membranes were blocked with 5% non-fat milk in TBST (50 mM Tris, 150 mM NaCl, 0.05% Tween-20, pH 7.4) for 1 hour at room temperature and then incubated overnight at 4 °C with primary antibodies (diluted in 1.5% milk/TBST; see Table 17). After washing in TBST three times for 10 minutes each, membranes were incubated for 1 hour at room temperature with HRP-conjugated anti-mouse secondary antibody (diluted in 1.5% milk/TBST; Table 17), followed by washing in TBST four times for 10 minutes each.

Table 17 *Antibodies used for Western blot analysis*

Antibody	Vendor	Catalog #	Dilution
HSP70 (primary)	Cell Signaling Technology	46447S	1:1000 in TBST with 1.5% milk
HSPA6 (primary)	OriGene	CF501950	1:2000 in TBST with 1.5% milk
β-actin (primary)	Santa Cruz Biotechnology	sc-47778	1:4000 in TBST with 1.5% milk
Anti-mouse IgG-HRP (secondary)	Southern Biotech	1030-05	1:8000 in TBST with 1.5% milk

3.2.11.3. Detection, normalisation and quantification

Signals were visualised using the SuperSignal™ West Dura Extended Duration Substrate kit (Thermo Scientific™, USA; Cat# 34075, Lot# AC405132), and band intensities were quantified with a GS-800 Calibrated Densitometer (Bio-Rad, Hercules, CA). Protein expression levels were normalised to β-actin. All experiments were performed in independent biological triplicates, and densitometric values represent the mean ± standard deviation (SD).

3.2.11.4. Membrane stripping and re-blotting

Membranes previously subjected to immunodetection were rinsed in distilled water for 5 minutes and then incubated at room temperature for 25 minutes in a 1:10 dilution of Re-Blot Plus Mild Solution (Re-Blot Plus Western Blot Recycling Kit; Millipore, Cat. No. 2502) prepared in distilled water. After stripping, membranes were re-blotted with the respective primary and secondary antibodies, and signals were detected and quantified as described in Sections 3.2.11.2 and 3.2.11.3.

3.2.12. Immunohistochemical staining

3.2.12.1. HSP70 staining

Paraffin-embedded sections (4 µm) from ascites-derived spheroids or tumor tissues were deparaffinised in xylene and rehydrated through a graded ethanol series (100%, 90%, 80%) to distilled water. Antigen retrieval was performed in DAKO Target Retrieval Solution (pH 6.0; Agilent Technologies; Cat# S1699) at 90 °C for 30 minutes. After cooling to room temperature (RT), sections were washed in PBS, and endogenous peroxidase activity was blocked using 3% hydrogen peroxide in methanol for 10 minutes at RT. Non-specific binding was blocked with 10% normal horse serum (Vector Laboratories; Cat# S-2000) for 30 minutes at RT.

Slides were incubated overnight at 4 °C with mouse anti-HSP70 primary antibody (Cell Signaling Technology; Cat# 46447S) diluted 1:1000 in Antibody Diluent (DAKO Agilent Technologies; Cat# S0809). After washing in PBS three times for 5 minutes each, sections were incubated for 1 hour at RT with a biotinylated horse anti-mouse IgG secondary antibody (Vector Laboratories; Cat# BA-2000). Signal amplification was achieved using the VECTASTAIN® Elite ABC Kit (Vector Laboratories; Cat# PK-6100), followed by chromogenic development with the DAB Peroxidase Substrate Kit (Vector Laboratories; Cat# SK-4100) until optimal staining intensity was observed (3–5 minutes). After DAB development, slides were washed in distilled water twice for 5 minutes each to terminate the reaction.

Slides were counterstained with hematoxylin for 5 minutes, then rinsed in running tap water to blue the nuclei. They were dehydrated in 80%, 90%, and 100% ethanol (2 × 5 minutes each), cleared in xylene (2 × 5 minutes), and mounted with Eukitt mounting medium (Sigma-Aldrich; Cat# 03989). Parallel isotype control staining was performed using a mouse IgG1 control antibody (DAKO; Cat# X0931) to exclude non-specific binding.

3.2.12.2. HSPA6 staining

Parallel paraffin-embedded sections from the same ascites-derived spheroids or tumor tissues were deparaffinised and rehydrated as described in Section 3.2.12.1. Antigen retrieval was performed in freshly prepared 10 mM citrate buffer (pH 6.0) at 90 °C for 45 minutes. After cooling to RT and washing in PBS, sections were blocked with 10% normal goat serum (Vector Laboratories; Cat# S-1000) for 30 minutes at RT to block non-specific binding.

Slides were incubated overnight at 4 °C with rabbit anti-HSPA6 primary antibody (Invitrogen; Cat# PA5-21726) diluted 1:750 in Antibody Diluent (DAKO Agilent Technologies; Cat# S0809). After washing in PBS three times for 5 minutes each, slides were incubated with a biotinylated goat anti-rabbit IgG secondary antibody (Vector Laboratories; Cat# BA-1000) for 1 hour at RT. Signal amplification was performed using the VECTASTAIN® ABC-AP Kit (Vector Laboratories; Cat# AK-5000), followed by chromogenic development with the Permanent AP-Red Kit (Zytomed Systems; Cat# 001-125) until the desired signal intensity was achieved (approximately 5–10 minutes).

Slides were counterstained with hematoxylin for 5 minutes, rinsed in running tap water to blue the nuclei, and mounted with Aquatex (Merck; Cat# 1.08562.0050). Parallel isotype control staining was performed using a rabbit IgG control antibody (DAKO; Cat# X0903) to verify specificity.

3.2.12.3. Image acquisition and quantification

Images were acquired with an AxioVision 40 microscope (Carl Zeiss, Oberkochen, Germany) at 20× and 40× magnification. Stained sections were independently evaluated by two blinded observers. Staining intensity (0–3) and the percentage of positive cells (1: <25%, 2: 25–50%, 3: 50–75%, 4: >75%) were scored, and an immunoreactivity score (IRS, 0–12) was calculated as intensity × percentage score.

3.2.13. *In vivo* intraperitoneal xenograft experiments with HSP70 inhibitors

Female CB17/Icr-Prkdc^scid/IcrIcoCrl mice (6–8 weeks old; Charles River Laboratories) were used for intraperitoneal xenograft studies. All animal experiments were approved by the Institutional Animal Care and Use Committee of the University Medical Center Hamburg-Eppendorf (UKE) (Approval No. 2020/N97) and were conducted in accordance with institutional and national guidelines.

Mice were housed under specific pathogen-free (SPF) conditions in individually ventilated cages (IVCs) with autoclaved bedding and environmental enrichment. The animal facility was maintained at 24 ± 1 °C with 50–70% relative humidity and a 12-hour light–dark cycle. Sterilised food and water were provided ad libitum.

For tumor implantation, luciferase-expressing OVCAR8 cells (1×10^6 cells suspended in 200 µL sterile PBS) were injected intraperitoneally (i.p.). Intraperitoneal tumor engraftment and progression were monitored weekly using *in vivo* bioluminescence imaging (BLI) with an IVIS 200 system (PerkinElmer). Imaging was performed 10 minutes after injection of D-luciferin, and photon flux (photons/second/cm²/sr) was quantified using Living Image 3.2 software (PerkinElmer).

Three weeks after tumor cell inoculation, intraperitoneal tumor growth was confirmed by BLI, and mice were then randomised into four treatment groups (n = 5 per group) using stratified randomisation according to BLI signal intensity so that baseline tumor burden was comparable between groups. Treatments were administered intraperitoneally twice weekly for two consecutive weeks with the following regimens: control group (200 µL saline); cisplatin (5 mg/kg in 200 µL saline); cisplatin (5 mg/kg) plus VER-155008 (40 mg/kg; dissolved in saline with 0.1% DMSO); cisplatin (5 mg/kg) plus

Quercetin (50 mg/kg; dissolved in saline with 0.1% DMSO).

Body weight and general health status were monitored three times per week throughout the experimental period. At the end of the treatment course, mice were euthanised under deep ketamine/xylazine anaesthesia. The following biological specimens were collected: whole blood (via cardiac puncture), lungs, livers and macroscopic metastatic lesions. Specimens were either snap-frozen in liquid nitrogen or fixed in 4% paraformaldehyde (PFA) for subsequent analyses.

The primary endpoint was intraperitoneal tumor burden, quantified as total photon flux on terminal BLI imaging. Secondary endpoints included the extent of intraperitoneal tumor nodules, assessed using a modified Peritoneal Cancer Index (mPCI) (De Clercq et al., 2019, Bastiaenen et al., 2020), and the detection of disseminated tumor cells in blood and distant organs by human-specific Alu-qPCR. For mPCI scoring, each predefined peritoneal region was scored from 0 to 3 according to macroscopic tumor involvement: 0, no macroscopic tumor; 1, tumor nodules ≤ 2 mm; 2, tumor nodules 2–5 mm in diameter or > 5 nodules; and 3, tumor nodules ≥ 5 mm. If a single lesion spanned a regional boundary with a continuous length > 5 mm (or > one-third of the lesion’s largest diameter), the adjoining region was also scored. Micronodules on the mesentery were scored separately as follows: 1, < 10 nodules; 2, 10–20 nodules; and 3, > 20 nodules.

3.2.14. Lentiviral shRNA–mediated silencing of HSPA6 in OVCAR8 cells

3.2.14.1. shRNA constructs and bacterial amplification

Five Sigma-Aldrich MISSION® shRNA glycerol stocks targeting HSPA6 (RefSeq NM_002155.3) in the pLKO.1-puro backbone were screened in parallel: F11 (TRCN0000186110), F12 (TRCN0000161416), G2 (TRCN0000163622), G3 (TRCN0000163337) and G4 (TRCN0000161807) (common lot# SHCLNG09302403MN).

Glycerol stocks were streaked on LB–agar plates containing ampicillin (100 µg/mL) and incubated overnight at 37 °C. Single colonies were picked with sterile tips, replica-streaked onto a master plate and inoculated into LB broth supplemented with ampicillin. Cultures were grown for 12–16 hours at 37 °C with shaking (200–220 rpm) in ventilated 15-mL tubes.

3.2.14.2. Plasmid preparation and cleanup

Plasmid DNA was isolated using the Qiagen Plasmid Midi Kit (Lot# 163051488). Cultures were harvested using a pre-cooled centrifuge at 4 °C, with buffers P1 and P3 kept on ice. Cell pellets were resuspended in buffer P1, lysed in buffer P2 by gentle inversion, neutralised with buffer P3 on ice and clarified (13,000 rpm for 2 minutes at 4 °C). Supernatants were loaded onto midi columns, and plasmid DNA was eluted in Tris-HCl (pH 8.0). Where indicated, eluates were concentrated by isopropanol precipitation (1:1 isopropanol, 5 minutes on ice; 13,000 rpm for 30 minutes at 4 °C), washed with 70% ethanol (1 mL then 100 µL; 15 minutes and 10 minutes, respectively), air-dried (approximately 20 minutes at 30 °C) and dissolved in 50 µL Tris-HCl. DNA yield and purity were determined spectrophotometrically.

To remove residual salts and improve transfection efficiency, plasmid DNA was subjected to an additional cleanup using the QIAquick PCR Purification Kit

(Qiagen; Cat# 28104). Up to 10 µg of DNA per spin column were diluted 1:3 with nuclease-free water, mixed with 5 volumes of PB buffer, applied to the column, washed with 750 µL PE buffer and eluted twice with EB buffer (2 × 15 µL, 1-minute incubation at room temperature before each spin). Final DNA concentrations were recorded.

3.2.14.3. Lentivirus production in HEK cells

On day 1, HEK cells were seeded at 4 × 10^6 cells per 10-cm tissue culture dish to reach ~60–70% confluence on the day of transfection (one dish per virus). On day 2, cells at 60–70% confluence were transfected with the pLKO.1-puro shRNA plasmid (one of the five TRC clones), the packaging plasmid psPAX2 and the VSV-G envelope plasmid pMD2.G using Lipofectamine 2000. For each dish, Transfection Mix A contained 250 µL Opti-MEM, 2.2 µg psPAX2, 0.75 µg pMD2.G and 3 µg shRNA plasmid; Transfection Mix B contained 250 µL Opti-MEM and 15 µL Lipofectamine 2000. Mix B (265 µL) was added to Mix A, incubated for 15 minutes at room temperature and then applied to PBS-washed HEK cells overlaid with 5 mL Opti-MEM. After 4–6 hours at 37 °C, 3 mL fresh DMEM supplemented with 10% FCS were added, and incubation continued overnight.

Viral supernatants were collected approximately 24 hours after transfection (day 3), passed through a 0.45-µm syringe filter, and producer cells were replenished with 6 mL fresh DMEM + 10% FCS for an additional 24 hours. A second harvest was performed on day 4 using the same procedure. Filtered supernatants were aliquoted, labelled and stored at –80 °C.

3.2.14.4. Transduction of target OVCAR8 cells

In parallel with HEK transfection (day 2), OVCAR8 target cells were seeded in 6-well plates to reach 40–50% confluence on day 3. For each virus type, two infection conditions were set up on day 3 and repeated on day 4 (two 24-hour rounds):

Well 1: 1 mL fresh medium + 1 mL filtered viral supernatant + Polybrene (1:1000).

Well 2: 2 mL filtered viral supernatant + Polybrene (1:1000).

Selection control: 2 mL fresh medium only.

An additional negative control (NC) lentiviral solution obtained from an external laboratory was processed as a separate NC transduction group in parallel with the five knockdown (KD) virus conditions.

3.2.14.5. Puromycin selection

Seventy-two hours after the second transduction, antibiotic selection was initiated with puromycin (1 µg/mL). A non-transduced control well (medium only) was included to verify selection stringency; non-transduced cells died within 5–7 days.

3.2.15. Heat-shock induction and immunoblot validation of HSPA6 knockdown

Lentivirally transduced OVCAR8 polyclonal pools—four HSPA6-knockdown (KD) pools (TRC clones F11, F12, G3 and G4) and one non-targeting control (NC) pool—were subjected to heat shock at 42 °C for 2 hours in a humidified incubator with 5% CO_2 to induce HSPA6 expression. Cells were then harvested and processed for protein extraction and Western blotting as described in the ‘Protein extraction from cells, spheroids and tumoroids’ and ‘Western blot’ sections, using an anti-HSPA6 primary antibody with β-actin as a loading control. Band intensities were quantified by densitometry, and HSPA6 signals were normalised to β-actin. Knockdown efficiency for each TRC clone was expressed as the normalised HSPA6 signal relative to the NC pool under identical heat stressed conditions. Biological replicates were included, and data are presented as mean ± SD.

3.2.16. 2D Cell viability

OVCAR8-derived sublines were seeded at 4,000 cells per well in 96-well plates in RPMI-1640 supplemented with 1% FCS (100 µL per well). To minimize edge effects, outer wells were filled with approximately 100 µL ddH_2O, and plates included medium-only blanks (no cells) for background subtraction. After 24 hours of incubation at 37 °C in a humidified atmosphere with 5% CO_2, cells were treated once daily with cisplatin (3 µM) from Day 2 to Day 4 (total treatment duration 72 hours). At each dosing time point, 100 µL of medium was removed per well and replaced with 100 µL cisplatin-containing medium (3 µM, corresponding to 90.33 ng per 100 µL; calculated from a molecular weight of 301.1 g/mol). Untreated wells received medium without cisplatin (vehicle control).

At the 72-hour endpoint, 10 µL of WST-1 reagent was added per well and incubated at 37 °C for 1 hour. Plates were briefly shaken for 1 minute and air bubbles were removed before reading. Absorbance was measured at 450 nm (reference 650 nm) on a microplate reader. Raw values were blank-subtracted and normalised to the corresponding untreated controls (set to 100%). Each condition was performed in three independent biological replicates, each with at least three technical replicates per plate.

3.2.17. 3D Cell viability

To assess cisplatin sensitivity under three-dimensional (3D) culture conditions, OVCAR8-derived sublines were seeded at 4,000 cells per well into poly-HEMA–pre-coated 96-well plates (poly-HEMA 12 mg/mL in 95% ethanol, 100 µL per well) to prevent cell adhesion. Outer wells were filled with approximately 100 µL ddH_2O to minimize edge effects. Cells were cultured in RPMI-1640 supplemented with 1% FCS (100 µL per well) for 4 days to allow

cell aggregate formation. From Day 5, cisplatin (3 µM) was added once daily for three consecutive days.

After 3 days of treatment, CellTiter-Glo 3D reagent was added at a 1:1 ratio to the existing culture medium in each well, and cell aggregates were disrupted by pipetting up and down at least 10 times to ensure complete dissociation. Plates were then shaken for 10 minutes and subsequently incubated at room temperature (RT) for 10 minutes. Luminescence was recorded approximately 30 minutes after reagent addition on a luminescence microplate reader. Medium-only wells served as blanks; signals were background-subtracted and normalized to untreated controls (set to 100%). Each condition was performed in three independent biological replicates, each with at least three technical replicates per plate.

3.2.18. Establishment of luciferase-labelled OVCAR8 knockdown pools

OVCAR8 cells were first transduced with a lentiviral luciferase vector (LeGO-iNeo2-luc2) obtained from an external laboratory under the same transduction conditions described above. Seventy-two hours after transduction, selection with Geneticin (G418, 1 mg/mL) was initiated and maintained until non-transduced control cells were eliminated (approximately 5–7 days), yielding stable luciferase-positive pools (OVCAR8-LUC). These OVCAR8-LUC cells were then transduced with either the non-targeting control virus (shNC) or the HSPA6 shRNA TRC clone F12 virus, as described above, to generate stable polyclonal NC-LUC and KD(F12)-LUC pools for subsequent *in vivo* mouse experiments. Knockdown efficiency in these luciferase-labelled pools was confirmed after heat-stressed induction (42 °C for 2 hours) followed by Western blotting for HSPA6, as described above.

3.2.19. *In vivo* study with NC-LUC and KD-LUC xenografts

Female CB17/Icr-Prkdc^scid/IcrIcoCrl mice (6–8 weeks old; Charles River) were used for intraperitoneal (i.p.) xenograft studies. All procedures were approved by the Institutional Animal Care and Use Committee of the University Medical Center Hamburg-Eppendorf (UKE) (Approval No. 2020/N97) and were conducted under specific pathogen-free (SPF) conditions, as described above.

For tumor implantation, OVCAR8 cells stably expressing firefly luciferase (OVCAR8-LUC) were injected i.p. at 1×10^6 cells in 200 µL sterile PBS. Two experimental lines were established: 10 mice received non-targeting control cells (NC-LUC), and 10 mice received HSPA6-knockdown cells (F12; HSPA6-KD-LUC). Tumor engraftment and progression were monitored weekly by *in vivo* bioluminescence imaging (BLI) using an IVIS 200 system (PerkinElmer), as described above.

Four weeks after tumor cell inoculation, intraperitoneal tumor growth was confirmed by BLI. Mice were then stratified by BLI signal and randomised within each line (NC-LUC and HSPA6-KD-LUC) into a control group (200 µL saline) or a cisplatin group (5 mg/kg in 200 µL saline), administered i.p. once weekly for three consecutive weeks (n = 5 per arm). Body weight and clinical status were assessed three times per week throughout the treatment period.

At the end of the 3-week treatment course, mice were euthanized under deep ketamine/xylazine anaesthesia. Whole blood (cardiac puncture), primary intraperitoneal tumor nodules, liver, lungs and any macroscopic metastases were collected and either snap-frozen in liquid nitrogen or fixed in 4% PFA for subsequent analyses. The primary endpoint was intraperitoneal tumor burden, quantified as total photon flux on terminal BLI. Secondary endpoints included the extent of intraperitoneal tumor nodules, scored using a modified Peritoneal Cancer Index (mPCI) with the same scoring system as described above, terminal total tumor volume (TTV, sum of macroscopic intraperitoneal nodules

at necropsy, with tumor volume calculated using the ellipsoid estimation formula V = height × width × length × π / 6) (Busch et al., 2009, Tomayko and Reynolds, 1989) and detection of disseminated tumor cells in blood and distant organs by human-specific Alu-qPCR.

3.2.20. Statistical analysis

Statistical analyses were performed using GraphPad Prism (GraphPad Software, San Diego, CA, USA). Data are presented as mean ± SD unless stated otherwise; skewed variables were log10-transformed or summarised as median (range). Comparisons between two groups were performed using two-tailed unpaired or paired Student's t-tests, as appropriate. For non-normally distributed or ordinal data, the Mann–Whitney U test was applied. For experiments involving more than two groups or factorial designs, one-way or two-way ANOVA with Tukey's or Dunnett's multiple-comparison tests was used, as specified in the figure legends. Correlations were assessed using Pearson's or Spearman's coefficients, as indicated in the corresponding figure legends. All tests were two-sided and $p < 0.05$ was considered statistically significant. In the figures, statistical significance is denoted as follows: * $p < 0.05$; ** $p < 0.01$; *** $p < 0.001$; **** $p < 0.0001$.

4. Results

4.1. Western blot quantification of stress-inducible HSP70 isoforms in matched patient samples

In order to validate the increased expression of three HSP70 family members in ascites-derived spheroids at the protein level, we performed western blot analysis on matched patient samples. These experiments used the same set of matched spheroids and primary tumour tissue samples as those illustrated previously in the Introduction and were extended by the inclusion of patient-derived tumoroids. Because tumour tissues contain abundant tumour-associated stroma that may dilute tumour cell–derived HSP70 signals, tumoroids were additionally analysed as tumour cell aggregates that are more comparable to ascites-derived spheroids and less influenced by stromal components. Western blots were performed on matched patient samples with lanes labelled S (ascites-derived spheroids), T (primary tumor tissue), and Tm (patient-derived tumoroids). After densitometric analysis, HSAPA1/B1 and HSP60 band intensities were normalized to corresponding ß-actin and S was set to 100% in each sample pair. T and Tm were analysed together as a combined group (T/Tm). Representative blots are shown in Figure 7A. In Figure 7B, HSPA1A/B in T/Tm averaged 74.77% ± 37.80 SD relative to S (n = 16 pairs; paired two-tailed t-test, p = 0.0175). HSPA6 in T/Tm averaged 17.60% ± 22.06 SD relative to S (n = 11 pairs; paired two-tailed t-test, p < 0.0001). Thus, both isoforms were significantly higher expressed in S than in T/Tm, with the relative reduction in T/Tm being more pronounced for HSPA6 than for HSPA1A/B.

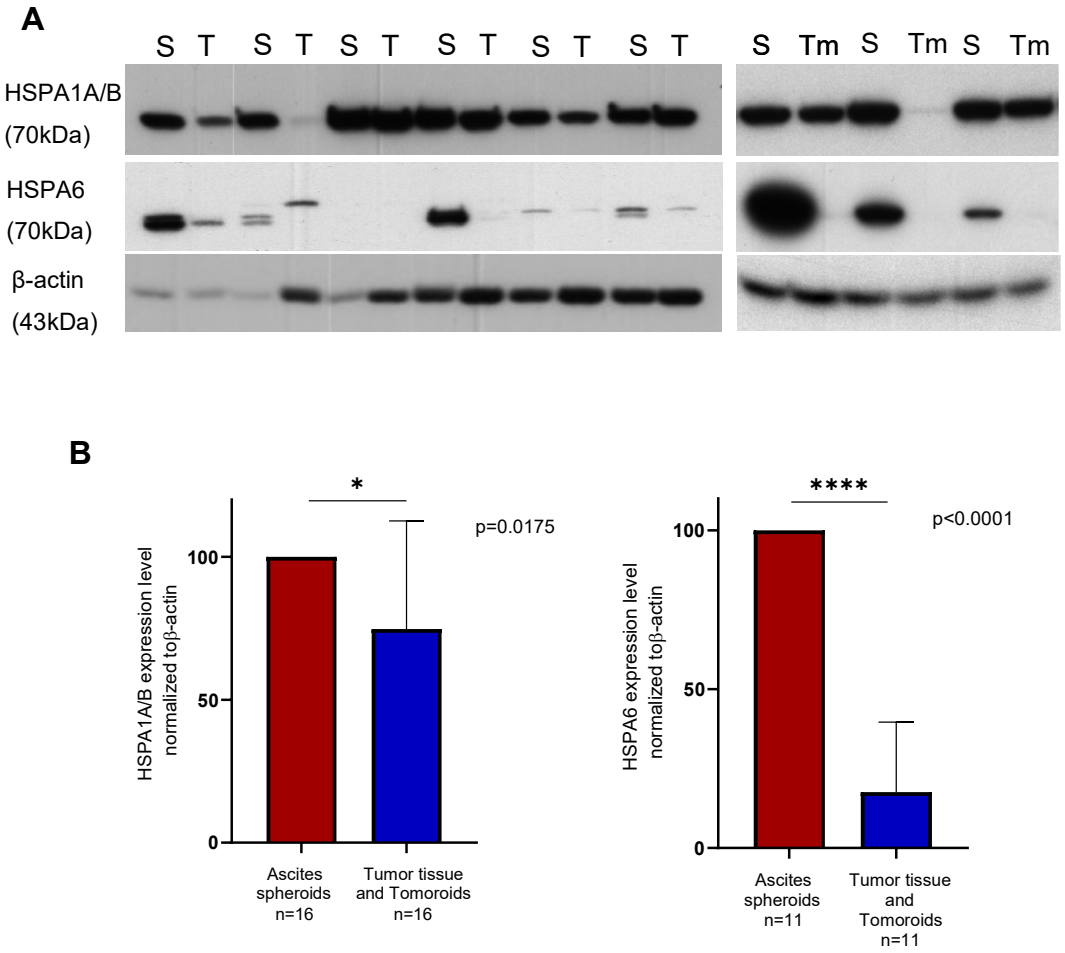

Figure 7 *Western blot analysis of stress-inducible HSP70 isoforms in matched patient samples*

A. Representative immunoblots for HSPA1A/B (~70 kDa) and HSPA6 (~70 kDa) from matched samples: ascites-derived spheroids (S), primary tumor tissue (T), and patient-derived tumoroids (Tm). β-actin (43 kDa) served as the loading control.

B. Paired densitometric quantification normalized to β-actin shows higher expression in spheroids (HSPA1A/B: n = 16 pairs, p = 0.0175; HSPA6: n = 11 pairs, p < 0.0001).

* p < 0.05; ** p < 0.01; *** p < 0.001; **** p < 0.0001.

4.2. IHC-based spatial and quantitative assessment of HSP70-family protein expression in matched patient samples

Given the increased expression of HSPA1A/B and HSPA6 in ascites-derived spheroids at the mRNA and protein levels, immunohistochemistry (IHC) was used to assess the spatial distribution of these proteins in matched patient samples and to determine which tumour cell compartments contributed to the signal. IHC for HSPA1A/B and HSPA6 was performed on FFPE material from ascites-derived spheroids and corresponding primary tumor tissues from 27 patients. Staining was scored using the immunoreactive score (IRS; intensity × proportion; range 0–12). For each marker, representative fields and the corresponding quantitative analyses are shown.

For HSPA1A/B, representative pictures are shown in Figure 8A (DAB chromogen, scale bar 100 µm). Ascites-derived spheroids showed stronger and more uniform cytoplasmic labeling, whereas the corresponding tumor tissues displayed more heterogeneous and often weaker staining. Quantitatively (Figure 8C), spheroids had a higher mean IRS (9.72 ± 2.56) than tumor tissues (7.94 ± 2.97). In paired analyses, spheroids scored higher than their matched tumors with a mean paired difference of 1.781 ($p = 0.0065$). The paired line plot (Figure 8C, right) shows that, in most pairs, IRS values are higher in spheroids than in the corresponding tumor samples.

For HSPA6, representative micrographs are shown in Figure 8B (AP-Red chromogen, scale bar 100 µm). Ascites-derived spheroids exhibited intense, compact cytoplasmic staining, whereas the corresponding tumor tissues showed more heterogeneous labelling, with strongly stained small tumor areas and largerer ones showing weak or no staining. Quantitatively (Figure 8D), spheroids had a mean IRS of 11.43 ± 1.14 compared with 8.15 ± 2.31 in tumor tissues. In paired analyses, spheroids exceeded their matched tumors by a mean paired difference of 3.272 ($p < 0.0001$). The paired line plot (Figure 8D,

right) demonstrates a consistent within-pair increase in IRS from tumor tissue to spheroids in almost all cases.

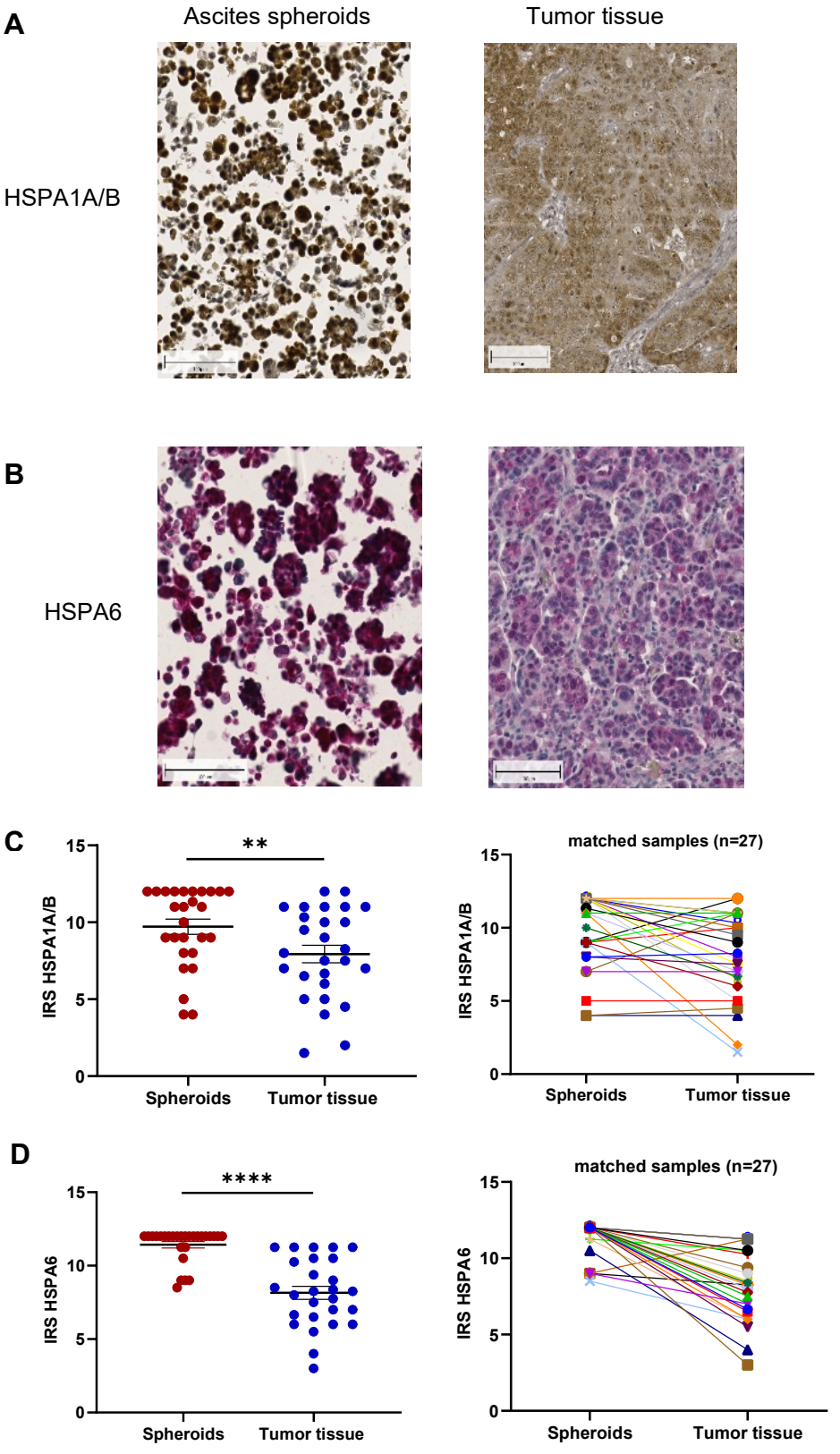

Figure 8 *IHC demonstrates higher HSP70-family expression in ascites-derived spheroids than in matched tumor tissue*

A. Representative IHC for HSPA1A/B in ascites-derived spheroids (left) and tumor tissue (right); chromogen DAB; scale bar 100 µm.

B. Representative IHC for HSPA6 in ascites-derived spheroids (left) and tumor tissue (right); chromogen AP-Red; scale bar 100 µm.

C. HSPA1A/B IRS quantification (n = 27 matched pairs). Left, scatter with mean ± SD (spheroids 9.72 ± 2.56; tumor tissue 7.94 ± 2.97), paired two-tailed t-test: p = 0.0065. Right, paired line plot.

D. HSPA6 IRS quantification (n = 27 matched pairs). Left, scatter with mean ± SD (spheroids 11.43 ± 1.14; tumor tissue 8.15 ± 2.31), paired two-tailed t-test: p < 0.0001. Right, paired line plot.

* p < 0.05; ** p < 0.01; *** p < 0.001; **** < 0.0001.

4.3. qPCR and Western blot profiling of stress-inducible HSP70 isoforms in ovarian cancer cell lines versus patient-derived spheroids

To characterise how stress-inducible HSP70 isoforms are expressed in standard ovarian cancer cell line relative to patient-derived ascites spheroids, we quantified HSPA1A, HSPA1B, and HSPA6 transcripts by qPCR and HSPA1A/B and HSPA6 proteins by Western blot (β-actin normalization) across four ovarian cancer cell lines (OVCAR8, SKOV3, A2780, OAW42) and four patient-derived ascites spheroid samples (TB6707, TB6759, TB6498, TB6624). Within each experiment, values were expressed relative to a common reference (OVCAR set to 1.0); comparisons focus on cell lines versus patient-derived spheroids (see Figure 9 for all panels).

4.3.1. mRNA expression patterns in ovarian cancer cell lines and patient-derived spheroids

For HSPA1A (Figure 9A), among the four ovarian cancer cell lines, HSPA1A transcript abundance was highest in OVCAR8 (set to 1.0) and markedly lower in SKOV3, A2780 and OAW42 (all <0.2-fold of OVCAR8). In contrast, patient-derived spheroids showed a broader and generally higher range of

expression: TB6707 and TB6498 displayed pronounced upregulation (18-fold and 2.6-fold, respectively, relative to OVCAR8), TB6759 expressed HSPA1A at a level similar to OVCAR8, whereas TB6624 remained low.

For HSPA1B (Figure 9B), transcripts showed a pattern similar to HSPA1A. Among the four ovarian cancer cell lines, OVCAR8 again displayed the highest expression (set to 1.0), with OAW42 at an intermediate level (0.67-fold) and SKOV3 and A2780 clearly lower (0.31-fold and 0.14-fold, respectively). In contrast, patient-derived spheroids contained samples with high expression: TB6707 showed a 23-fold increase and TB6498 a 4-fold higher HSPA1B mRNA level compared with OVCAR8, whereas TB6759 and TB6624 remained in the low-to-intermediate range (0.66-fold and 0.34-fold, respectively).

For HSPA6 (Figure 9C), OVCAR8 again showed the highest transcript level among the four ovarian cancer cell lines (set to 1.0), with OAW42 at an intermediate level (0.53-fold), SKOV3 lower (0.33-fold) and A2780 displaying near-undetectable expression (0.02-fold). In contrast, patient-derived spheroids included several higher-expressing samples: TB6707 showed a 3.6-fold upregulation relative to OVCAR8, TB6759 exceeded OVCAR8 by 1.4-fold, TB6498 was slightly lower than OVCAR8 (0.75-fold) and TB6624 fell into the low-expression range (0.20-fold).

Taken together, these qPCR data show that ascites-derived spheroids tend to exhibit higher mRNA levels of all three stress-inducible HSP70 isoforms (HSPA1A, HSPA1B and HSPA6) than established ovarian cancer cell lines, with some spheroid samples showing particularly high expression.

4.3.2. Protein expression patterns across cell lines and spheroids

For HSPA1A/B (Figure 9D), Western blot analysis revealed a similar pattern at the protein level. Among the four ovarian cancer cell lines, HSPA1A/B abundance was highest in OVCAR8 (set to 1.0), with lower levels in SKOV3 and A2780 (0.50-fold and 0.35-fold, respectively) and an intermediate level in

OAW42 (0.67-fold). In contrast, patient-derived spheroids showed consistently higher HSPA1A/B protein expression: TB6707 and TB6759 reached nearly three-fold levels compared with OVCAR8 (2.8-fold each), while TB6498 and TB6624 displayed moderately elevated levels of about 1.3-fold.

For HSPA6 (Figure 9E), Western blot quantification revealed very low HSPA6 protein in OVCAR8 (reference 1.0), whereas SKOV3, A2780 and OAW42 already showed higher levels (16-fold, 25-fold and 59-fold, respectively). Patient-derived spheroids displayed an extreme up-regulation compared with both OVCAR8 and the cell-line panel: TB6707, TB6759 and TB6498 reached 1.1×10^4-fold, 3.6×10^3-fold and 1.2×10^3-fold of the OVCAR8 level, and even the lowest spheroid, TB6624, remained 2.7×10^2-fold above OVCAR8.

Overall, these Western blot data demonstrate that ascites-derived spheroids exhibit markedly higher protein levels of stress-inducible HSP70 isoforms than ovarian cancer cell lines, with HSPA6 showing the strongest enrichment.

4.3.3. Concordance between mRNA and protein levels of stress-inducible HSP70 isoforms

Across all ovarian cancer cell lines and patient-derived spheroids, both HSPA1A and HSPA1B mRNA levels (x-axis, log10) showed only moderate concordance with HSPA1A/B protein abundance (y-axis). For HSPA1A (Figure 9F), the correlation coefficient was $r = 0.6433$ with $p = 0.0853$, and for HSPA1B (Figure 9G) $r = 0.6196$ with $p = 0.1014$, indicating a positive but non-significant association between transcript and protein levels for these two isoforms.

In contrast, HSPA6 mRNA correlated very tightly with HSPA6 protein levels (Figure 9H; protein on a log10 y-axis), yielding $r = 0.967$ with $p < 0.0001$. Thus, among the stress-inducible HSP70 isoforms analysed, HSPA6 displayed a close and statistically significant correlation between mRNA and protein levels across the combined panel of cell lines and patient-derived spheroids.

A

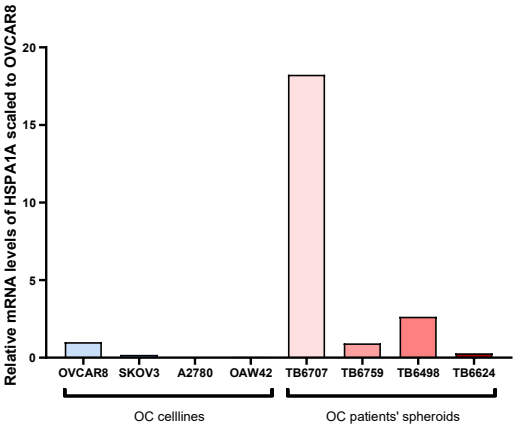
Relative mRNA levels of HSPA1A scaled to OVCAR8
20
15
10
5
0
OVCAR8 SKOV3 A2780 OAW42 TB6707 TB6759 TB6498 TB6624
OC celllines
OC patients' spheroids

B

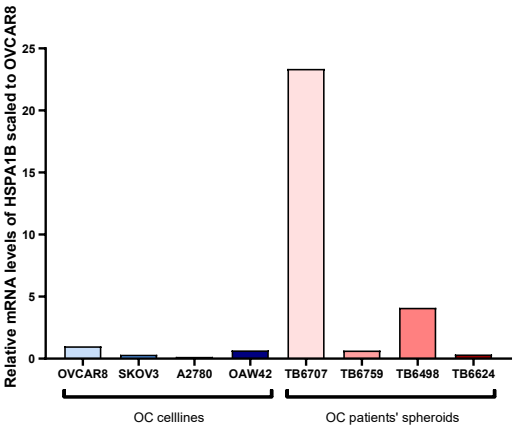
Relative mRNA levels of HSPA1B scaled to OVCAR8
25
20
15
10
5
0
OVCAR8 SKOV3 A2780 OAW42 TB6707 TB6759 TB6498 TB6624
OC celllines
OC patients' spheroids

C

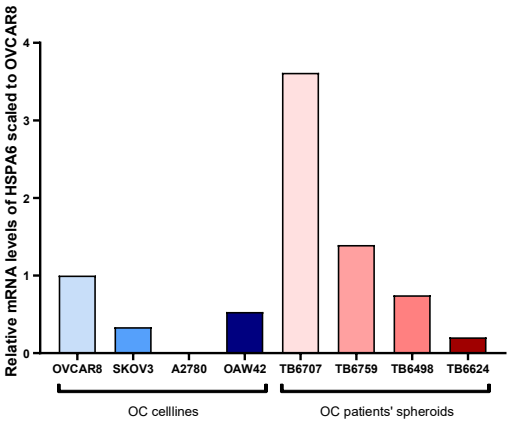
Relative mRNA levels of HSPA6 scaled to OVCAR8
4
3
2
1
0
OVCAR8 SKOV3 A2780 OAW42 TB6707 TB6759 TB6498 TB6624
OC celllines
OC patients' spheroids

D

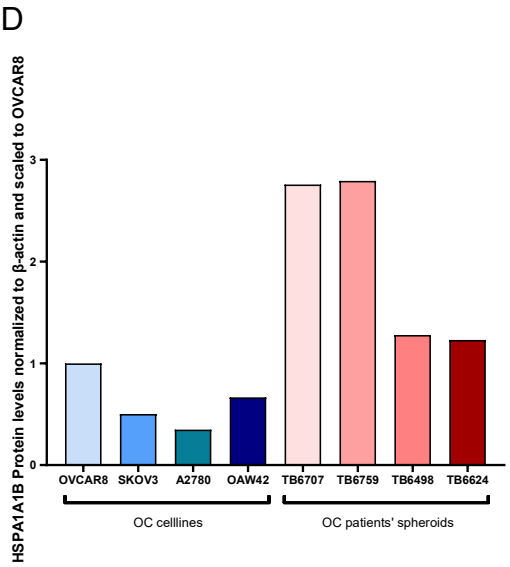
HSPA1A1B Protein levels normalized to β-actin and scaled to OVCAR8
3
2
1
0
OVCAR8 SKOV3 A2780 OAW42 TB6707 TB6759 TB6498 TB6624
OC celllines
OC patients' spheroids

E

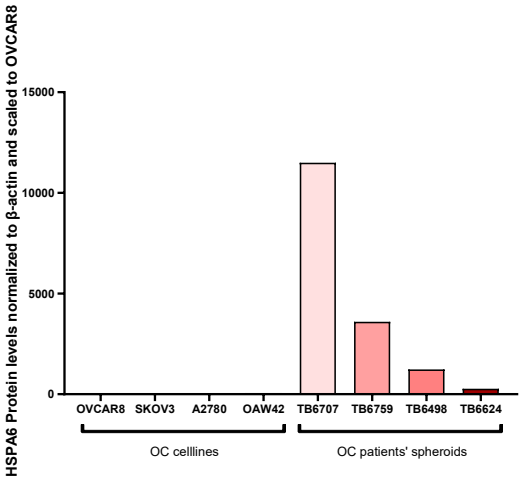
HSPA6 Protein levels normalized to β-actin and scaled to OVCAR8
15000
10000
5000
0
OVCAR8 SKOV3 A2780 OAW42 TB6707 TB6759 TB6498 TB6624
OC celllines
OC patients' spheroids

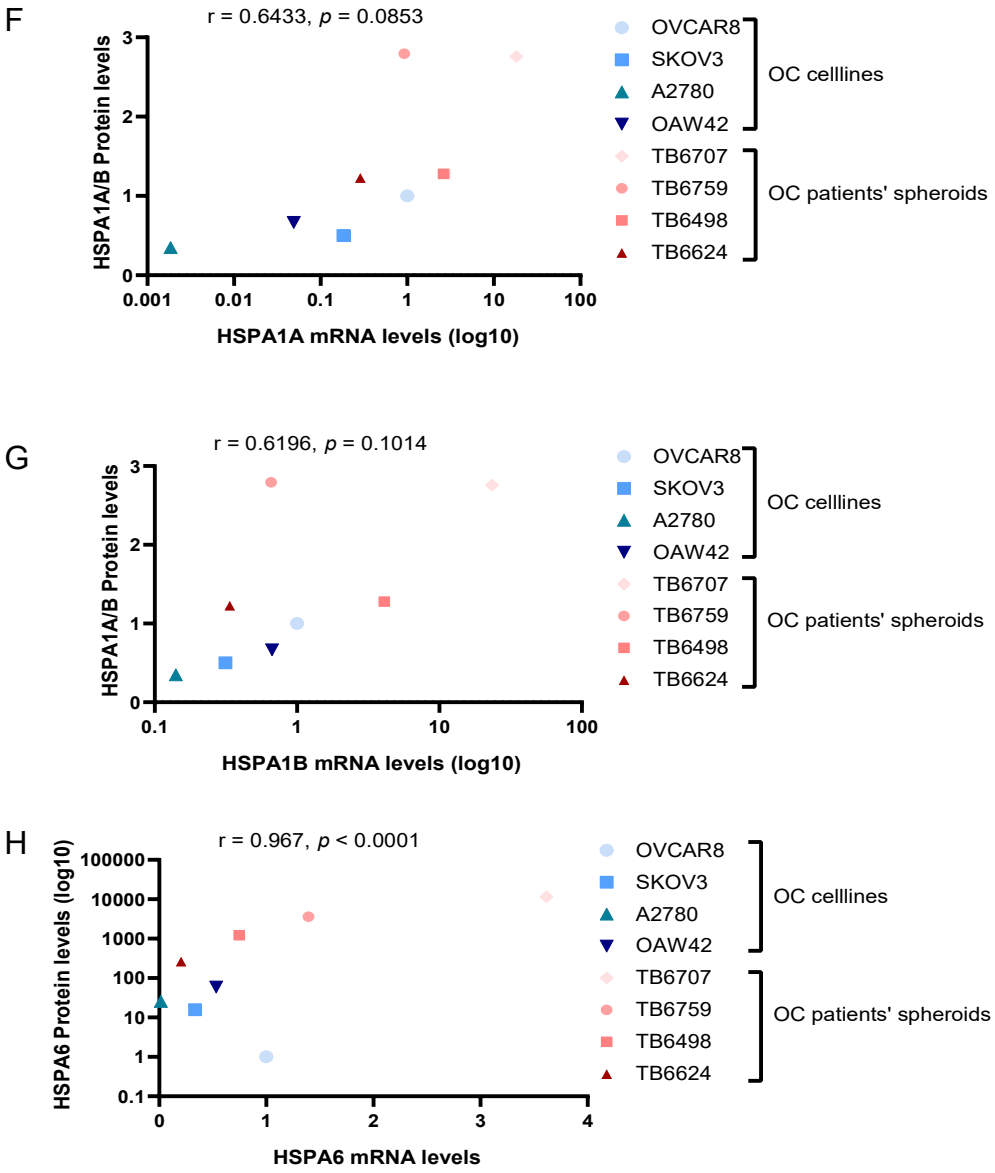

Figure 9 *RNA and protein levels of stress-inducible HSP70 isoforms in ovarian cancer cell lines and patient-derived ascites spheroids*

A–C. Relative mRNA levels of HSPA1A (A), HSPA1B (B) and HSPA6 (C) measured by qPCR in four ovarian cancer cell lines (OVCAR8, SKOV3, A2780, OAW42) and four patient-derived spheroid samples (TB6707, TB6759, TB6498, TB6624). Expression values are normalized to OVCAR8 (set to 1.0).

D–E. Relative protein levels of HSPA1A/B (D) and HSPA6 (E) determined by Western blot, normalized to β-actin and expressed relative to OVCAR8.

F–H. Correlation between mRNA and protein levels for HSPA1A (F), HSPA1B (G) and HSPA6 (H) across the same panel of samples. HSPA1A and HSPA1B mRNA levels (x-axis, log10) are plotted against HSPA1A/B protein abundance (y-axis); HSPA6 mRNA (x-axis) is plotted against HSPA6 protein levels (y-axis, log10). Cell lines and spheroids are indicated by distinct symbols and colors as shown in the legend; Pearson correlation coefficient (r) and two-sided p values are reported in each panel.

4.4. *In vivo* efficacy of pharmacologic HSP70 inhibition in an intraperitoneal ovarian cancer xenograft model

Based on the in vitro data demonstrating that pharmacologic HSP70 inhibition enhances cisplatin-induced cytotoxicity in ovarian cancer cell lines and patient-derived ascites spheroids, the next step was to evaluate these combinations in vivo in an intraperitoneal ovarian cancer xenograft model. Female CB17/Icr-Prkdc^scid/IcrIcoCrl mice bearing intraperitoneal luciferase-expressing OVCAR8 xenografts were randomized 3 weeks after inoculation into four treatment groups (n = 5 per group) stratified by baseline bioluminescence imaging (BLI): control, cisplatin (5 mg/kg), cisplatin + VER-155008 (40 mg/kg) and cisplatin + Quercetin (50 mg/kg). All drugs were administered intraperitoneally twice weekly. After two weeks of treatment, the experiment was terminated because some mice developed severe adverse effects (four doses in total; Figure 10A). Tumor burden was monitored over time by IVIS and quantified as total photon flux (Figure 10B). At necropsy, intraperitoneal disease was scored using the modified Peritoneal Cancer Index (mPCI). In addition, peripheral blood, lung and liver were collected for human-specific Alu-qPCR to detect and quantify disseminated human tumor cells in the circulation and distant organs.

4.4.1. Bioluminescence-based assessment of intraperitoneal tumor growth

At day 14 of treatment, tumor progression by BLI was calculated as the percentage change in total photon flux relative to baseline (D14/D0 × 100%; Figure 10C). The control group showed the largest increase in BLI signal (mean 556.8% of baseline), whereas all cisplatin-containing regimens markedly restricted signal growth (cisplatin 179.9%, cisplatin + VER-155008 123.1% and cisplatin + Quercetin 131.4%). One-way ANOVA with Tukey’s multiple-comparisons test demonstrated that each cisplatin-based arm

significantly reduced the BLI increase compared with the control group (control vs cisplatin, p = 0.0293; control vs cisplatin + VER-155008, p = 0.0113; control vs cisplatin + Quercetin, p = 0.0131). In contrast, direct comparisons between cisplatin and the two combination regimens did not show further reductions in BLI signal (cisplatin vs cisplatin + VER-155008, p = 0.9640; cisplatin vs cisplatin + Quercetin, p = 0.9771).

For the BLI time course (Figure 10D), tumor growth was plotted as percentage BLI relative to day 0 (set to 100% for all groups). The control group showed a progressive rise in signal from approximately 130% at day 7 to approximately 560% at day 14, with noticeable variability between mice. Cisplatin alone initially kept BLI close to baseline (around 100% at day 7) but still increased to around 180% by day 14. By contrast, both cisplatin + VER-155008 and cisplatin + Quercetin, the two HSP70 inhibitor combinations, maintained overall lower signals: the cisplatin + VER-155008 group dropped below baseline at day 7 (about 63%) and rose only modestly to about 123% at day 14, whereas the cisplatin + Quercetin group showed the flattest course, remaining close to baseline throughout (about 113% at day 7 and 131% at day 14). Although statistical comparisons between the cisplatin-containing regimens did not reveal significant differences, these time-course profiles are consistent with a more sustained suppression of intraperitoneal tumor BLI signal when cisplatin is combined with either VER-155008 or Quercetin.

A

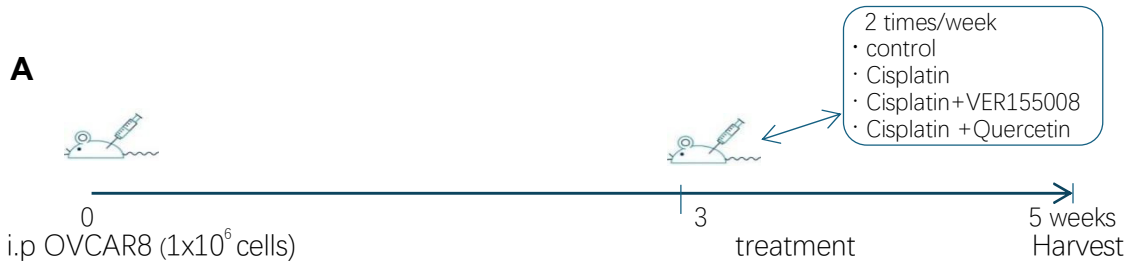
2 times/week
· control
· Cisplatin
· Cisplatin+VER155008
· Cisplatin +Quercetin
0
i.p OVCAR8 (1x10^6 cells)
3
treatment
5 weeks
Harvest

B

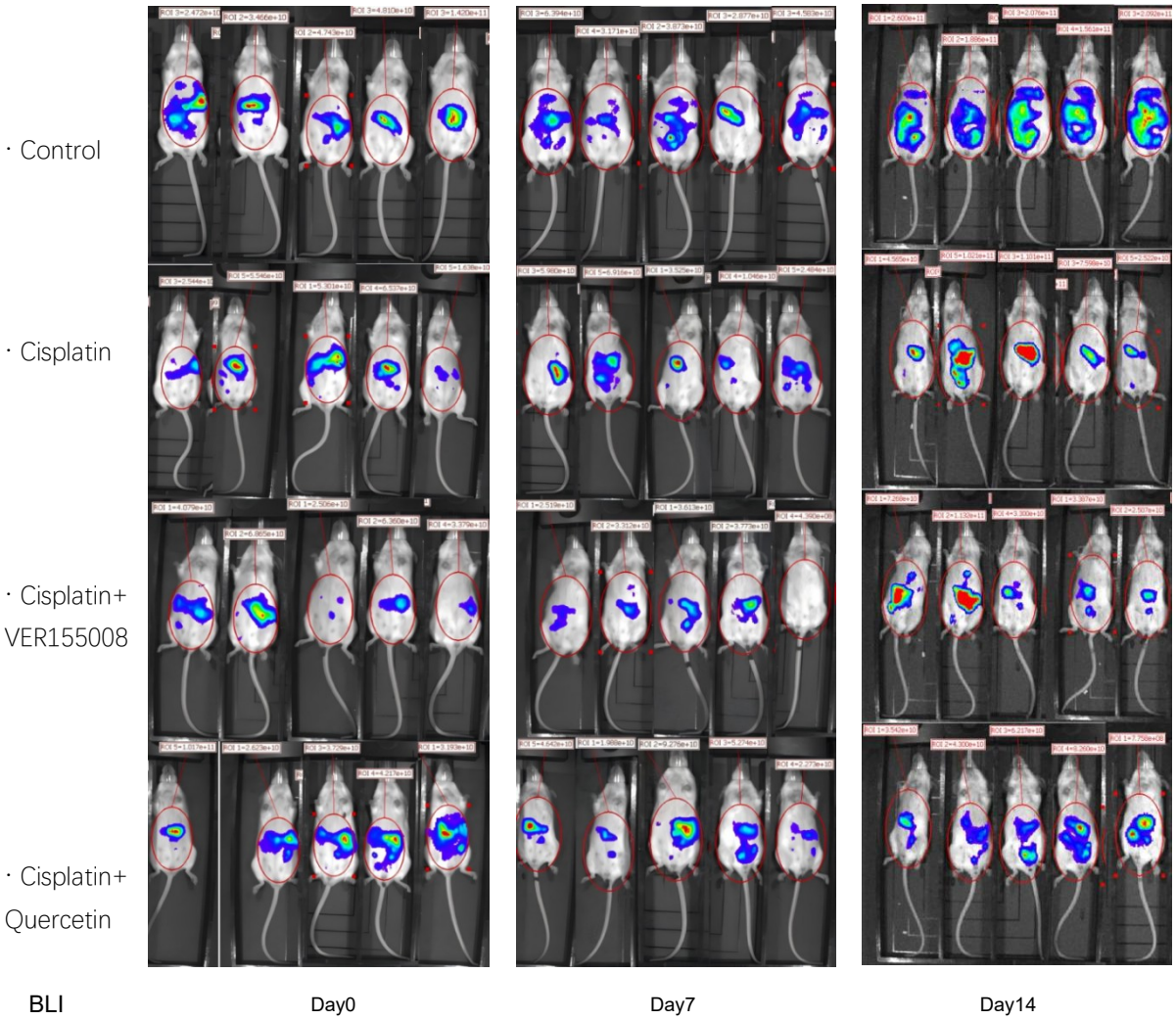
· Control
· Cisplatin
· Cisplatin+ VER155008
· Cisplatin+ Quercetin
BLI
Day0
Day7
Day14

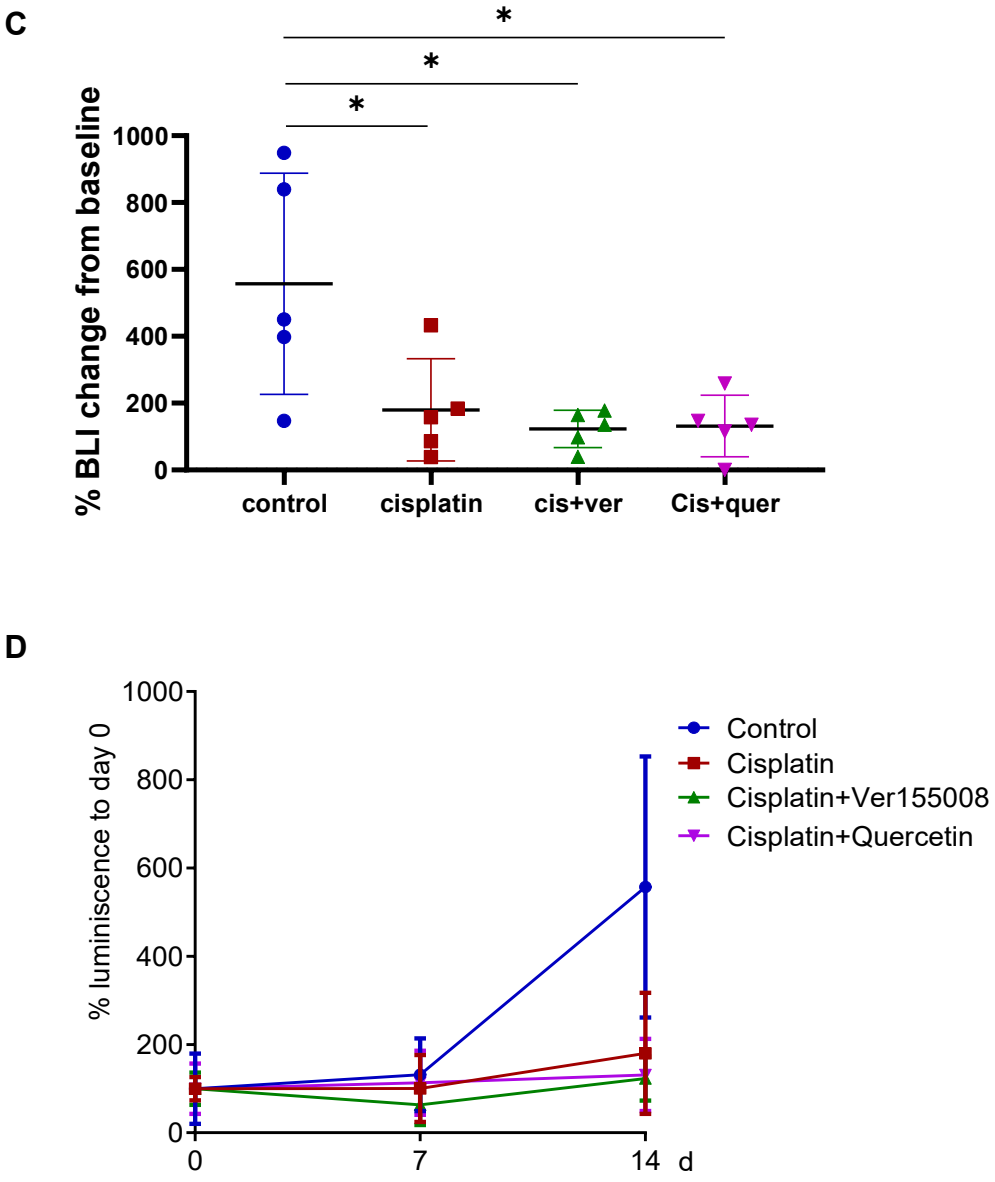

Figure 10 *In vivo efficacy of HSP70 inhibition in a peritoneal ovarian cancer xenograft model*

A. Schematic overview of the *in vivo* treatment schedule in the intraperitoneal OVCAR8 xenograft model, showing randomization into four groups (control, cisplatin, cisplatin + VER-155008, cisplatin + Quercetin) and timing of i.p. treatments and necropsy.

B. Representative serial IVIS images from each group at days 0, 7 and 14, showing intraperitoneal tumor burden as total photon flux.

C. Percentage change in BLI at day 14 relative to day 0 (D14/D0 × 100%) in each treatment group. Symbols represent individual mice; bars indicate mean ± SD.

D. Time course of BLI during treatment, expressed as % BLI relative to day 0 (mean ± SD).

* $p < 0.05$; ** $p < 0.01$; *** $p < 0.001$; **** $p < 0.0001$.

4.4.2. Necropsy-based intraperitoneal tumor burden and its correlation with BLI

At necropsy, intraperitoneal tumor burden was quantified using a Modified Peritoneal Cancer Index (mPCI), in which the peritoneal cavity was divided into nine regions and each region was scored from 0 to 3 according to the size and number of tumor nodules (see Methods for details; Figure 11A). The control group showed the highest mPCI scores (mean 7.4 ± 1.3; range 6–9), whereas all cisplatin-containing regimens showed lower values (cisplatin 4.2 ± 1.6, cisplatin + VER-155008 3.8 ± 1.5, cisplatin + Quercetin 3.2 ± 0.8; Figure 11B). One-way ANOVA with Tukey's multiple comparisons test confirmed that each cisplatin-based arm significantly reduced mPCI compared with the control group (control vs cisplatin, $p = 0.0091$; control vs cisplatin + VER-155008, $p = 0.0035$; control vs cisplatin + Quercetin, $p = 0.0009$). Direct comparisons among the cisplatin-containing groups did not reach statistical significance (cisplatin vs cisplatin + VER-155008, $p = 0.9656$; cisplatin vs cisplatin + Quercetin, $p = 0.6579$). Nonetheless, both cisplatin + VER-155008 and cisplatin + Quercetin tended to yield lower mPCI scores than cisplatin alone, with the lowest values observed in the cisplatin + Quercetin group.However, this apparent additional reduction of peritoneal tumor burden did not reach statistical significance in this small cohort.

At study end, BLI signal (log10 total photon flux on the y-axis) correlated positively with the total mPCI score across all treatment groups (Spearman $r = 0.7066$; 95% CI, 0.3722–0.8787; $p = 0.0005$; $n = 20$; Figure 11C). Thus, mice with higher bioluminescent signals also tended to have higher mPCI scores, indicating good agreement between imaging-based and necropsy-based assessments of intraperitoneal tumor burden and supporting mPCI as a reliable semiquantitative readout in this model.

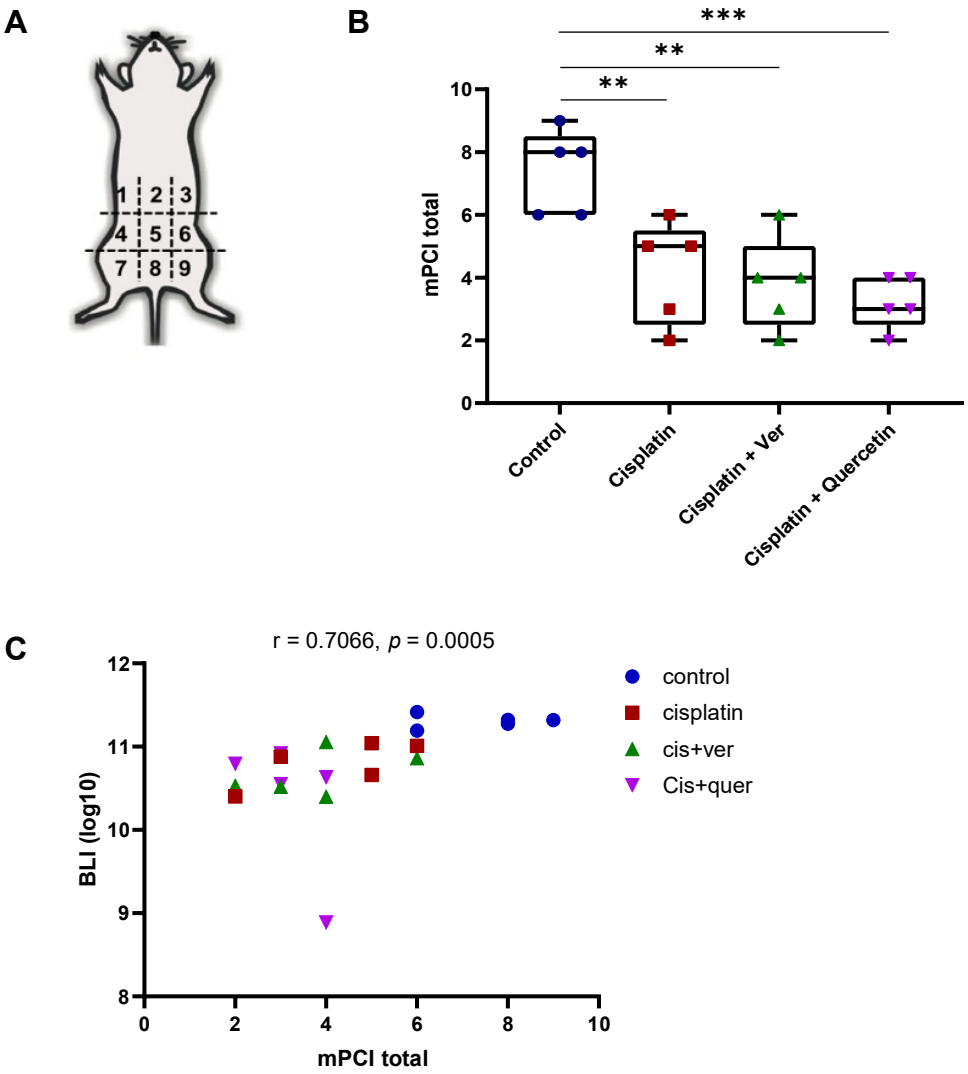

Figure 11 *Modified Peritoneal Cancer Index (mPCI) and its relationship to BLI in the OVCAR8 intraperitoneal xenograft model*

A. Schematic overview of the 9-region mPCI scoring system used to quantify intraperitoneal tumor burden.

B. Box-and-whisker plots of total mPCI scores at necropsy in the four treatment groups (control group, cisplatin, cisplatin + VER-155008, cisplatin + Quercetin; n = 5 per group).

C. Correlation between total mPCI score and terminal BLI signal (log10 total photon flux) across all mice (n = 20). Data points are color-coded by treatment group as indicated; Spearman r = 0.7066, p = 0.0005.

* p < 0.05; ** p < 0.01; *** p < 0.001; **** p < 0.0001.

4.4.3. Disseminated cervical cancer cells in blood and distant organs detected by Alu-qPCR

At necropsy, genomic DNA from peripheral blood, lung and liver was analyzed by human-specific Alu-qPCR to quantify disseminated human tumor cells (tumor cells per 60 ng DNA, log10-transformed for display; Figure 12A–C).

In peripheral blood, the control group showed a median of 19.0 tumor cells/60 ng DNA (range 13.1–35.5), whereas cisplatin-containing regimens yielded lower medians of 3.1 (cisplatin), 9.9 (cisplatin + VER-155008) and 4.4 (cisplatin + Quercetin) tumor cells/60 ng DNA. However, because of variability between mice, Mann–Whitney U tests did not detect statistically significant differences versus the control group.

In lung tissue, tumor cell counts were highest in the control group and consistently lower in all cisplatin-based arms, with median tumor cells/60 ng DNA decreasing from 0.81 in controls to 0.41 in the cisplatin group, 0.47 in the cisplatin + VER-155008 group and 0.32 in the cisplatin + Quercetin group. Mann–Whitney U tests confirmed significantly reduced lung tumor cells for each cisplatin-containing regimen compared with control (control vs cisplatin, $p = 0.0317$; control vs cisplatin + VER-155008, $p = 0.0317$; control vs cisplatin + Quercetin, $p = 0.0079$), while no additional significant differences were observed among the three cisplatin-based groups.

In liver tissue, tumor cells/60 ng DNA again showed marked variability between mice, with median values of 145.9, 3.0, 8.1 and 5.1 tumor cells/60 ng DNA in the control, cisplatin, cisplatin + VER-155008 and cisplatin + Quercetin groups, respectively (corresponding means 60.30, 49.10, 9.66 and 13.69). These differences did not reach statistical significance, but numerically all three cisplatin-containing regimens tended to show lower hepatic tumor cell counts than the control group, with the lowest levels again seen in the cisplatin + VER-155008 and cisplatin + Quercetin arms.

Overall, the Alu-qPCR data support a reduction in disseminated tumor cells under cisplatin-based treatment, most clearly detectable in the lung tissue, while strong inter-individual variability in blood and liver limits conclusions regarding regimen-dependent differences.

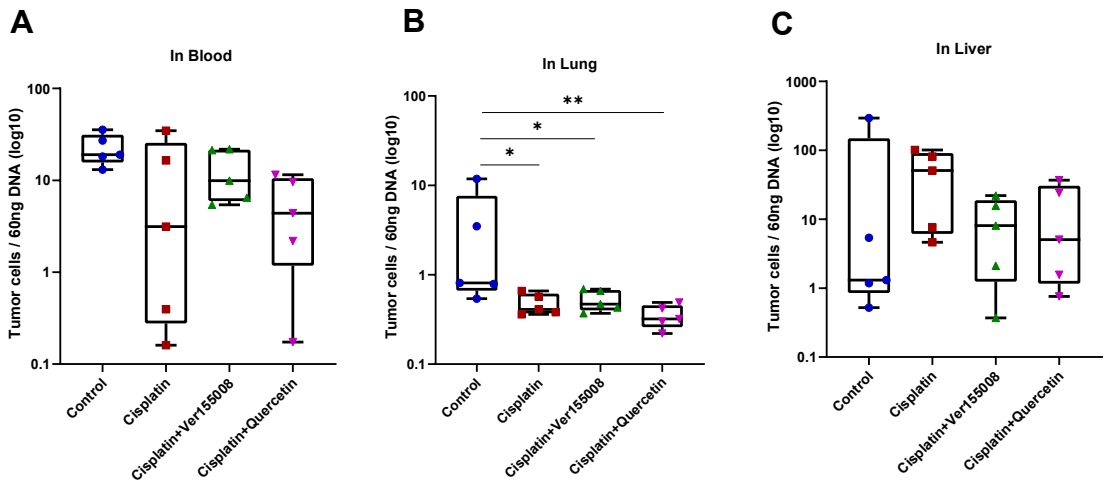

Figure 12 *Detection of disseminated human tumor cells in blood, lung and liver by human-specific Alu-qPCR*

A – C. Human tumor cell equivalents per 60 ng genomic DNA (log10 scale) measured by human-specific Alu-qPCR in peripheral blood (A), lung (B), and liver (C) from the four treatment groups (control group, cisplatin, cisplatin + VER-155008, cisplatin + Quercetin; n = 5 per group).

* $p < 0.05$; ** $p < 0.01$; *** $p < 0.001$; **** $p < 0.0001$.

4.5. Heat-shock induction and immunoblot validation of HSPA6 knockdown in OVCAR8

Given the strong enrichment of HSPA6 in patient-derived spheroids and its marked induction under stress conditions, shRNA-mediated HSPA6 knockdown was established in OVCAR8 cells to enable functional studies. Five lentiviral shRNA constructs targeting HSPA6 (sh#F11, sh#F12, sh#G2, sh#G3 and sh#G4) were generated. Because HSPA6 is only weakly expressed under basal conditions and is predominantly induced after cellular stress, heat shock was applied as a stimulus to induce HSPA6 expression and to assess knockdown efficiency by immunoblot.

sh#G2 was excluded beforehand due to insufficient post-transduction cell numbers. Following heat shock (42 °C, 2 h), HSPA6 was robustly induced in the non-targeting control (NC), whereas normothermic lanes showed little to no signal (Figure 13A). Densitometry (β-actin–normalized; scaled to NC under heat shock = 100%) demonstrated reduced HSPA6 expression in all four knockdown pools, with mean relative levels of 36.15% (sh#F11), 2.535% (sh#F12), 24.13% (sh#G3), and 36.91% (sh#G4). By Dunnett's multiple comparisons test versus NC, reductions were significant for sh#F12 ($p = 0.0101$; 97.5% knockdown) and sh#G3 ($p = 0.0281$; 76.9% knockdown), whereas sh#F11 ($p = 0.0536$) and sh#G4 ($p = 0.0559$) showed the same direction of effect but did not reach statistical significance at the current sample size (Figure 13B). Together, these data confirm heat-inducible HSPA6 expression in OVCAR8 and verify effective knockdown—most pronounced for sh#F12 and sh#G3.

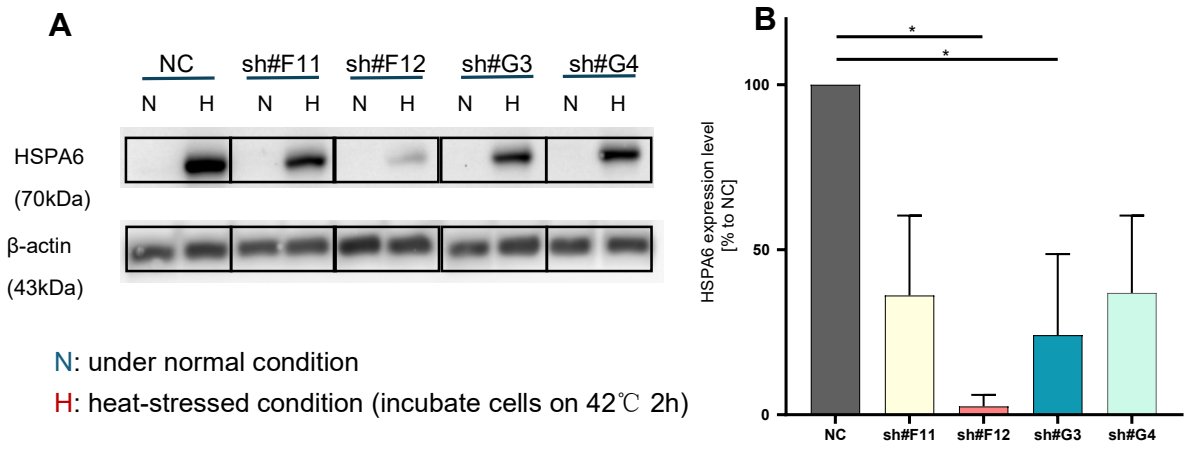

Figure 13 *Heat-shock induction and validation of HSPA6 knockdown in OVCAR8 cells*

A. Immunoblot of HSPA6 (70 kDa) and β-actin (43 kDa) in non-targeting control (NC) and four HSPA6 shRNA pools (sh#F11, sh#F12, sh#G3, sh#G4) under normal conditions (N) and heat-stressed conditions (H; incubation at 42 °C for 2 h).

B. Quantification of HSPA6 protein under heat stress. Band intensities were normalized to β-actin and expressed relative to NC (= 100%). Bars represent mean ± SD.

* $p < 0.05$; ** $p < 0.01$; *** $p < 0.001$; **** $p < 0.0001$.

4.6. Effect of HSPA6 knockdown on cisplatin sensitivity in 2D and 3D OVCAR8 cultures

To test whether HSPA6 knockdown alters cisplatin response in adherent culture, OVCAR8 NC, sh#F12, and sh#G3 sublines were treated 3 μM cisplatin for 72 h (once daily × 3), and cell viability values were normalized to line-matched untreated controls (set to 100%) (Figure 14A). Under cisplatin, mean (± SD) viabilities were 79.51 ± 11.95% for NC, 54.08 ± 14.73% for sh#F12, and 54.49 ± 6.12% for sh#G3. One-way ANOVA with post hoc pairwise comparisons versus NC showed significantly lower viability for both knockdowns (NC vs sh#F12, mean difference 25.43%, $p < 0.0001$; NC vs sh#G3, 25.02%, $p < 0.0001$). Thus, HSPA6 silencing enhances cisplatin sensitivity in 2D, with both sh#F12 and sh#G3 showing approximately 25% reductions versus NC.

To assess drug response in a non-adherent context, OVCAR8 NC, sh#F12, and sh#G3 spheroids were exposed to 3 µM cisplatin for 72 h (once daily × 3); luminescence was normalized to line-matched untreated controls (set to 100%) (Figure 14B). Under cisplatin, mean (± SD) viabilities were 72.17 ± 8.11% for NC, 59.50 ± 3.32% for sh#F12, and 64.16 ± 2.74% for sh#G3. One-way ANOVA with post hoc pairwise comparisons versus NC indicated significantly lower viability for both knockdowns (NC vs sh#F12, mean difference 12.67%, $p < 0.0001$; NC vs sh#G3, 8.01%, $p = 0.0072$). Thus, HSPA6 silencing also increases cisplatin sensitivity in 3D spheroids, with sh#F12 exhibiting the strongest shift.

Taken together, HSPA6 silencing increased cisplatin sensitivity in both 2D and 3D OVCAR8 cultures, with sh#F12 showing the most pronounced shift, consistent with its strongest knockdown efficiency. Therefore, sh#F12 was selected for *in vivo* validation alongside the NC sub line.

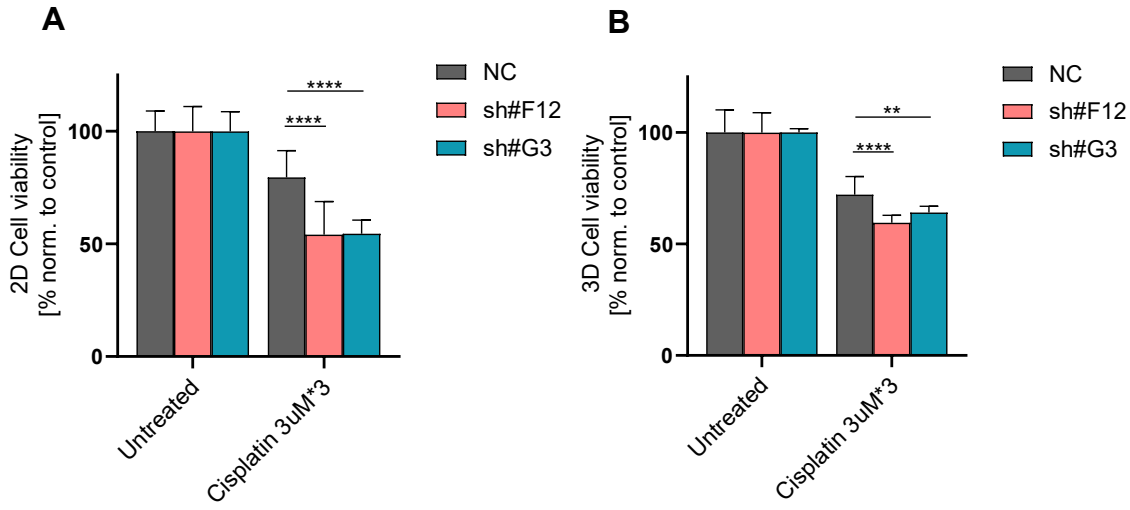

Figure 14 *Effect of HSPA6 knockdown on cisplatin sensitivity in 2D and 3D OVCAR8 cultures*

All cultures were treated with 3 µM cisplatin for 72 h (once daily × 3), and viability was measured at 72 h. Bars show mean ± SD viability of OVCAR8 non-targeting control (NC), sh#F12, and sh#G3, normalized to line-matched untreated controls (100%).

A. 2D adherent cultures.

B. 3D spheroid cultures.

* $p < 0.05$; ** $p < 0.01$; *** $p < 0.001$; **** $p < 0.0001$

4.7. *In vivo* efficacy of HSPA6 silencing in an intraperitoneal ovarian cancer xenograft model

Building on the in vitro data demonstrating that shRNA-mediated HSPA6 knockdown enhances cisplatin sensitivity in OVCAR8 cells, an intraperitoneal OVCAR8 xenograft model was established to assess the in vivo effects of stable HSPA6 silencing on tumour growth and platinum response.

In an intraperitoneal OVCAR8 xenograft model, mice received i.p. injections of either non-targeting control (NC) or HSPA6-knockdown (KD) OVCAR8 cells and were randomized to cisplatin or control treatment in a four-arm design (n = 5 per arm; Figure 15A). Terminal bioluminescence imaging (BLI) was used as the primary endpoint, and the modified peritoneal cancer index (mPCI), total intraperitoneal tumor volume (TTV) and human-specific Alu-qPCR were assessed as secondary endpoints.

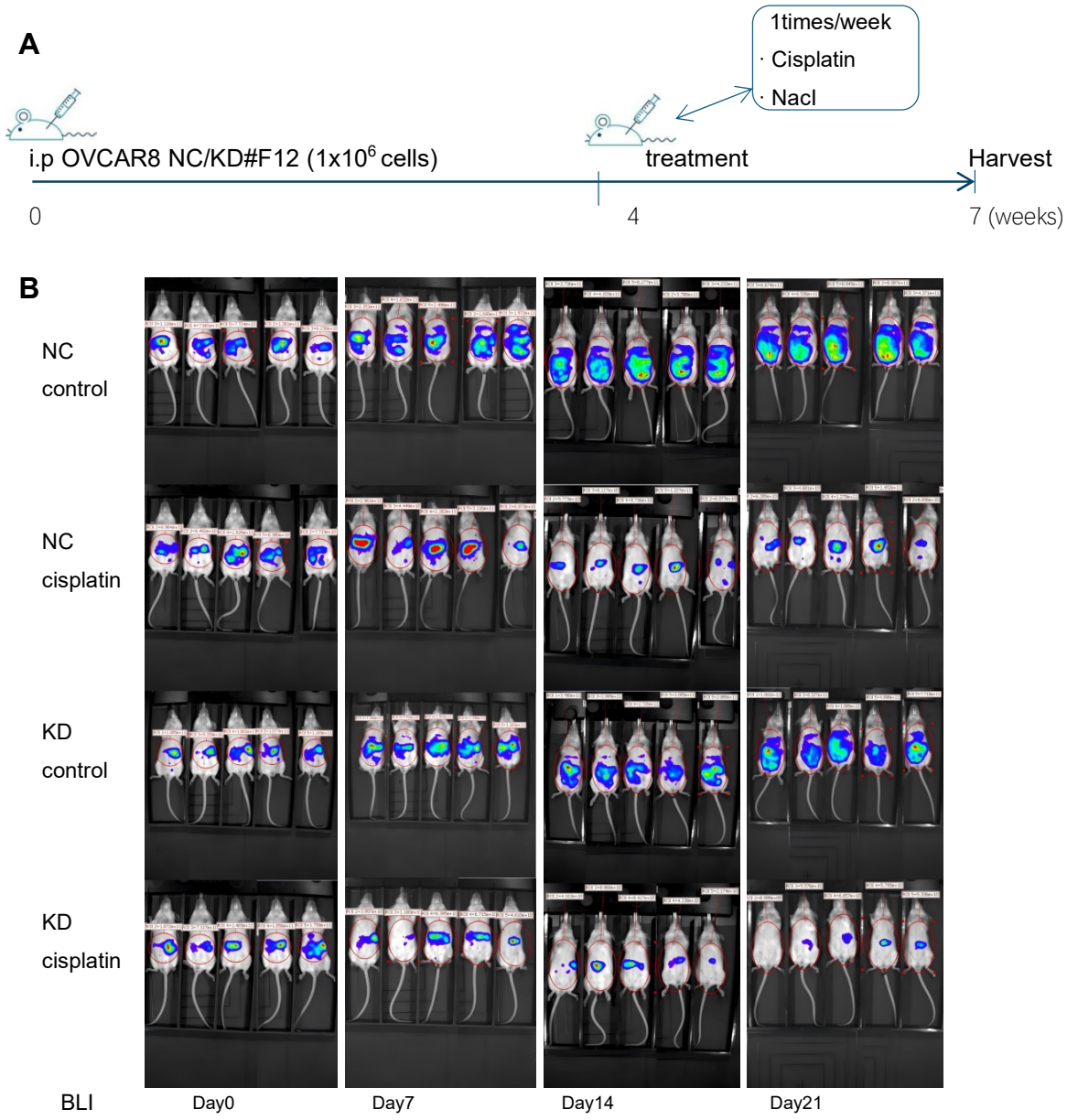
A
1times/week
· Cisplatin
· Nacl
i.p OVCAR8 NC/KD#F12 (1x10^6 cells)
treatment
Harvest
0
4
7 (weeks)
B
NC control
NC cisplatin
KD control
KD cisplatin
BLI
Day0
Day7
Day14
Day21
C
% BLI change from baseline
1500
1000
500
0
****
****
NC control
NC cisplatin
KD control
KD cisplatin
D
NC control
NC cisplatin
KD control
KD cisplatin
% BLI to day 0
1000
500
0
0
7
14
21
days

Figure 15 *In vivo efficacy of HSPA6 silencing in a peritoneal OVCAR8 xenograft model*

A. Timeline of the *in vivo* experiment: intraperitoneal implantation of NC (NC-LUC) or HSPA6-knockdown (KD-LUC) OVCAR8 cells at week 0, baseline BLI and randomization at week 4, followed by 3 weeks of control or cisplatin treatment and terminal analysis at week 7.

B. Representative serial BLI images of NC and KD tumors under control or cisplatin treatment at days 0, 7, 14, and 21.

C. Percentage change in total photon flux from baseline (D21/D0 × 100%) for each group (n = 5), shown as box-and-whisker plots with individual mice.

D. Time course of total photon flux expressed as percentage of day 0 (mean ± SD) over the 21-day observation period.

* $p < 0.05$; ** $p < 0.01$; *** $p < 0.001$; **** $p < 0.0001$.

4.7.1. Bioluminescence-based assessment of tumor burden

At day 21, tumor progression was quantified as the percentage change in total photon flux relative to baseline (D21/D0 × 100%; Figure 15C). In NC tumors, the control group showed a marked increase in BLI signal (mean 780.6% ± 235.5% of baseline), whereas cisplatin limited this to 100.5% ± 41.3%. KD tumors showed a similar pattern, with 694.8% ± 183.9% in the KD control group and 42.8% ± 27.5% in the KD cisplatin group. Two-way ANOVA demonstrated a strong main effect of treatment (cisplatin vs control, $p < 0.0001$), but no significant effect of genotype (NC vs KD, $p = 0.3050$) and no interaction between genotype and treatment ($p = 0.8387$). Post hoc comparisons within each genotype confirmed that cisplatin significantly reduced percent BLI change compared with the corresponding control group in both NC and KD tumors (NC: untreated vs cisplatin, $p < 0.0001$; KD: untreated vs cisplatin, $p < 0.0001$). Within each treatment condition, NC and KD did not differ significantly (control $p = 0.6201$; cisplatin $p = 0.8019$). Nonetheless, the mean percent BLI change was numerically lower in KD than in NC in both the control and cisplatin groups (694.8 vs 780.6% and 42.8 vs 100.5%, respectively), indicating a trend toward weaker tumor outgrowth in KD xenografts that did not reach statistical significance.

Longitudinal bioluminescence (total photon flux normalized to day 0 = 100%) showed clear separation between treatment arms over the 21-day course (n = 5 per group; Figure 15D). In the NC control group, signal rose from 233.8 ± 76.1% (day 7) to 527.8 ± 202.0% (day 14) and 780.6 ± 210.6% (day 21). The KD control group increased more slowly early on (106.2 ± 15.5% at day 7; 257.5 ± 70.5% at day 14) but reached 694.8 ± 164.5% by day 21. In contrast, both cisplatin-treated arms remained near or below baseline: NC cisplatin was 219.2 ± 149.2% (day 7), 92.4 ± 29.2% (day 14), and 100.5 ± 37.0% (day 21); KD cisplatin was 34.2 ± 17.3%, 51.4 ± 40.3%, and 42.8 ± 24.6% at days 7, 14, and 21, respectively. Overall, these time courses illustrate sustained suppression of *in vivo* BLI signal by cisplatin in both NC and KD tumors, with KD controls showing slower early growth than NC controls and KD cisplatin maintaining the lowest trajectory, in line with the percent BLI change from baseline at day 21.

4.7.2. Necropsy-based tumor burden: mPCI and TTV and ascites

At necropsy, peritoneal carcinosis as well as ascites development was documented. We observed a clear decreased in the volume and number of metastatic lesion as well as in the presence of ascites between untreated and treated mice as well as between NC and KD.

Intraperitoneal tumor burden was quantified using the Modified Peritoneal Cancer Index (mPCI) (Figure 16A). Two-way ANOVA revealed significant main effects of treatment (cisplatin vs control; $p = 0.0002$) and genotype (KD vs NC; $p = 0.0234$), but no significant interaction between these factors ($p = 0.8967$). In NC mice, mean (± SD) mPCI decreased from 8.4 ± 2.5 in the control group to 4.8 ± 1.6 with cisplatin, and in KD mice from 6.6 ± 1.5 to 2.8 ± 0.4. Post hoc comparisons confirmed that cisplatin significantly reduced mPCI within both genotypes (NC control vs NC cisplatin, $p = 0.0080$; KD control vs KD cisplatin, $p = 0.0054$). Although comparisons between NC and KD within each treatment arm did not reach statistical significance (control $p = 0.2126$; cisplatin $p = 0.1548$), KD groups consistently exhibited lower mPCI scores than their NC counterparts under both control and cisplatin treatment, with the KD cisplatin group showing the lowest and most uniformly low scores.

Tumor volume was documented and quantified, corresponding TTV per mouse was summed by the way we maintained before in Method and analyzed on a log10 scale (Figure 16B). Here, the enhanced effect of cisplatin on KD tumor became clearer. Two-way ANOVA revealed significant effects of both treatment and genotype, as well as a significant interaction (row factor, cisplatin vs control, $p = 0.0002$; column factor, NC vs KD, $p = 0.0170$; interaction, $p = 0.0488$). In NC mice, mean (± SD) log10 TTV decreased from 2.51 ± 0.18 in the control group to 2.05 ± 0.54 with cisplatin (untreated vs cisplatin, $p = 0.1334$). In KD mice, cisplatin produced a more pronounced reduction, from 2.42 ± 0.27 in the control group to 1.24 ± 0.42 (untreated vs cisplatin, $p =$

0.0003). Comparisons between genotypes showed no difference under control conditions (NC vs KD control, p = 0.9178), whereas under cisplatin the KD group had significantly lower log10 TTV than the NC group (p = 0.0075). Overall, cisplatin reduced TTV in both NC and KD mice, with a significantly stronger effect and the lowest residual tumor burden observed in the KD cisplatin group.

Ascites was additionally assessed at necropsy as an indicator of advanced intraperitoneal disease. Ascites was scored as 0 (absent) or 1 (present)(Figure 16C). In the NC cohort, ascites was present in all control animals but absent in all cisplatin-treated animals (5/5 vs 0/5; Fisher's exact test, p = 0.0079). In KD mice, ascites was observed in 2 out of 5 control animals and in none of the cisplatin-treated animals. These findings are consistent with the mPCI and TTV data and support that cisplatin treatment, particularly in combination with HSPA6 knockdown, reduces intraperitoneal tumour burden and the occurrence of ascites, a clinical sign of advanced disease and poor prognosis in ovarian cancer.

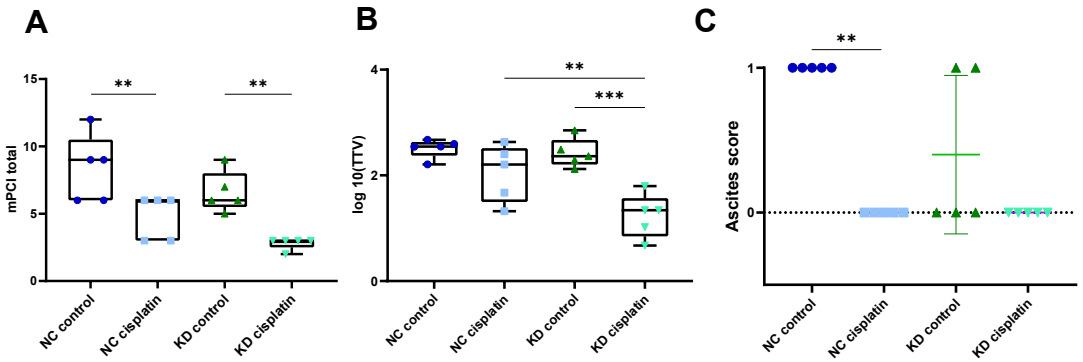

Figure 16 *Necropsy-based assessment of intraperitoneal tumor burden in NC and KD xenografts*

A. Modified Peritoneal Cancer Index (mPCI) total score in NC and KD mice under control or cisplatin treatment (n = 5 per group), shown as box-and-whisker plots with individual values.

B. Total macroscopic intraperitoneal tumor volume (TTV) per mouse, analyzed on a log10 scale, for the same four groups (n = 5 per group), shown as box-and-whisker plots with individual values.

C. Presence of ascites scored as 0 (absent) or 1 (present) in NC control, NC cisplatin, KD control and KD cisplatin groups.

* p < 0.05; ** p < 0.01; *** p < 0.001; **** p < 0.0001.

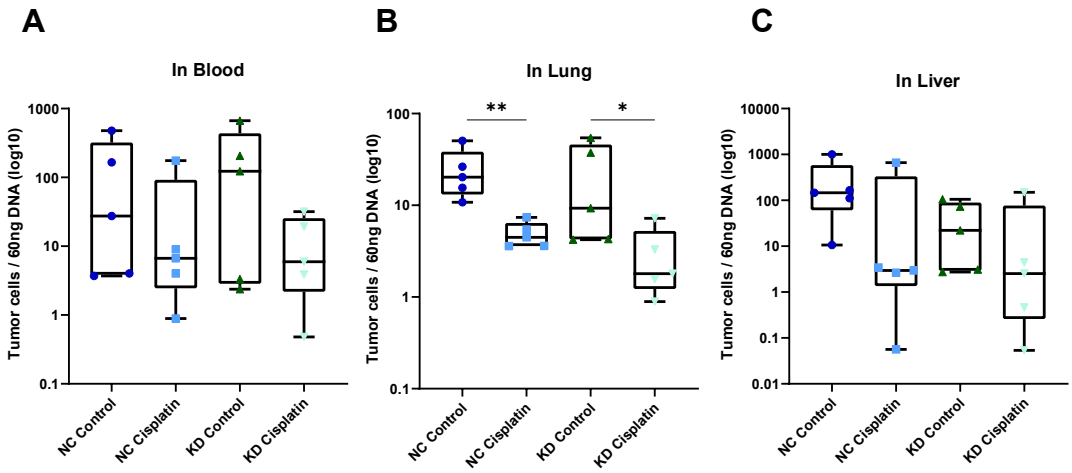

Figure 17 *Detection of disseminated human tumor cells in blood, lung and liver by human-specific Alu-qPCR.*

A – C. Analysis by human-specific Alu-qPCR to quantify disseminated tumor cells (tumor cells/60 ng DNA, log10) in peripheral blood (A), lung (B) and liver (C). Box-and-whisker plots show median, interquartile range, and range, with individual mice (n = 5 per group) for NC control, NC cisplatin, KD control, and KD cisplatin.

* p < 0.05; ** p < 0.01; *** p < 0.001; **** p < 0.0001

4.7.3. Disseminated tumour cells in blood and distant organs detected by Alu-qPCR

At necropsy, genomic DNA from peripheral blood, lung, and liver was analyzed by human-specific Alu-qPCR to quantify disseminated tumor cells (tumor cells per 60 ng DNA, log10-transformed for display; Figure 17A–C).

In peripheral blood, readouts showed substantial inter-individual variability: in the NC cohort, median levels decreased from 27.5 tumor cells/60 ng DNA in the control group to 6.7 with cisplatin, and in the KD cohort from 123.2 to 6.0, but these differences did not reach statistical significance.

In lung tissue, Alu signal was higher in control mice and clearly reduced by cisplatin in both genotypes; median values fell from 20.2 to 4.5 tumor cells/60 ng DNA in NC mice (Mann–Whitney U test, $p = 0.0079$) and from 9.3 to 1.8 in KD mice ($p = 0.0317$). Comparisons between NC and KD within each treatment arm were not significant, although cisplatin-treated groups—particularly KD cisplatin—tended to have lower lung Alu levels than their respective controls.

In liver tissue, Alu-qPCR values were again heterogeneous, with NC medians decreasing from 145.9 to 3.0 tumor cells/60 ng DNA and KD medians from 22.2 to 2.5 under cisplatin, without reaching statistical significance.

Taken together, these data are consistent with a reduction of circulating and disseminated tumor cells under cisplatin treatment, most clearly detectable in lung tissue, while strong variability in blood and liver limits conclusions regarding genotype-dependent effects.

5. Discussion

5.1. Summary of main findings in the context of advanced epithelial ovarian cancer

In this study, we used matched ovarian cancer patient samples, including ascites-derived tumor spheroids and tissues from primary or intraperitoneal metastatic lesions, established ovarian cancer cell lines and intraperitoneal xenograft models to examine the role of stress-inducible HSP70 isoforms, with a special focus on HSPA6, in the response to cisplatin in epithelial ovarian cancer (EOC). Building on our previous transcriptomic profiling of ascites-derived spheroids versus tumor tissues from primary and metastatic sites, which had identified HSP70 family genes among the transcripts upregulated in spheroids (Ding et al., 2021), we now demonstrate that HSP70 enrichment in spheroids is also present at the protein level. HSP70 proteins, particularly HSPA6, were increased in ascites-derived spheroids compared with matched solid tumor tissues or tumoroid samples, and HSPA6 expression was also higher in patient-derived spheroids than in established ovarian cancer cell lines. Pharmacological inhibition of HSP70 reduced cell viability and increased cisplatin sensitivity in both 2D and 3D models, and genetic knockdown of HSPA6 further increased cisplatin sensitivity *in vitro*. In an intraperitoneal xenograft model that mimics peritoneal dissemination of EOC, HSPA6 knockdown in tumor cells was associated with lower total tumor volume and reduced peritoneal tumor burden in cisplatin-treated mice compared with control xenografts receiving the same chemotherapy. Taken together, these findings identify HSPA6 as a stress-inducible HSP70 isoform that is enriched in ascites-derived spheroids and may support the survival of cisplatin-exposed tumor cells in EOC with peritoneal dissemination, a setting in which HSPA6 has so far been examined only to a limited extent.

Advanced epithelial ovarian cancer is characterised by widespread peritoneal

dissemination and malignant ascites, both of which are closely linked to treatment failure and poor survival (Nunes and Ricardo, 2022, Ford et al., 2020). In ascites, tumor cells occur as single cells and, more frequently, as multicellular spheroids that use the peritoneal fluid to disseminate and implant on peritoneal surfaces throughout the abdominal cavity, thereby acting as metastatic units that drive intraperitoneal progression and clinical relapse (Ding et al., 2021, Al Habyan et al., 2018, Uno et al., 2022, Rakina et al., 2022). Recent works have suggested that malignant ascites is not a passive by-product of tumor growth but a dynamic ecosystem composed of tumor cells, mesothelial cells, fibroblasts, immune cells and acellular components such as cytokines, extracellular matrix proteins and extracellular vesicles, all of which together support intraperitoneal spread, immune evasion and drug resistance (Ford et al., 2020, Dogra et al., 2025). Consistent with this view, ascites-derived spheroids display distinct molecular features compared with solid lesions, including increased reliance on mitochondrial oxidative phosphorylation, epithelial–mesenchymal plasticity and specific adhesion and invasion programs that enhance their tumorigenicity and allow them to recreate patient-like dissemination patterns in *in vivo* models (Ding et al., 2021, Wu et al., 2022, Cui et al., 2024). However, whereas adhesion molecules, epithelial–mesenchymal plasticity and metabolic rewiring in ascites-derived spheroids have been studied in some detail, the contribution of stress-response pathways, in particular stress-inducible HSP70 isoforms, to the survival of these metastatic units under chemotherapy-induced stress has remained largely unexplored and is addressed in this work.

5.2. Stress-inducible HSP70 isoforms in ovarian cancer

Beyond the specific role of ascites-derived spheroids, our findings could be placed in the broader context of heat shock protein biology in cancer. Members of the HSP70 family are among the most frequently overexpressed molecular chaperones in human tumors and support several hallmarks of cancer, including sustained proliferation, resistance to apoptosis, invasion and metastasis, and resistance to chemo- and radiotherapy (Murphy, 2013, Zhao et al., 2023). Several reviews have shown that HSP70 proteins interact with many oncogenic signalling pathways and that high HSP70 expression is often associated with poor prognosis and therapy failure across a wide range of solid and haematological malignancies (Murphy, 2013, Zhao et al., 2023). In ovarian cancer, several reviews and primary studies have reported overexpression of HSP70 and other heat shock proteins and have discussed their potential as biomarkers and therapeutic targets (Hoter and Naim, 2019, Cohen et al., 2010). Most of these studies have focused on the major inducible cytosolic isoforms HSPA1A and HSPA1B (also referred to collectively as HSP70-1). In gene expression analyses, HSPA1A is overexpressed in more aggressive epithelial ovarian cancers, particularly high-grade serous tumors, and higher HSPA1A levels are associated with shorter time to progression and overall survival (Oliveira et al., 2021, Guan et al., 2021). Proteomic and secretome studies further showed that HSPA1A is abundantly expressed and secreted by ovarian cancer cells, that its secretion varies with tumor type and stage, and that elevated HSPA1A in ascites-derived extracellular vesicles is linked to unfavourable relapse-free survival (Nowak et al., 2017, Finkernagel et al., 2019). Overall, these studies support a pro-survival role of stress-inducible HSP70 isoforms in ovarian cancer and their involvement in drug resistance, in line with the sensitising effects of HSP70 inhibition and HSPA6 knockdown waht we observed in our models.However, in the RNA-seq cohort from our project, baseline HSPA1A, HSPA1B and HSPA6 mRNA levels in bulk primary

debulking specimens showed no association with FIGO stage, nodal status, residual tumour or overall survival, and only higher HSPA1A expression correlated weakly but significantly with longer disease-free survival. This apparent discrepancy is likely to reflect differences in material and readouts—most clinical reports have assessed total HSP70 protein in small, clinically selected cohorts and have reported associations with platinum resistance or adverse outcome (Li et al., 2021, Hoter and Naim, 2019)—whereas our data are based on mRNA from heterogeneous bulk tumour samples—as well as the dynamic, stress-inducible nature of HSP70 expression (Yun et al., 2019) and the dilution of spheroid- or niche-restricted HSP70-high subpopulations in bulk RNA-seq, particularly in ascites-related 3D models enriched for chemoresistant metastatic units (Uno et al., 2022, Al Habyan et al., 2018) and in bulk datasets where stromal and immune signals can dominate gene-expression signatures (Guo et al., 2023)

Compared with the canonical cytosolic isoforms HSPA1A/HSPA1B, the stress-inducible isoform HSPA6 has been much less studied. A recent review summarised that HSPA6 is almost absent under basal conditions in most tissues, is strongly induced by severe cellular stress, and remains incompletely characterised with respect to its roles in cancer and other diseases (Song et al., 2022a). Available tumor-specific studies suggest that the impact of HSPA6 is highly context dependent. In gliomas, high HSPA6 expression is associated with higher grade, an immunosuppressive microenvironment and worse patient survival, and functional experiments have showed that HSPA6 promotes proliferation, invasion and resistance to apoptosis (Zhou et al., 2022). In gastric cancer, HSPA6 has been proposed as a prognostic and potential therapeutic biomarker; it is upregulated in tumor tissue, associated with Ming classification and larger tumor size, and promotes gastric cancer cell proliferation through the Hippo pathway (Zhang et al., 2023). By contrast, in

breast cancer, the TRIM35–HSPA6 axis has been shown to suppress tumor growth and invasion and to promote apoptosis, suggesting a tumor-suppressive role of HSPA6 in that setting (Jing et al., 2025). In acute myeloid leukaemia, HSPA6 was included in an immunogenic cell death–related gene signature in which higher expression correlated with adverse prognosis (Min et al., 2025). Taken together, these seemingly divergent observations indicate that HSPA6 does not have a uniform function across tumor types but acts within tissue- and context-specific regulatory networks and microenvironments. Our data add a further clinically relevant example by showing that in epithelial ovarian cancer with peritoneal dissemination, HSPA6 is enriched in ascites-derived spheroids and may support the survival of tumor cells exposed to cisplatin.

5.3. Enrichment of stress-inducible HSP70 in ascites-derived spheroids

In patient-derived material, one of our main observations was that stress-inducible HSP70 proteins, in particular HSPA6, were consistently higher in ascites-derived spheroids than in matched tumor tissues and tumoroids. Patient-derived spheroids also expressed higher levels of HSPA6 than established EOC cell lines. This pattern suggests that HSPA6 expression is linked to the ascites niche rather than simply reflecting cell line–intrinsic properties. It is also in line with previous work showing that ascites-derived spheroids from high-grade serous EOC behave as highly tumorigenic metastatic units with a distinct transcriptional profile. These spheroids are characterised by increased mitochondrial oxidative phosphorylation, stem-like features and specific adhesion and invasion programs, and they are able to recreate the peritoneal dissemination pattern of the corresponding patients *in vivo* (Ding et al., 2021, Wu et al., 2022, Cui et al., 2024). In this context, HSPA6 enrichment may form part of a broader adaptive program that helps ascites-derived cells tolerate metabolic stress, shear stress, hypoxia and repeated exposure to cytotoxic drugs.

More broadly, work on three-dimensional (3D) ovarian cancer models has demonstrated that spheroid and organoid cultures more closely resemble patient tumors than 2D monolayers (Yee et al., 2022, Flörkemeier et al., 2024, Fontoura et al., 2020). They display distinct gene expression and metabolic states and tend to be more resistant to cytotoxic drugs. In particular, 3D cultures better preserve cell–cell and cell–matrix interactions, gradients of oxygen and nutrients and stress-response signaling, features that are largely lost in 2D cultures. Recent 3D-bioprinted models have reported that increased extracellular matrix stiffness can further enhance chemoresistance in ovarian cancer cells (Shan et al., 2024). Mechanobiology studies in different tumor types also suggest that mechanical forces and matrix stiffness can drive therapy resistance by activating adaptive signalling pathways and altering drug

uptake (Kalli et al., 2023). Against this background, the robust enrichment of HSPA6 in ascites-derived spheroids raises the possibility that chaperone-mediated stress protection is an integral part of this adaptive program. It may help these metastatic units tolerate the combined metabolic, mechanical and treatment-related stress in the ascites microenvironment and to endure platinum-based chemotherapy.

5.4. Pharmacological HSP70 inhibition and cisplatin response

To examine whether HSP70 activity contributes to platinum tolerance, we used two small-molecule HSP70 inhibitors, VER-155008 and Quercetin. We first focused on VER-155008, an ATP-competitive inhibitor of HSP70/Hsc70 that binds to the nucleotide-binding domain and blocks HSP70 ATPase activity. In several cancer types, including prostate cancer, breast cancer, malignant pleural mesothelioma and anaplastic thyroid carcinoma, VER-155008 has been reported to decrease tumor cell viability, induce apoptosis or paraptosis and interfere with chaperone networks (Brünnert et al., 2020, Kim et al., 2014, Sakai et al., 2021, Budina-Kolomets et al., 2014). In our study, VER-155008 alone had variable and mostly modest effects on the viability of the ovarian cancer cell lines OVCAR8 and SKOV3 cultured as 2D monolayers or 3D spheroids, and on patient-derived spheroids. By contrast, combining VER-155008 with cisplatin generally sensitised cells to cisplatin, with higher cytotoxicity than cisplatin alone in most *in vitro* models, although the strength of this effect differed between individual cell lines and patient samples.

Quercetin was chosen as a second, chemically distinct HSP70 inhibitor. In our experiments, Quercetin alone showed only limited, model-dependent effects on viability in both OVCAR8 and SKOV3 cell lines and in patient-derived spheroids. When combined with cisplatin, Quercetin often led to a further

decrease in cell viability compared with cisplatin alone in 2D and 3D cultures of both cell lines and in patient-derived spheroids, although the effect size varied between models. These observations are consistent with previous work showing that Quercetin can downregulate heat shock proteins, including HSP70, in ovarian cancer cells and can increase their sensitivity to cisplatin or paclitaxel *in vitro* (Maciejczyk and Surowiak, 2013, Shafabakhsh and Asemi, 2019, Rashidi et al., 2021). Several reviews have also noted that Quercetin has pro-apoptotic and anti-proliferative effects in ovarian cancer models and may act as a chemosensitiser when combined with standard drugs (Shafabakhsh and Asemi, 2019, Rashidi et al., 2021, Parvaresh et al., 2016). However, Quercetin is a pleiotropic natural compound that targets multiple pathways, and its effects can depend on dose, schedule and cellular context. In some settings, low concentrations of Quercetin can reduce oxidative stress and partially protect cells, which may help to explain why the chemosensitising effect was not uniform across all our models (Maciejczyk and Surowiak, 2013, Shafabakhsh and Asemi, 2019, Rashidi et al., 2021, Parvaresh et al., 2016).

In our initial intraperitoneal xenograft experiment, we combined cisplatin with either VER-155008 or Quercetin in an OVCAR8-based model. In this *in vivo* experiment, cisplatin clearly reduced tumor burden compared with the control group. Adding VER-155008 or Quercetin to cisplatin trended to the lower BLI signals and mPCI scores in some arms, but these differences did not reach statistical significance. In addition to imaging and macroscopic assessment, we also performed human-specific Alu-qPCR. Tumor cells/60 ng DNA in peripheral blood and lung were highest in the control group and lower in all cisplatin-containing regimens, and we did not observe consistent further reductions in the combination groups.

This modest additional effect of adding VER-155008 or Quercetin on both macroscopic tumor burden and disseminated tumor cells is in line with preclinical and early translational experience with HSP70 inhibitors. Many

HSP70 inhibitors lack clear selectivity within the HSP70 family, show suboptimal pharmacokinetics and have relatively narrow therapeutic windows, and they can induce compensatory stress responses in tumor and normal tissues (Goloudina et al., 2012, Mouawad et al., 2023). Experimental studies have also indicated that cancer cells can adapt to HSP70 blockade by upregulating other chaperones or activating autophagy, which may reduce the overall antitumor impact (Mikhailova et al., 2025, Li et al., 2009, Sannino et al., 2018). In addition, our xenograft experiment used relatively small groups in an aggressive intraperitoneal ovarian cancer model, which makes it difficult to detect moderate combination effects. Overall, our data support a role for HSP70 family activity in modulating the cisplatin response. They show that HSP70 inhibition can enhance cisplatin efficacy *in vitro* in OVCAR8 and SKOV3 cells grown as 2D monolayers and 3D spheroids, as well as in patient-derived spheroids, while also suggesting that more selective and clinically suitable HSP70-targeting strategies will be required to translate this approach successfully *in vivo*.

5.5. Genetic HSPA6 knockdown and cisplatin response

Because the pharmacologic HSP70 inhibition used in our study is neither HSP70-specific nor isoform-selective, we next turned to a genetic approach. Given that HSPA6 showed the strongest enrichment in ascites-derived spheroids and the most robust induction under stress conditions in our models, we targeted HSPA6 directly using lentiviral shRNA in OVCAR8 cells.

In our genetic experiments, we targeted HSPA6 directly using lentiviral shRNA in OVCAR8 cells. Heat-shock immunoblotting confirmed that several shRNA sequences reduced HSPA6 protein, with sh#F12 and sh#G3 showing the most pronounced knockdown under stress conditions. When we exposed these

lines to cisplatin, both HSPA6-knockdown sublines F12 and G3 displayed lower viability than the non-targeting control in 2D monolayers and in 3D spheroids, indicating increased cisplatin sensitivity across culture formats. Among them, sh#F12 showed the strongest change in both knockdown efficiency and drug response and was therefore selected for *in vivo* validation. Overall, these results support a direct contribution of HSPA6 to the cisplatin response in OVCAR8 cells.

In the intraperitoneal OVCAR8 xenograft model, we then compared non-targeting control shRNA xenografts (NC-LUC) with HSPA6-knockdown xenografts (KD-LUC, derived from sh#F12) under control or cisplatin treatment. Terminal BLI and longitudinal imaging showed a clear treatment effect of cisplatin. Cisplatin suppressed tumor growth in both NC and KD tumors, while the main effect of HSPA6 knockdown status (NC versus KD) did not reach statistical significance for the BLI-based endpoints. However, KD xenografts tended to grow more slowly and showed lower BLI signals than NC in both control and cisplatin groups, with the lowest trajectory in the KD cisplatin arm. At necropsy, macroscopic endpoints provided more detailed information. The modified Peritoneal Cancer Index (mPCI), providing a semi-quantitative assessment of intraperitoneal tumour distribution as described in the Methods, was reduced by cisplatin in both shRNA groups (NC and KD) and were also lower overall in KD than in NC, although pairwise NC–KD comparisons did not reach significance within each treatment arm. Total tumor volume showed the clearest interaction between cisplatin treatment and HSPA6 knockdown status: cisplatin decreased tumor volume in both NC and KD mice, but the reduction was significantly stronger in KD xenografts, which had the lowest residual tumor burden under cisplatin.

Human specific Alu-qPCR provided an additional readout for circulating and disseminated tumor cells. We used human-specific Alu-qPCR to estimate the amount of tumor cells (expressed as tumor cells per 60 ng DNA) in blood and

organs. Cisplatin reduced tumor cells per 60 ng DNA in both NC and KD cohorts, most clearly in the lung, where all cisplatin-treated groups showed significantly lower values than untreated controls. Differences between NC and KD groups in blood and liver were more variable and did not reach significance, but KD cisplatin mice often had some of the lowest tumor cell counts in several tissues.

Taken together, these *in vivo* data indicate that cisplatin remains highly effective in this aggressive model and that HSPA6 knockdown may further decrease macroscopic intraperitoneal tumor burden and could help to limit disseminated disease under platinum treatment. Combined with our in vitro data in OVCAR8 cells and in patient-derived spheroids, these findings suggest that HSPA6 expressed in tumor cells contributes to stress adaptation under cisplatin and supports their survival. As tumor cells form the central cellular component of ascites-derived spheroids, this mechanism is likely to be relevant for the behaviour of peritoneal metastatic units in the ascites compartment.

5.6 Overall implications and future directions

Taken together, our data support a role of stress-inducible HSP70, and in particular HSPA6, in modulating the response to platinum in preclinical models that capture key features of advanced EOC. We analysed matched patient samples of ascites-derived spheroids and tumor tissues, 2D monolayers and 3D spheroids from the ovarian cancer cell lines OVCAR8 and SKOV3, patient-derived spheroids *in vitro*, and an intraperitoneal OVCAR8 xenograft model. Across these systems, we found that HSPA6 is enriched in ascites-derived spheroids compared with corresponding solid lesions, that it is more strongly expressed in patient-derived spheroids than in cell lines, and that pharmacological HSP70 inhibition or genetic HSPA6 knockdown can

increase cisplatin sensitivity in both 2D and 3D culture conditions. In the intraperitoneal xenograft model, HSPA6 knockdown further reduced intraperitoneal total tumor volume and disseminated tumor cell numbers under cisplatin treatment, consistent with a contribution of HSPA6 to tumor-cell survival under platinum-induced stress in the intraperitoneal space. These findings can be viewed in the context of two related lines of evidence. First, malignant ascites is now recognised as an active metastatic niche rather than a passive by-product of tumor growth. It contains tumor cells and multiple stromal and immune populations embedded in a complex acellular milieu, and promotes intraperitoneal dissemination, immune escape, metabolic rewiring and resistance to chemotherapy in advanced ovarian cancer. These reviews further note that ascites-derived spheroids can act as metastatic units that seed the peritoneal cavity, and that the cellular and acellular components of ascites provide survival signals that allow tumor cells to tolerate hostile conditions and repeated lines of systemic treatment (Rickard et al., 2021, Ahmed and Stenvers, 2013). Second, stress-inducible heat shock proteins, in particular members of the HSP70 family, are frequently overexpressed in ovarian cancer, interact with oncogenic signalling pathways and DNA-damage responses, and have been associated with platinum resistance, more aggressive disease and poor outcome (Li et al., 2021, van Zyl et al., 2018). Our data extend these concepts by identifying HSPA6 as a stress-inducible HSP70 isoform that is preferentially enriched in ascites-related models and may contributes to platinum tolerance of ovarian cancer cells, supporting a possible link between ascites-associated metastatic units and chaperone-mediated stress adaptation in intraperitoneal disease. From a translational perspective, our findings motivate evaluation of HSPA6 in larger, clinically annotated patient cohorts, with particular attention to intraperitoneal dissemination patterns, ascites characteristics and response to platinum-based chemotherapy, and to integrate HSPA6 into functional studies across additional histological subtypes and orthotopic or intraperitoneal

models (van Zyl et al., 2018, Ahmed and Stenvers, 2013, Richardson et al., 2023). In parallel, our pharmacological data, together with recent work on HSP70-directed small molecules, suggest that more selective and clinically suitable HSP70/HSPA6-targeted approaches and well-designed combinations with platinum-based chemotherapy should be explored to translate chaperone-directed stress modulation into meaningful clinical benefit for patients with advanced EOC (Ambrose and Chapman, 2021, Nitzsche et al., 2023).

6. Zusammenfassung

Aufbauend auf RNA-Seq-Daten, die eine Anreicherung von stressinduzierbaren HSP70-Isoformen in aus Aszites gewonnenen Sphäroiden zeigten, fanden wir, dass die mRNA- und Proteinspiegel von HSP70 in patienteneigenen Sphäroiden höher waren als in den entsprechenden Tumorgeweben und Eierstockkrebszelllinien. Die pharmakologische Hemmung von HSP70 erhöhte die Cisplatin-induzierte Zytotoxizität *in vitro*, und in einem Xenograft-Modell reduzierten Cisplatin-haltige Therapien die intraperitoneale Tumorlast und die Ausbreitung von Tumorzellen. Parallel dazu sensibilisierte die shRNA-vermittelte Hemmung von HSPA6 die Zellen gegenüber Cisplatin und verringerte das intraperitoneale Tumorvolumen und die Ausbreitung. Zusammengenommen deuten diese Ergebnisse darauf hin, dass stressinduzierbares HSP70 zur Platintoleranz in der Aszitesnische beiträgt und ein potenzielles Ziel zur Verbesserung der Cisplatin-Wirksamkeit bei fortgeschrittenem Eierstockkrebs darstellen könnte, wobei sich HSPA6 als besonders relevante Isoform herausstellt.

Summary (English version)

Building on RNA-seq data indicating enrichment of stress-inducible HSP70 isoforms in ascites-derived spheroids, we found that HSP70 mRNA and protein levels were higher in patient-derived spheroids than in both matched tumor tissues and EOC cell lines. Pharmacological inhibition of HSP70 increased cisplatin-induced cytotoxicity *in vitro* and, in a xenograft model, cisplatin-containing regimens reduced intraperitoneal tumor burden and disseminated tumor cells. In parallel, shRNA-mediated silencing of HSPA6 sensitised cells to cisplatin and lowered intraperitoneal tumor volume and dissemination. Taken together, these findings suggest that stress-inducible HSP70 contributes to platinum tolerance in the ascites niche and may represent a potential target to improve cisplatin efficacy in advanced EOC, with HSPA6 emerging as a particularly relevant isoform.

7. References

AABO, K., ADAMS, M., ADNITT, P., ALBERTS, D. S., ATHANAZZIOU, A., BARLEY, V., BELL, D. R., BIANCHI, U., BOLIS, G., BRADY, M. F., BRODOVSKY, H. S., BRUCKNER, H., BUYSE, M., CANETTA, R., CHYLAK, V., COHEN, C. J., COLOMBO, N., CONTE, P. F., CROWTHER, D., EDMONSON, J. H., GENNATAS, C., GILBEY, E., GORE, M., GUTHRIE, D., YEAP, B. Y. & ET AL. 1998. Chemotherapy in advanced ovarian cancer: four systematic meta-analyses of individual patient data from 37 randomized trials. Advanced Ovarian Cancer Trialists' Group. *Br J Cancer,* 78**,** 1479–87.

AHMED, N. & STENVERS, K. L. 2013. Getting to know ovarian cancer ascites: opportunities for targeted therapy-based translational research. *Front Oncol,* 3**,** 256.

AL HABYAN, S., KALOS, C., SZYMBORSKI, J. & MCCAFFREY, L. 2018. Multicellular detachment generates metastatic spheroids during intra-abdominal dissemination in epithelial ovarian cancer. *Oncogene,* 37**,** 5127–5135.

ALEMZADEH, E., ALLAHQOLI, L., MAZIDIMORADI, A., ALEMZADEH, E., GHASEMI, F., SALEHINIYA, H. & ALKATOUT, I. 2024. Deciphering resistance mechanisms and novel strategies to overcome drug resistance in ovarian cancer: a comprehensive review. *Oncol Res,* 32**,** 831–847.

AMBROSE, A. J. & CHAPMAN, E. 2021. Function, Therapeutic Potential, and Inhibition of Hsp70 Chaperones. *J Med Chem,* 64**,** 7060–7082.

ANDERSON, N. M. & SIMON, M. C. 2020. The tumor microenvironment. *Curr Biol,* 30**,** R921–r925.

ARMSTRONG, D. K. 2013. New issues in systemic therapy for ovarian cancer. *J Natl Compr Canc Netw,* 11**,** 690–3.

BALABURSKI, G. M., LEU, J. I., BEEHARRY, N., HAYIK, S., ANDRAKE, M. D., ZHANG, G., HERLYN, M., VILLANUEVA, J., DUNBRACK, R. L., JR., YEN, T., GEORGE, D. L. & MURPHY, M. E. 2013. A modified HSP70 inhibitor shows broad activity as an anticancer agent. *Mol Cancer Res,* 11**,** 219–29.

BASTIAENEN, V. P., KLAVER, C. E. L., VAN DER HEIJDEN, M. C. S., NIJMAN, L. E., LECCA, M. C., TANIS, P. J., LENOS, K. J. & VERMEULEN, L. 2020. A mouse model for peritoneal metastases of colorectal origin recapitulates patient heterogeneity. *Lab Invest,* 100**,** 1465–1474.

BAYRAKTAR, E., CHEN, S., CORVIGNO, S., LIU, J. & SOOD, A. K. 2024. Ovarian cancer metastasis: Looking beyond the surface. *Cancer Cell,* 42**,** 1631–1636.

BLANDER, S. J. & HORWITZ, M. A. 1993. Major cytoplasmic membrane protein of Legionella pneumophila, a genus common antigen and member of the hsp 60 family of heat shock proteins, induces protective immunity in a guinea pig model of Legionnaires' disease. *J Clin Invest,* 91**,** 717–23.

BOU ANTOUN, N. & CHIONI, A. M. 2023. Dysregulated Signalling Pathways Driving Anticancer Drug Resistance. *Int J Mol Sci,* 24.

BOULIKAS, T. & VOUGIOUKA, M. 2004. Recent clinical trials using cisplatin, carboplatin and their combination chemotherapy drugs (review). *Oncol Rep,* 11**,** 559–95.

BOWTELL, D. D., BöHM, S., AHMED, A. A., ASPURIA, P. J., BAST, R. C., JR., BERAL, V., BEREK, J. S., BIRRER, M. J., BLAGDEN, S., BOOKMAN, M. A., BRENTON, J. D., CHIAPPINELLI, K. B.,

MARTINS, F. C., COUKOS, G., DRAPKIN, R., EDMONDSON, R., FOTOPOULOU, C., GABRA, H., GALON, J., GOURLEY, C., HEONG, V., HUNTSMAN, D. G., IWANICKI, M., KARLAN, B. Y., KAYE, A., LENGYEL, E., LEVINE, D. A., LU, K. H., MCNEISH, I. A., MENON, U., NAROD, S. A., NELSON, B. H., NEPHEW, K. P., PHAROAH, P., POWELL, D. J., JR., RAMOS, P., ROMERO, I. L., SCOTT, C. L., SOOD, A. K., STRONACH, E. A. & BALKWILL, F. R. 2015. Rethinking ovarian cancer II: reducing mortality from high-grade serous ovarian cancer. *Nat Rev Cancer,* 15**,** 668–79.

BRüNNERT, D., LANGER, C., ZIMMERMANN, L., BARGOU, R. C., BURCHARDT, M., CHATTERJEE, M. & STOPE, M. B. 2020. The heat shock protein 70 inhibitor VER155008 suppresses the expression of HSP27, HOP and HSP90β and the androgen receptor, induces apoptosis, and attenuates prostate cancer cell growth. *J Cell Biochem,* 121**,** 407–417.

BUDINA-KOLOMETS, A., BALABURSKI, G. M., BONDAR, A., BEEHARRY, N., YEN, T. & MURPHY, M. E. 2014. Comparison of the activity of three different HSP70 inhibitors on apoptosis, cell cycle arrest, autophagy inhibition, and HSP90 inhibition. *Cancer Biol Ther,* 15**,** 194–9.

BUSCH, T. M., XING, X., YU, G., YODH, A., WILEYTO, E. P., WANG, H. W., DURDURAN, T., ZHU, T. C. & WANG, K. K. 2009. Fluence rate-dependent intratumor heterogeneity in physiologic and cytotoxic responses to Photofrin photodynamic therapy. *Photochem Photobiol Sci,* 8**,** 1683–93.

CAI, Q., FAN, Q., BUECHLEIN, A., MILLER, D., NEPHEW, K. P., LIU, S., WAN, J. & XU, Y. 2018. Changes in mRNA/protein expression and signaling pathways in in vivo passaged mouse ovarian cancer cells. *PLoS One,* 13**,** e0197404.

CARNERO, A., BLANCO-APARICIO, C., RENNER, O., LINK, W. & LEAL, J. F. 2008. The PTEN/PI3K/AKT signalling pathway in cancer, therapeutic implications. *Curr Cancer Drug Targets,* 8**,** 187–98.

CARUSO, G., WEROHA, S. J. & CLIBY, W. 2025. Ovarian Cancer: A Review. *Jama,* 334**,** 1278–1291.

COHEN, M., DROMARD, M. & PETIGNAT, P. 2010. Heat shock proteins in ovarian cancer: a potential target for therapy. *Gynecol Oncol,* 119**,** 164–6.

CUI, X., XU, J. & JIA, X. 2024. Targeting mitochondria: a novel approach for treating platinum-resistant ovarian cancer. *J Transl Med,* 22**,** 968.

DASARI, S. & TCHOUNWOU, P. B. 2014. Cisplatin in cancer therapy: molecular mechanisms of action. *Eur J Pharmacol,* 740**,** 364–78.

DE CLERCQ, K., XIE, F., DE WEVER, O., DESCAMPS, B., HOORENS, A., VERMEULEN, A., CEELEN, W. & VERVAET, C. 2019. Preclinical evaluation of local prolonged release of paclitaxel from gelatin microspheres for the prevention of recurrence of peritoneal carcinomatosis in advanced ovarian cancer. *Sci Rep,* 9**,** 14881.

DEJONGHE, W., KUENEN, S., MYLLE, E., VASILEVA, M., KEECH, O., VIOTTI, C., SWERTS, J., FENDRYCH, M., ORTIZ-MOREA, F. A., MISHEV, K., DELANG, S., SCHOLL, S., ZARZA, X., HEILMANN, M., KOURELIS, J., KASPROWICZ, J., NGUYEN LE, S. L., DROZDZECKI, A., VAN HOUTTE, I., SZATMáRI, A. M., MAJDA, M., BAISA, G., BEDNAREK, S. Y., ROBERT, S., AUDENAERT, D., TESTERINK, C., MUNNIK, T., VAN DAMME, D., HEILMANN, I., SCHUMACHER, K., WINNE, J., FRIML, J., VERSTREKEN, P. & RUSSINOVA, E. 2016. Mitochondrial uncouplers inhibit clathrin-mediated endocytosis largely through cytoplasmic acidification. *Nat Commun,* 7**,** 11710.

DHALIWAL, D. & SHEPHERD, T. G. 2022. Molecular and cellular mechanisms controlling

integrin-mediated cell adhesion and tumor progression in ovarian cancer metastasis: a review. *Clin Exp Metastasis,* 39**,** 291–301.

DING, Y., LABITZKY, V., LEGLER, K., QI, M., SCHUMACHER, U., SCHMALFELDT, B., STüRKEN, C. & OLIVEIRA-FERRER, L. 2021. Molecular characteristics and tumorigenicity of ascites-derived tumor cells: mitochondrial oxidative phosphorylation as a novel therapy target in ovarian cancer. *Mol Oncol,* 15**,** 3578–3595.

DOGRA, S., ADHIKARI, L., BENBROOK, D. M., BOHN, J. A., BURGETT, A., CHANDRA, V., DOCKERY, L., SINGH, A., MCNALLY, L., RAI, R., ISINGIZWE, Z. R., RICHARDSON, D. L., YANG, Z. & HANNAFON, B. N. 2025. Harnessing ovarian cancer ascites for translational science: models, biomarkers, and therapeutics. *Mol Cancer,* 24**,** 257.

DU BOIS, A., REUSS, A., PUJADE-LAURAINE, E., HARTER, P., RAY-COQUARD, I. & PFISTERER, J. 2009. Role of surgical outcome as prognostic factor in advanced epithelial ovarian cancer: a combined exploratory analysis of 3 prospectively randomized phase 3 multicenter trials: by the Arbeitsgemeinschaft Gynaekologische Onkologie Studiengruppe Ovarialkarzinom (AGO-OVAR) and the Groupe d'Investigateurs Nationaux Pour les Etudes des Cancers de l'Ovaire (GINECO). *Cancer,* 115**,** 1234–44.

DU, Z. X., ZHANG, H. Y., MENG, X., GAO, Y. Y., ZOU, R. L., LIU, B. Q., GUAN, Y. & WANG, H. Q. 2009. Proteasome inhibitor MG132 induces BAG3 expression through activation of heat shock factor 1. *J Cell Physiol,* 218**,** 631–7.

FINKERNAGEL, F., REINARTZ, S., SCHULDNER, M., MALZ, A., JANSEN, J. M., WAGNER, U., WORZFELD, T., GRAUMANN, J., VON STRANDMANN, E. P. & MüLLER, R. 2019. Dual-platform affinity proteomics identifies links between the recurrence of ovarian carcinoma and proteins released into the tumor microenvironment. *Theranostics,* 9**,** 6601–6617.

FLöRKEMEIER, I., ANTONS, L. K., WEIMER, J. P., HEDEMANN, N., ROGMANS, C., KRüGER, S., SCHERLIEß, R., DEMPFLE, A., ARNOLD, N., MAASS, N. & BAUERSCHLAG, D. O. 2024. Multicellular ovarian cancer spheroids: novel 3D model to mimic tumour complexity. *Sci Rep,* 14**,** 23526.

FONTOURA, J. C., VIEZZER, C., DOS SANTOS, F. G., LIGABUE, R. A., WEINLICH, R., PUGA, R. D., ANTONOW, D., SEVERINO, P. & BONORINO, C. 2020. Comparison of 2D and 3D cell culture models for cell growth, gene expression and drug resistance. *Mater Sci Eng C Mater Biol Appl,* 107**,** 110264.

FORD, C. E., WERNER, B., HACKER, N. F. & WARTON, K. 2020. The untapped potential of ascites in ovarian cancer research and treatment. *Br J Cancer,* 123**,** 9–16.

GAILLARD, S., LACCHETTI, C., ARMSTRONG, D. K., CLIBY, W. A., EDELSON, M. I., GARCIA, A. A., GHEBRE, R. G., GRESSEL, G. M., LESNOCK, J. L., MEYER, L. A., MOORE, K. N., O'CEARBHAILL, R. E., OLAWAIYE, A. B., SALANI, R., SPARACIO, D., VAN DRIEL, W. J. & TEW, W. P. 2025. Neoadjuvant Chemotherapy for Newly Diagnosed, Advanced Ovarian Cancer: ASCO Guideline Update. *J Clin Oncol,* 43**,** 868–891.

GALANSKI, M. S. & KEPPLER, B. K. 2007. Searching for the Magic Bullet: Anticancer Platinum Drugs Which Can Be Accumulated or Activated in the Tumor Tissue. *Anticancer Agents Med Chem,* 7**,** 55–73.

GAPONOVA, A. V., DENEKA, A. Y., BECK, T. N., LIU, H., ANDRIANOV, G., NIKONOVA, A. S., NICOLAS, E., EINARSON, M. B., GOLEMIS, E. A. & SEREBRIISKII, I. G. 2017. Identification of

evolutionarily conserved DNA damage response genes that alter sensitivity to cisplatin. *Oncotarget,* 8**,** 19156–19171.

GASTPAR, R., GEHRMANN, M., BAUSERO, M. A., ASEA, A., GROSS, C., SCHROEDER, J. A. & MULTHOFF, G. 2005. Heat shock protein 70 surface-positive tumor exosomes stimulate migratory and cytolytic activity of natural killer cells. *Cancer Res,* 65**,** 5238–47.

GHOSH, S. 2019. Cisplatin: The first metal based anticancer drug. *Bioorg Chem,* 88**,** 102925.

GOLOUDINA, A. R., DEMIDOV, O. N. & GARRIDO, C. 2012. Inhibition of HSP70: a challenging anti-cancer strategy. *Cancer Lett,* 325**,** 117–24.

GONG, J., ZHU, B., MURSHID, A., ADACHI, H., SONG, B., LEE, A., LIU, C. & CALDERWOOD, S. K. 2009. T cell activation by heat shock protein 70 vaccine requires TLR signaling and scavenger receptor expressed by endothelial cells-1. *J Immunol,* 183**,** 3092–8.

GONZáLEZ-MARTíN, A., SáNCHEZ-LORENZO, L., BRATOS, R., MáRQUEZ, R. & CHIVA, L. 2014. First-line and maintenance therapy for ovarian cancer: current status and future directions. *Drugs,* 74**,** 879–89.

GRáF, A., ENYEDI, M. Z., PINTéR, L., KRISTON-PáL, É., JAKSA, G., BáLIND, Á., EZER, É., HORVáTH, P., SüKöSD, F., KISS, E. & HARACSKA, L. 2021. The Combination of Single-Cell and Next-Generation Sequencing Can Reveal Mosaicism for BRCA2 Mutations and the Fine Molecular Details of Tumorigenesis. *Cancers (Basel),* 13.

GREENE, M. H., BOICE, J. D., JR., GREER, B. E., BLESSING, J. A. & DEMBO, A. J. 1982. Acute nonlymphocytic leukemia after therapy with alkylating agents for ovarian cancer: a study of five randomized clinical trials. *N Engl J Med,* 307**,** 1416–21.

GROSS, C., KOELCH, W., DEMAIO, A., ARISPE, N. & MULTHOFF, G. 2003. Cell surface-bound heat shock protein 70 (Hsp70) mediates perforin-independent apoptosis by specific binding and uptake of granzyme B. *J Biol Chem,* 278**,** 41173–81.

GUAN, Y., ZHU, X., LIANG, J., WEI, M., HUANG, S. & PAN, X. 2021. Upregulation of HSPA1A/HSPA1B/HSPA7 and Downregulation of HSPA9 Were Related to Poor Survival in Colon Cancer. *Front Oncol,* 11**,** 749673.

GUO, S., LIU, X., ZHANG, J., HUANG, Z., YE, P., SHI, J., STALIN, A., WU, C., LU, S., ZHANG, F., GAO, Y., JIN, Z., TAO, X., HUANG, J., ZHAI, Y., SHI, R., GUO, F., ZHOU, W. & WU, J. 2023. Integrated analysis of single-cell RNA-seq and bulk RNA-seq unravels T cell-related prognostic risk model and tumor immune microenvironment modulation in triple-negative breast cancer. *Comput Biol Med,* 161**,** 107066.

HAIDER, M. T., FREYTAG, V., KRAUSE, L., SPETHMANN, T., GOSAU, T., BEINE, M. C., KNIES, C., SCHRöDER-SCHWARZ, J., HORN, M., RIECKEN, K. & LANGE, T. 2024. Comparison of ex vivo bioluminescence imaging, Alu-qPCR and histology for the quantification of spontaneous lung and bone metastases in subcutaneous xenograft mouse models. *Clin Exp Metastasis,* 41**,** 103–115.

HINSHAW, D. C. & SHEVDE, L. A. 2019. The Tumor Microenvironment Innately Modulates Cancer Progression. *Cancer Res,* 79**,** 4557–4566.

HOTER, A. & NAIM, H. Y. 2019. Heat Shock Proteins and Ovarian Cancer: Important Roles and Therapeutic Opportunities. *Cancers (Basel),* 11.

JääTTELä, M., WISSING, D., BAUER, P. A. & LI, G. C. 1992. Major heat shock protein hsp70 protects tumor cells from tumor necrosis factor cytotoxicity. *Embo j,* 11**,** 3507–12.

JEE, B., DHAR, R., SINGH, S. & KARMAKAR, S. 2021. Heat Shock Proteins and Their Role in

Pregnancy: Redefining the Function of "Old Rum in a New Bottle". *Front Cell Dev Biol,* 9**,** 648463.

JING, X., LI, F., ZHOU, J., ZHANG, J., CAO, L., GUO, C., LI, Q., PENG, H., JIANG, Q., WANG, X., CHEN, Y., DING, J., TONG, D., ZHAO, Z. & HUANG, C. 2025. TRIM35, a novel DNA-binding protein, epigenetically modifies H3 to promote HSPA6 transcription and suppress breast cancer progression. *Cell Death Discov,* 11**,** 479.

KAIGORODOVA, E. V. & BOGATYUK, M. V. 2014. Heat shock proteins as prognostic markers of cancer. *Curr Cancer Drug Targets,* 14**,** 713–26.

KALLI, M., POSKUS, M. D., STYLIANOPOULOS, T. & ZERVANTONAKIS, I. K. 2023. Beyond matrix stiffness: targeting force-induced cancer drug resistance. *Trends Cancer,* 9**,** 937–954.

KAMPINGA, H. H. & CRAIG, E. A. 2010. The HSP70 chaperone machinery: J proteins as drivers of functional specificity. *Nat Rev Mol Cell Biol,* 11**,** 579–92.

KHOSRAVI-SHAHI, P. & CABEZON-GUTIERREZ, L. 2012. Antiangiogenic drugs in the treatment of advanced epithelial ovarian cancer. *Anticancer Agents Med Chem,* 12**,** 982–7.

KIM, E., HAN, D. J., KIM, B. H., YOO, J., KIM, H. J., WU, H. G., KIM, K. S., KIM, H. S., HAN, I., MOON, K. C., PARK, J. H., SONG, S., KIM, T. M. & CHANG, J. H. 2023. Whole-Genome Sequencing Reveals Mutational Signatures Related to Radiation-Induced Sarcomas and DNA-Damage-Repair Pathways. *Mod Pathol,* 36**,** 100004.

KIM, J. Y., CHO, C. H. & SONG, H. S. 2017. Targeted therapy of ovarian cancer including immune check point inhibitor. *Korean J Intern Med,* 32**,** 798–804.

KIM, S. H., KANG, J. G., KIM, C. S., IHM, S. H., CHOI, M. G., YOO, H. J. & LEE, S. J. 2014. The hsp70 inhibitor VER155008 induces paraptosis requiring de novo protein synthesis in anaplastic thyroid carcinoma cells. *Biochem Biophys Res Commun,* 454**,** 36–41.

KLYMENKO, Y., KIM, O. & STACK, M. S. 2017. Complex Determinants of Epithelial: Mesenchymal Phenotypic Plasticity in Ovarian Cancer. *Cancers (Basel),* 9.

KONECNY, G. E., WANG, C., HAMIDI, H., WINTERHOFF, B., KALLI, K. R., DERING, J., GINTHER, C., CHEN, H. W., DOWDY, S., CLIBY, W., GOSTOUT, B., PODRATZ, K. C., KEENEY, G., WANG, H. J., HARTMANN, L. C., SLAMON, D. J. & GOODE, E. L. 2014. Prognostic and therapeutic relevance of molecular subtypes in high-grade serous ovarian cancer. *J Natl Cancer Inst,* 106.

KONISHI, I., ABIKO, K., HAYASHI, T., YAMANOI, K., MURAKAMI, R., YAMAGUCHI, K., HAMANISHI, J., BABA, T., MATSUMURA, N. & MANDAI, M. 2022. Peritoneal dissemination of high-grade serous ovarian cancer: pivotal roles of chromosomal instability and epigenetic dynamics. *J Gynecol Oncol,* 33**,** e83.

KRZYSTYNIAK, J., CEPPI, L., DIZON, D. S. & BIRRER, M. J. 2016. Epithelial ovarian cancer: the molecular genetics of epithelial ovarian cancer. *Ann Oncol,* 27 Suppl 1**,** i4–i10.

LANGSETH, H., HANKINSON, S. E., SIEMIATYCKI, J. & WEIDERPASS, E. 2008. Perineal use of talc and risk of ovarian cancer. *J Epidemiol Community Health,* 62**,** 358–60.

LAVOUé, V., THéDREZ, A., LEVêQUE, J., FOUCHER, F., HENNO, S., JAUFFRET, V., BELAUD-ROTUREAU, M. A., CATROS, V. & CABILLIC, F. 2013. Immunity of human epithelial ovarian carcinoma: the paradigm of immune suppression in cancer. *J Transl Med,* 11**,** 147.

LEARY, A., AUGUSTE, A. & MESNAGE, S. 2016. DNA damage response as a therapeutic target in gynecological cancers. *Curr Opin Oncol,* 28**,** 404–11.

LHEUREUX, S., BRAUNSTEIN, M. & OZA, A. M. 2019. Epithelial ovarian cancer: Evolution of management in the era of precision medicine. *CA Cancer J Clin,* 69**,** 280–304.

LI, C., ZHANG, N., ZHOU, J., DING, C., JIN, Y., CUI, X., PU, K. & ZHU, Y. 2018. Peptide Blocking of PD-1/PD-L1 Interaction for Cancer Immunotherapy. *Cancer Immunol Res,* 6**,** 178–188.

LI, F., ZHANG, H., HUANG, Y., LI, D., ZHENG, Z., XIE, K., CAO, C., WANG, Q., ZHAO, X., HUANG, Z., CHEN, S., CHEN, H., FAN, Q., DENG, F., HOU, L., DENG, X. & TAN, W. 2024. Single-cell transcriptome analysis reveals the association between histone lactylation and cisplatin resistance in bladder cancer. *Drug Resist Updat,* 73**,** 101059.

LI, J., XU, X. & PENG, X. 2022. NDC80 Enhances Cisplatin-resistance in Triple-negative Breast Cancer. *Arch Med Res,* 53**,** 378–387.

LI, M., WANG, J., JING, J., HUA, H., LUO, T., XU, L., WANG, R., LIU, D. & JIANG, Y. 2009. Synergistic promotion of breast cancer cells death by targeting molecular chaperone GRP78 and heat shock protein 70. *J Cell Mol Med,* 13**,** 4540–50.

LI, X. F., HUA, T., LI, Y., TIAN, Y. J., HUO, Y. & KANG, S. 2021. The HSP70 gene predicts prognosis and response to chemotherapy in epithelial ovarian cancer. *Ann Transl Med,* 9**,** 806.

LIN, Q., LI, S., JIN, H., CAI, H., ZHU, X., YANG, Y., WU, J., QI, C., SHAO, X., LI, J., ZHANG, K., ZHOU, W., ZHANG, M., CHENG, J., GU, L., MOU, S. & NI, Z. 2023. Mitophagy alleviates cisplatin-induced renal tubular epithelial cell ferroptosis through ROS/HO-1/GPX4 axis. *Int J Biol Sci,* 19**,** 1192–1210.

LIU, D., ZHANG, L., INDIMA, N., PENG, K., LI, Q., HUA, T. & TANG, G. 2017. CT and MRI findings of type I and type II epithelial ovarian cancer. *Eur J Radiol,* 90**,** 225–233.

LIU, J., LIU, C., MA, Y., PAN, X., CHU, R., YAO, S., CHEN, J., LIU, C., CHEN, Z., SHENG, C., ZHANG, K., XUE, Y., SCHIöTH, H. B., KONG, B., ZHANG, Q. & SONG, K. 2024. STING inhibitors sensitize platinum chemotherapy in ovarian cancer by inhibiting the CGAS-STING pathway in cancer-associated fibroblasts (CAFs). *Cancer Lett,* 588**,** 216700.

LIU, T., DANIELS, C. K. & CAO, S. 2012. Comprehensive review on the HSC70 functions, interactions with related molecules and involvement in clinical diseases and therapeutic potential. *Pharmacol Ther,* 136**,** 354–74.

MA, F., YAN, S., ZHANG, J., WANG, Y., WANG, L., WANG, Y., ZHANG, S., DU, X., ZHANG, P., CHEN, H. Y. & HUANG, S. 2021. Nanopore Sequencing Accurately Identifies the Cisplatin Adduct on DNA. *ACS Sens,* 6**,** 3082–3092.

MACIEJCZYK, A. & SUROWIAK, P. 2013. Quercetin inhibits proliferation and increases sensitivity of ovarian cancer cells to cisplatin and paclitaxel. *Ginekol Pol,* 84**,** 590–5.

MAMAN, S. & WITZ, I. P. 2018. A history of exploring cancer in context. *Nat Rev Cancer,* 18**,** 359–376.

MANICKASAMY, M. K., VISHWA, R., BHARATHWAJCHETTY, B., ALQAHTANI, M. S., ABBAS, M. & KUNNUMAKKARA, A. B. 2025. Cytokine symphony: Deciphering the tumor microenvironment and metastatic axis in oral cancer. *Cytokine Growth Factor Rev,* 85**,** 1–10.

MARCHETTI, C., PISANO, C., FACCHINI, G., BRUNI, G. S., MAGAZZINO, F. P., LOSITO, S. & PIGNATA, S. 2010. First-line treatment of advanced ovarian cancer: current research and perspectives. *Expert Rev Anticancer Ther,* 10**,** 47–60.

MARTíNEZ-REYES, I. & CHANDEL, N. S. 2021. Cancer metabolism: looking forward. *Nat Rev Cancer,* 21**,** 669–680.

MEZZAPESA, F., GIUNCHI, S., DE LEO, A., GIULIA, D., DI COSTANZO, S., GENOVESI, L., DE BIASE, D., DE IACO, P. & PERRONE, A. M. 2025. Mesonephric-like adenocarcinoma of the ovary: features of a rare and aggressive entity associated with endometriosis. *Int J Gynecol Cancer*, 101990.

MIKHAILOVA, E., SOKOLENKO, A., COMBS, S. E. & SHEVTSOV, M. 2025. Modulation of Heat Shock Proteins Levels in Health and Disease: An Integrated Perspective in Diagnostics and Therapy. *Cells,* 14.

MIN, K., LU, C., WU, X., ZHONG, S., MA, P., ZHENG, Y., XUE, K., SUN, Q., LIU, W., WANG, C., YU, L., LI, K., HONG, M. & LI, R. 2025. Identifying an immunogenic cell death-related gene signature and HSPA6 infers adverse prognosis in acute myeloid leukemia. *J Cancer,* 16, 3643–3653.

MINERVA, BHAT, A., VERMA, S., CHANDER, G., JAMWAL, R. S., SHARMA, B., BHAT, A., KATYAL, T., KUMAR, R. & SHAH, R. 2023. Cisplatin-based combination therapy for cancer. *J Cancer Res Ther,* 19, 530–536.

MONNERET, C. 2011. Platinum anticancer drugs. From serendipity to rational design. *Ann Pharm Fr,* 69, 286–95.

MONTERAN, L. & EREZ, N. 2019. The Dark Side of Fibroblasts: Cancer-Associated Fibroblasts as Mediators of Immunosuppression in the Tumor Microenvironment. *Front Immunol,* 10, 1835.

MOUAWAD, N., CAPASSO, G., RUGGERI, E., MARTINELLO, L., SEVERIN, F., VISENTIN, A., FACCO, M., TRENTIN, L. & FREZZATO, F. 2023. Is It Still Possible to Think about HSP70 as a Therapeutic Target in Onco-Hematological Diseases? *Biomolecules,* 13.

MURPHY, M. E. 2013. The HSP70 family and cancer. *Carcinogenesis,* 34, 1181–8.

NACHTIGAL, M. W., ALTMAN, A. D., ARORA, R., SCHWEIZER, F. & ARTHUR, G. 2022. The Potential of Novel Lipid Agents for the Treatment of Chemotherapy-Resistant Human Epithelial Ovarian Cancer. *Cancers (Basel),* 14.

NITZSCHE, B., HöPFNER, M. & BIERSACK, B. 2023. Synthetic Small Molecule Modulators of Hsp70 and Hsp40 Chaperones as Promising Anticancer Agents. *Int J Mol Sci,* 24.

NOESSNER, E., GASTPAR, R., MILANI, V., BRANDL, A., HUTZLER, P. J., KUPPNER, M. C., ROOS, M., KREMMER, E., ASEA, A., CALDERWOOD, S. K. & ISSELS, R. D. 2002. Tumor-derived heat shock protein 70 peptide complexes are cross-presented by human dendritic cells. *J Immunol,* 169, 5424–32.

NOWAK, M., GLOWACKA, E., KIELBIK, M., KULIG, A., SULOWSKA, Z. & KLINK, M. 2017. Secretion of cytokines and heat shock protein (HspA1A) by ovarian cancer cells depending on the tumor type and stage of disease. *Cytokine,* 89, 136–142.

NUNES, M. & RICARDO, S. 2022. Chemoresistance in Ovarian Cancer: The Role of Malignant Ascites. *In:* LELE, S. (ed.) *Ovarian Cancer.* Brisbane (AU): Exon Publications

OLIVEIRA, D., PRAHM, K. P., CHRISTENSEN, I. J., HANSEN, A., HøGDALL, C. K. & HøGDALL, E. V. 2021. Gene expression profile association with poor prognosis in epithelial ovarian cancer patients. *Sci Rep,* 11, 5438.

OSAKI, M., OSHIMURA, M. & ITO, H. 2004. PI3K-Akt pathway: its functions and alterations in human cancer. *Apoptosis,* 9, 667–76.

OZOLS, R. F. 2006. Systemic therapy for ovarian cancer: current status and new treatments. *Semin Oncol,* 33, S3–11.

PARVARESH, A., RAZAVI, R., RAFIE, N., GHIASVAND, R., POURMASOUMI, M. & MIRAGHAJANI, M. 2016. Quercetin and ovarian cancer: An evaluation based on a systematic review. *J Res Med Sci,* 21**,** 34.

PAULI, D., SPIERER, A. & TISSIèRES, A. 1986. Several hundred base pairs upstream of Drosophila hsp23 and 26 genes are required for their heat induction in transformed flies. *Embo j,* 5**,** 755–61.

PAWELEC, G., PICARD, E., BUENO, V., VERSCHOOR, C. P. & OSTRAND-ROSENBERG, S. 2021. MDSCs, ageing and inflammageing. *Cell Immunol,* 362**,** 104297.

PIETRAGALLA, A., ARCIERI, M., MARCHETTI, C., SCAMBIA, G. & FAGOTTI, A. 2020. Ovarian cancer predisposition beyond BRCA1 and BRCA2 genes. *Int J Gynecol Cancer,* 30**,** 1803–1810.

POCALY, M., LAGARDE, V., ETIENNE, G., RIBEIL, J. A., CLAVEROL, S., BONNEU, M., MOREAU-GAUDRY, F., GUYONNET-DUPERAT, V., HERMINE, O., MELO, J. V., DUPOUY, M., TURCQ, B., MAHON, F. X. & PASQUET, J. M. 2007. Overexpression of the heat-shock protein 70 is associated to imatinib resistance in chronic myeloid leukemia. *Leukemia,* 21**,** 93–101.

RAIMONDI, G., TURNER, M. S., THOMSON, A. W. & MOREL, P. A. 2007. Naturally occurring regulatory T cells: recent insights in health and disease. *Crit Rev Immunol,* 27**,** 61–95.

RAKINA, M., KAZAKOVA, A., VILLERT, A., KOLOMIETS, L. & LARIONOVA, I. 2022. Spheroid Formation and Peritoneal Metastasis in Ovarian Cancer: The Role of Stromal and Immune Components. *Int J Mol Sci,* 23.

RASHIDI, Z., KHOSRAVIZADEH, Z., TALEBI, A., KHODAMORADI, K., EBRAHIMI, R. & AMIDI, F. 2021. Overview of biological effects of Quercetin on ovary. *Phytother Res,* 35**,** 33–49.

RAY-COQUARD, I., LEARY, A., PIGNATA, S., CROPET, C., GONZáLEZ-MARTíN, A., MARTH, C., NAGAO, S., VERGOTE, I., COLOMBO, N., MäENPää, J., SELLE, F., SEHOULI, J., LORUSSO, D., GUERRA ALIA, E. M., BOGNER, G., YOSHIDA, H., LEFEUVRE-PLESSE, C., BUDERATH, P., MOSCONI, A. M., LORTHOLARY, A., BURGES, A., MEDIONI, J., EL-BALAT, A., RODRIGUES, M., PARK-SIMON, T. W., DUBOT, C., DENSCHLAG, D., YOU, B., PUJADE-LAURAINE, E. & HARTER, P. 2023. Olaparib plus bevacizumab first-line maintenance in ovarian cancer: final overall survival results from the PAOLA-1/ENGOT-ov25 trial. *Ann Oncol,* 34**,** 681–692.

RICHARDSON, D. L., ESKANDER, R. N. & O'MALLEY, D. M. 2023. Advances in Ovarian Cancer Care and Unmet Treatment Needs for Patients With Platinum Resistance: A Narrative Review. *JAMA Oncol,* 9**,** 851–859.

RICKARD, B. P., CONRAD, C., SORRIN, A. J., RUHI, M. K., READER, J. C., HUANG, S. A., FRANCO, W., SCARCELLI, G., POLACHECK, W. J., ROQUE, D. M., DEL CARMEN, M. G., HUANG, H. C., DEMIRCI, U. & RIZVI, I. 2021. Malignant Ascites in Ovarian Cancer: Cellular, Acellular, and Biophysical Determinants of Molecular Characteristics and Therapy Response. *Cancers (Basel),* 13.

ROMERO, I., LESKELä, S., MIES, B. P., VELASCO, A. P. & PALACIOS, J. 2020. Morphological and molecular heterogeneity of epithelial ovarian cancer: Therapeutic implications. *EJC Suppl,* 15**,** 1–15.

SAJI, H., KUROSE, K., SUGIURA, K., MIYAGI, E., ONOSE, R., KATO, H. & NAKAYAMA, H. 2007. Endometrial aspiration cytology for diagnosis of peritoneal lesions in extrauterine malignancies. *Acta Cytol,* 51**,** 533–40.

SAKAI, K., INOUE, M., MIKAMI, S., NISHIMURA, H., KUWABARA, Y., KOJIMA, A., TODA, M., OGAWA-KOBAYASHI, Y., KIKUCHI, S., HIRATA, Y., MIKAMI-SAITO, Y., KYOYAMA, H., MORIYAMA, G., SHIIBASHI, M., SEIKE, M., GEMMA, A. & UEMATSU, K. 2021. Functional inhibition of heat shock protein 70 by VER-155008 suppresses pleural mesothelioma cell proliferation via an autophagy mechanism. *Thorac Cancer,* 12**,** 491–503.

SANNINO, S., GUERRIERO, C. J., SABNIS, A. J., STOLZ, D. B., WALLACE, C. T., WIPF, P., WATKINS, S. C., BIVONA, T. G. & BRODSKY, J. L. 2018. Compensatory increases of select proteostasis networks after Hsp70 inhibition in cancer cells. *J Cell Sci,* 131.

SHAFABAKHSH, R. & ASEMI, Z. 2019. Quercetin: a natural compound for ovarian cancer treatment. *J Ovarian Res,* 12**,** 55.

SHAN, Y., PANG, M., WANG, L., MAO, Y., YAN, R., ZHOU, C., JI, J., MAO, Y., JIN, Y. & YANG, H. 2024. Increased stiffness of extracellular matrix enhanced chemoresistance in 3D-bioprinted ovarian cancer model. *IJB,* 10.

SHIH IE, M. & KURMAN, R. J. 2004. Ovarian tumorigenesis: a proposed model based on morphological and molecular genetic analysis. *Am J Pathol,* 164**,** 1511–8.

SODA, N., REHM, B. H. A., SONAR, P., NGUYEN, N. T. & SHIDDIKY, M. J. A. 2019. Advanced liquid biopsy technologies for circulating biomarker detection. *J Mater Chem B,* 7**,** 6670–6704.

SONG, B., SHEN, S., FU, S. & FU, J. 2022a. HSPA6 and its role in cancers and other diseases. *Mol Biol Rep,* 49**,** 10565–10577.

SONG, M., CUI, M. & LIU, K. 2022b. Therapeutic strategies to overcome cisplatin resistance in ovarian cancer. *Eur J Med Chem,* 232**,** 114205.

SOTTILE, M. L. & NADIN, S. B. 2018. Heat shock proteins and DNA repair mechanisms: an updated overview. *Cell Stress Chaperones,* 23**,** 303–315.

SUTHERS, G. K. 2007. Cancer risks for Australian women with a BRCA1 or a BRCA2 mutation. *ANZ J Surg,* 77**,** 314–9.

TANIGUCHI, T., TISCHKOWITZ, M., AMEZIANE, N., HODGSON, S. V., MATHEW, C. G., JOENJE, H., MOK, S. C. & D'ANDREA, A. D. 2003. Disruption of the Fanconi anemia-BRCA pathway in cisplatin-sensitive ovarian tumors. *Nat Med,* 9**,** 568–74.

THIGPEN, T., VANCE, R., PUNEKY, L. & KHANSUR, T. 1994. Chemotherapy in advanced ovarian carcinoma: current standards of care based on randomized trials. *Gynecol Oncol,* 55**,** S97–107.

TOMAYKO, M. M. & REYNOLDS, C. P. 1989. Determination of subcutaneous tumor size in athymic (nude) mice. *Cancer Chemother Pharmacol,* 24**,** 148–54.

TORRE, L. A., TRABERT, B., DESANTIS, C. E., MILLER, K. D., SAMIMI, G., RUNOWICZ, C. D., GAUDET, M. M., JEMAL, A. & SIEGEL, R. L. 2018. Ovarian cancer statistics, 2018. *CA Cancer J Clin,* 68**,** 284–296.

TOSS, A., TOMASELLO, C., RAZZABONI, E., CONTU, G., GRANDI, G., CAGNACCI, A., SCHILDER, R. J. & CORTESI, L. 2015. Hereditary ovarian cancer: not only BRCA 1 and 2 genes. *Biomed Res Int,* 2015**,** 341723.

UEDA, G., TAMURA, Y., HIRAI, I., KAMIGUCHI, K., ICHIMIYA, S., TORIGOE, T., HIRATSUKA, H., SUNAKAWA, H. & SATO, N. 2004. Tumor-derived heat shock protein 70-pulsed dendritic cells elicit tumor-specific cytotoxic T lymphocytes (CTLs) and tumor immunity. *Cancer Sci,* 95**,** 248–53.

UNO, K., IYOSHI, S., YOSHIHARA, M., KITAMI, K., MOGI, K., FUJIMOTO, H., SUGIYAMA, M., KOYA,

Y., YAMAKITA, Y., NAWA, A., KANAYAMA, T., TOMITA, H., ENOMOTO, A. & KAJIYAMA, H. 2022. Metastatic Voyage of Ovarian Cancer Cells in Ascites with the Assistance of Various Cellular Components. *Int J Mol Sci,* 23.

VAN NOORT, J. M., BSIBSI, M., NACKEN, P., GERRITSEN, W. H. & AMOR, S. 2012. The link between small heat shock proteins and the immune system. *Int J Biochem Cell Biol,* 44**,** 1670–9.

VAN ZYL, B., TANG, D. & BOWDEN, N. A. 2018. Biomarkers of platinum resistance in ovarian cancer: what can we use to improve treatment. *Endocr Relat Cancer,* 25**,** R303–r318.

VAUPEL, P. & MULTHOFF, G. 2021. Revisiting the Warburg effect: historical dogma versus current understanding. *J Physiol,* 599**,** 1745–1757.

WEBB, P. M. & JORDAN, S. J. 2024. Global epidemiology of epithelial ovarian cancer. *Nat Rev Clin Oncol,* 21**,** 389–400.

WHITESIDE, T. L. 2008. The tumor microenvironment and its role in promoting tumor growth. *Oncogene,* 27**,** 5904–12.

WOŹNIAK, K. & BŁASIAK, J. 2002. Recognition and repair of DNA-cisplatin adducts. *Acta Biochim Pol,* 49**,** 583–96.

WU, F., YANG, J., LIU, J., WANG, Y., MU, J., ZENG, Q., DENG, S. & ZHOU, H. 2021. Signaling pathways in cancer-associated fibroblasts and targeted therapy for cancer. *Signal Transduct Target Ther,* 6**,** 218.

WU, Y., ZHANG, X., WANG, Z., ZHENG, W., CAO, H. & SHEN, W. 2022. Targeting oxidative phosphorylation as an approach for the treatment of ovarian cancer. *Front Oncol,* 12**,** 971479.

XI, Y., ZHANG, Y., ZHENG, K., ZOU, J., GUI, L., ZOU, X., CHEN, L., HAO, J. & ZHANG, Y. 2023. A chemotherapy response prediction model derived from tumor-promoting B and Tregs and proinflammatory macrophages in HGSOC. *Front Oncol,* 13**,** 1171582.

YAN, Y., ZHANG, J., REN, L. & TANG, C. 2016. Metal-containing and related polymers for biomedical applications. *Chem Soc Rev,* 45**,** 5232–63.

YEE, C., DICKSON, K. A., MUNTASIR, M. N., MA, Y. & MARSH, D. J. 2022. Three-Dimensional Modelling of Ovarian Cancer: From Cell Lines to Organoids for Discovery and Personalized Medicine. *Front Bioeng Biotechnol,* 10**,** 836984.

YOUSEFI, M., DEHGHANI, S., NOSRATI, R., GHANEI, M., SALMANINEJAD, A., RAJAIE, S., HASANZADEH, M. & PASDAR, A. 2020. Current insights into the metastasis of epithelial ovarian cancer - hopes and hurdles. *Cell Oncol (Dordr),* 43**,** 515–538.

YUN, C. W., KIM, H. J., LIM, J. H. & LEE, S. H. 2019. Heat Shock Proteins: Agents of Cancer Development and Therapeutic Targets in Anti-Cancer Therapy. *Cells,* 9.

ZHANG, B. & QI, R. 2025. The dual-function of HSP70 in immune response and tumor immunity: from molecular regulation to therapeutic innovations. *Front Immunol,* 16**,** 1587414.

ZHANG, L., ZHUO, H. Q., HONG, Z. J., HOU, J. J., CHENG, J. & CAI, J. 2023. HSPA6, a novel prognostic and therapeutic biomarker, associated with Ming classification in gastric cancer. *J Clin Lab Anal,* 37**,** e24763.

ZHAO, K., ZHOU, G., LIU, Y., ZHANG, J., CHEN, Y., LIU, L. & ZHANG, G. 2023. HSP70 Family in Cancer: Signaling Mechanisms and Therapeutic Advances. *Biomolecules,* 13.

ZHAO, R., LI, H., GE, W., ZHU, X., ZHU, L., WAN, X., WANG, G., PAN, H., LU, J. & HAN, W. 2022. Comprehensive Analysis of Genomic Alterations in Hepatoid Adenocarcinoma of the Stomach and Identification of Clinically Actionable Alterations. *Cancers (Basel),* 14.

ZHOU, X., JI, Q., LI, Q., WANG, P., HU, G., XIAO, F., YE, M., LIN, L., LUO, M., GUO, Y., WU, W., HUANG, K. & GUO, H. 2022. HSPA6 is Correlated With the Malignant Progression and Immune Microenvironment of Gliomas. *Front Cell Dev Biol,* 10**,** 833938.

ZHU, C., XIE, Y., LI, Q., ZHANG, Z., CHEN, J., ZHANG, K., XIA, X., YU, D., CHEN, D., YU, Z. & CHEN, J. 2023. CPSF6-mediated XBP1 3'UTR shortening attenuates cisplatin-induced ER stress and elevates chemo-resistance in lung adenocarcinoma. *Drug Resist Updat,* 68**,** 100933.

ZHU, S., ZHANG, C., CAO, D., BAI, J., YU, S., CHEN, J., WANG, J., REN, T., YANG, J., YU, M., XIAO, X., GONG, Y., GUAN, Y., LI, P., YUE, Y., YIN, R., WANG, Y., AN, R., LOU, G., YUAN, J., ZHANG, G., XIA, X., YANG, L. & XIANG, Y. 2022. Genomic and TCR profiling data reveal the distinct molecular traits in epithelial ovarian cancer histotypes. *Oncogene,* 41**,** 3093–3103.

ZHU, X., ZHANG, K., WANG, Q., CHEN, S., GOU, Y., CUI, Y. & LI, Q. 2015. Cisplatin-mediated c-myc overexpression and cytochrome c (cyt c) release result in the up-regulation of the death receptors DR4 and DR5 and the activation of caspase 3 and caspase 9, likely responsible for the TRAIL-sensitizing effect of cisplatin. *Med Oncol,* 32**,** 133.

ZHUANG, Q., GU, G., CHEN, J., TANG, Z., WU, C., LIU, J. & QU, L. 2025. Global, regional, and national burden of ovarian cancer among young women during 1990-2019. *Eur J Cancer Prev,* 34**,** 1–10.

ZOŃ, A. & BEDNAREK, I. 2023. Cisplatin in Ovarian Cancer Treatment-Known Limitations in Therapy Force New Solutions. *Int J Mol Sci,* 24.

ZSIROS, E., LYNAM, S., ATTWOOD, K. M., WANG, C., CHILAKAPATI, S., GOMEZ, E. C., LIU, S., AKERS, S., LELE, S., FREDERICK, P. J. & ODUNSI, K. 2021. Efficacy and Safety of Pembrolizumab in Combination With Bevacizumab and Oral Metronomic Cyclophosphamide in the Treatment of Recurrent Ovarian Cancer: A Phase 2 Nonrandomized Clinical Trial. *JAMA Oncol,* 7**,** 78–85.

8. List of Abbreviations

Table18 *Abbreviations*

Abbreviation	Full term
2D	Two-dimensional
3D	Three-dimensional
APS	Ammonium persulfate
BCA	Bicinchoninic acid
BLI	Bioluminescence imaging
BSA	Bovine serum albumin
DAB	3,3′-diaminobenzidine
DFS	Disease-Free Survival
DNA	Deoxyribonucleic acid
DMSO	Dimethyl sulfoxide
EOC	Epithelial Ovarian Cancer
FCS	Fetal calf serum
FIGO	International Federation of Gynecology and Obstetrics
HEK	Human embryonic kidney
HGSOC	High-grade serous ovarian cancer
HSC70	Heat shock cognate 70 kDa protein
HSP	Heat shock protein
HSPA1A	Heat shock 70 kDa protein 1A
HSPA1B	Heat shock 70 kDa protein 1B
HSPA6	Heat shock 70 kDa protein 6
IHC	Immunohistochemistry
IRS	Immunoreactive score
i.p.	Intraperitoneal
IVIS	*In vivo* imaging system
KD	Knockdown
LGSOC	Low-grade serous ovarian cancer
mPCI	Modified Peritoneal Cancer Index
mRNA	Messenger RNA
PBS	Phosphate-buffered saline
qPCR	Quantitative real-time PCR
RIPA	Radioimmunoprecipitation assay

RNA	Ribonucleic acid
RNA-seq	RNA sequencing
RT	Room temperature
SD	Standard deviation
SDS–PAGE	Sodium dodecyl sulfate polyacrylamide gel electrophoresis
shRNA	Short hairpin RNA
SPF	Specific pathogen-free
TME	Tumor microenvironment
TTV	Total tumor volume
WST-1	Water-soluble tetrazolium salt-1

9. Figure Contents

10. Table contents

11. Declaration of personal Contribution

This study was conducted at the Department of Gynaecology, University Medical Center Hamburg-Eppendorf under the supervision of Prof. Dr. Leticia Oliveira-Ferrer.

I contributed to the work as follows:

1) Study concept: Discussion of the overall research design, formulation of the central hypothesis, choice of experimental conditions and interpretation of results.

2) Experimental work: Independent performance of the *in vitro* experiments described in this thesis. These included maintenance of cell lines, isolation and culture of ascites-derived spheroids and tumoroids, drug treatment assays, Western blot analyses, quantitative real-time PCR, 2D and 3D cell viability assays and immunohistochemical staining. I also contributed to the design, performance and documentation of the mouse xenograft experiments in collaboration with animal facility staff and cooperating researchers.

3) Data collection and analysis: Collection, organisation and analysis of raw experimental data, including evaluation with appropriate software tools, statistical analysis and preparation of figures and summary tables.

4) Manuscript and thesis writing: Writing of the manuscripts and thesis chapters, including text, figures and tables, and revision of the written work in close collaboration with my supervisor.

I confirm that the above statements accurately reflect my personal contribution to the work presented in this thesis.

12. Eidesstattliche Versicherung

Ich versichere ausdrücklich, dass ich die Arbeit selbständig und ohne fremde Hilfe, insbesondere ohne entgeltliche Hilfe von Vermittlungs- und Beratungsdiensten, verfasst, andere als die von mir angegebenen Quellen und Hilfsmittel nicht benutzt und die aus den benutzten Werken wörtlich oder inhaltlich entnommenen Stellen einzeln nach Ausgabe (Auflage und Jahr des Erscheinens), Band und Seite des benutzten Werkes kenntlich gemacht habe. Das gilt insbesondere auch für alle Informationen aus Internetquellen.

Soweit beim Verfassen der Dissertation KI-basierte Tools („Chatbots“) verwendet wurden, versichere ich ausdrücklich, den daraus generierten Anteil deutlich kenntlich gemacht zu haben. Die „Stellungnahme des Präsidiums der Deutschen Forschungsgemeinschaft (DFG) zum Einfluss generativer Modelle für die Text- und Bilderstellung auf die Wissenschaften und das Förderhandeln der DFG“ aus September 2023 wurde dabei beachtet.

Ferner versichere ich, dass ich die Dissertation bisher nicht einem Fachvertreter an einer anderen Hochschule zur Überprüfung vorgelegt oder mich anderweitig um Zulassung zur Promotion beworben habe.

Ich erkläre mich damit einverstanden, dass meine Dissertation vom Dekanat der Medizinischen Fakultät mit einer gängigen Software zur Erkennung von Plagiaten überprüft werden kann.

Datum Unterschrift

13. Acknowledgements

First and foremost, I would like to express my sincere gratitude to my supervisor, Prof. Dr. Leticia Oliveira-Ferrer, for her dedicated mentorship. As head of laboratory, she has consistently shaped the direction of this project and provided invaluable scientific guidance throughout my doctoral work. Her expertise, rigorous scientific standards and warm, supportive attitude have created an inspiring research environment during my doctoral study.

I am also grateful to Prof. Dr. Linda Diehl for her expertise in molecular biology and for her helpful advice whenever I faced experimental difficulties. My sincere thanks go to Ms Kathrin Eylmann and Ms Maila Rossberg for their essential scientific and technical support throughout this project.

I would further like to thank Tobias Gosau from the Institute of Anatomy and Experimental Morphology for his assistance and guidance with the mouse experiments, Michael Horn from UCCH for his support with the *in vivo* imaging, and Kristoffer Riecken from the Center for Oncology for his help and advice with the transfection experiments.

I am grateful to Prof. Dr. Schmalfeldt and the team of the Department of Gynaecology at the University Medical Center Hamburg-Eppendorf for their sustained support of this project. I especially thank all patients who agreed to participate and donated samples; without their contribution, this work would not have been possible.

I also gratefully acknowledge the financial support of the China Scholarship Council (CSC).

My deepest thanks go to my family and friends for their constant encouragement, understanding and support throughout this journey.